2016

Simulation Studies For Relative Importance Of Unconventional Reservoir Subgrid Scale Physics Parameters

Yaakoub Youssef El Khamra
Louisiana State University and Agricultural and Mechanical College

SIMULATION STUDIES FOR RELATIVE IMPORTANCE OF UNCONVENTIONAL RESERVOIR SUBGRID SCALE PHYSICS PARAMETERS

A Dissertation

Submitted to the Graduate Faculty of the
Louisiana State University and
Agricultural and Mechanical College
in partial fulfillment of the
requirements for the degree of
Doctor of Philosophy

in

Petroleum Engineering

by
Yaakoub El-Khamra
MS, Louisiana State University, 2009
BE, American University of Beirut, 2002
December 2016

To my father.

Acknowledgments

I would like to acknowledge my PhD advisor Professor Mayank Tyagi for keeping me on track and my committee members Professors Blaise Bourdin, Richard Hughes, Mehdi Zeidouni Justin Ragains for their help, support and understanding. I would like to thank Professor Chris White for his mentorship and guidance throughout the years.

I would also like to acknowledge the support from my colleagues at the Texas Advanced Computing Center (TACC), especially Dr. Kent Milfeld, Dr. Lars Koesterke, Dr. Doug James, Chris Hempel, Bob Garza, Dr. John Cazes, Dr. Dan Stanzione, Dr Robert McLay, Dr. Rion Dooley, Jo Wozniak, Dr. Bill Barth, Dr. Tommy Minyard, Dr. Karl Schulz, Dr. Jay Boisseau, David Anderson and Jim Foster. I am indebtted to you all.

This work would not have been possible without the support and understanding of the SRMS Development Team in Houston and in Rijswijk, specifically Dr. Jeroen Vink, Dr. Fredrik Saaf, Dr. Tulio Colmenares, Dr. Paul Good, Dr. Paul Van Hagen, Dr. Steve Shi, Dr. Guohua Gao, Dr. Wenfeng Xie, Dr. Honggang Zhie, Mr. Terence Wells, along with the support of Dr. Sherif Abd El Gawad, Mr. Hani Shaabi, Mr. Abiodun Alimi, Dr. Kefei Wang and Mr. Kerstan Moran.

Last but not least I would like to convey my most sincere gratitude to my friends and colleagues Dr. Richard Duff, Ms Stacy Warrick for their diligent review of my work.

This work is dedicated to my family Dr. Youssef El Khamra, Ms Randa Al-Khatib, Dr. Akaber El Khamra and Dr. Omar El Khamra.

Table of Contents

List of Tables

List of Figures

Abstract

In this endeavor we attempt to better understand gas transport in shale gas reservoirs, specifically the impact and effects of different physical phenomena. We start by documenting the nature of the reservoirs and the need for accurate modeling of various physical phenomena in multiple interconnected continua. The physical phenomena of interest include non-linear Forchheimer flow, Knudsen diffusion in the form of slip "Klinkenberg" flow and adsorption/desorption.

The numerical methods used in the reservoir simulator are also introduced, along with a derivation of the main equations used. Various verification and validation results are compared against manufactured and analytical solutions and finally advanced features including mesh adaptivity and multi-block support are showcased.

Several detailed parameter survey studies are conducted with realistic and exaggerated field values to identify the need for advanced physics models based on deviation from Darcy models. Recommendations as to the applicability of each model are presented along with suggested best practices of when to apply these models in real simulations.

A redefinition of the SRV is proposed, based on the need to apply a non-Darcy flow model. This new definition would highlight the need for advanced (and costly) non-linear flow models near the wells and hydraulic fractures. The judicious application of computationally intensive physical models in the SRV and lower fidelity models further away is presented as an efficient alternative to large scale high fidelity simulations.

Chapter 1
Shale Gas Reservoirs

1.1 Shale Gas Reservoirs

Shale gas is the oldest source of natural gas in the United States. The first commercial gas well in the United States was completed in 1821 from the Devonian Dunkirk Shale in Chatauqua County, New York. Gas from that well was used to light the town of Fredonia a whole thirty five years before Drake's well at Oil Creek, Pennsylvania.

Significant commercial production of shale gas did not begin until 1926 when the Devonian Shales in the Appalachian basin were produced. In the 1980's shale gas development became widespread after a United States government tax incentive program was initiated to stimulate the exploration and development of unconventional reservoirs.

Recent advances in drilling, completion and production technology, coupled with an increase in demand have turned shale gas from gas-in-place to producible reserves. There are several shale gas reservoirs in the continental United States (Figure 1.1). The Barnett Shale is of particular interest as it may have the largest producible reserves of any onshore gas field. The Barnett Shale has 10,564 producing wells (as of Jan 2009) and covers 5000 square miles.

Over the past decade, the United States shale gas production has increased 14–fold and reserves have tripled over the past 4 years (Figure 1.2). Shale gas is also supplying an increasingly larger portion of the total gas production in the United States (Figure 1.3). Natural gas provides a quarter of all energy used in the United States and is projected to maintain a 24% share until 2035. Shale gas is therefore projected to account for 11% of all energy produced in the United States. The increased importance of shale gas resources is not limited to the United States. Interest has spread to Australia, Canada, China and Europe.

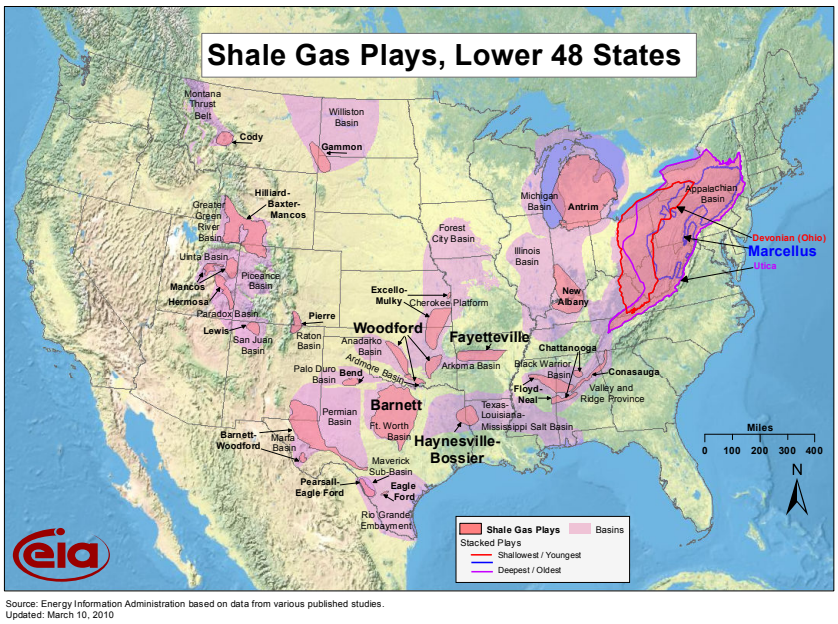

Source: Energy Information Administration based on data from various published studies.
Updated: March 10, 2010

Figure 1.1: Shale gas reservoirs in the lower 48 states. Reproduced From the Energy Information administration, updated March 10 2010

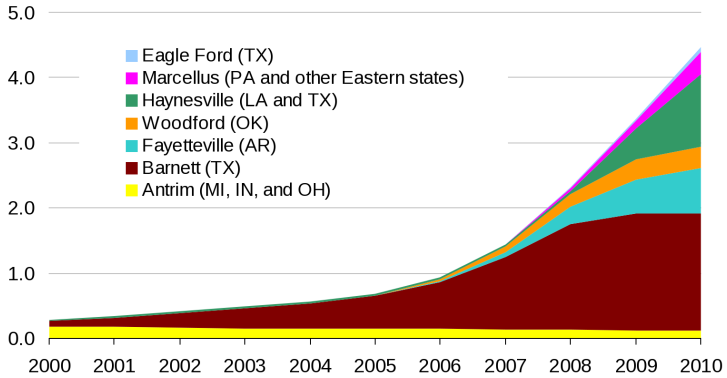

Figure 1.2: Shale gas production in trillions of cubic feet per year from reservoirs in the lower 48 states. Reproduced from the EIA 2010 annual outlook report.

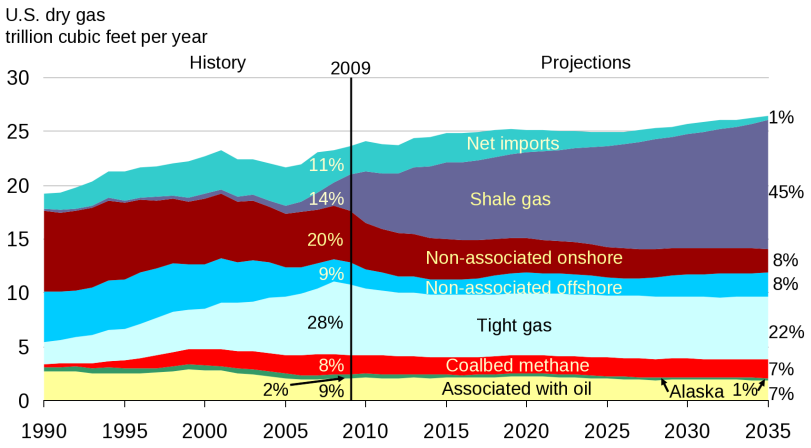

Figure 1.3: Historical and projected gas production in the United States. Shale gas constituted 14% of total gas production in 2009. Shale gas is projected to constitute 45% of the total gas production in 2035. Reproduced from EIA data.

1.2 Origin and Properties of Shale Gas Reservoirs

Shale gas reserves in the United States display different geochemical and reservoir properties. Formations can be biogenic or thermogenic, black shale, black and gray shale or siltstone. Depth varies from 500 ft in the Antrim Shale to 7000 ft in the Barnett Shale. For example, Figure 1.4 and 1.5 shows the different properties of five shale gas reservoirs.

Thermogenic shale gas is formed when organic matter is compressed at high temperatures and pressures for extended periods of time. Organic particles carried in the clastic materials (which turn into shales) undergo a cracking process, similar to oil formation. The temperature, pressure, compression time and nature of organic material determine the ultimate result of the thermogenic process. Thermogenic shale gas can contain significant quantities of heavier hydrocarbons but can also be nearly pure methane. Fayetteville, Barnett, Ohio and Lewis shales are thermogenic shales.

Biogenic shale gas is formed by micro–organisms that chemically break down organic matter. Biogenic gas is mostly methane with little to no heavier hydrocarbons. Biogenic shale gas is typically formed at shallow depths (e.g., Antrim Shale 500–2500 ft). Contrary to thermogenic shale gas, biogenic shale gas is unrelated to the processes that form oil. In fact, landfills employ the same biogenic processes that lead to the formation of biogenic

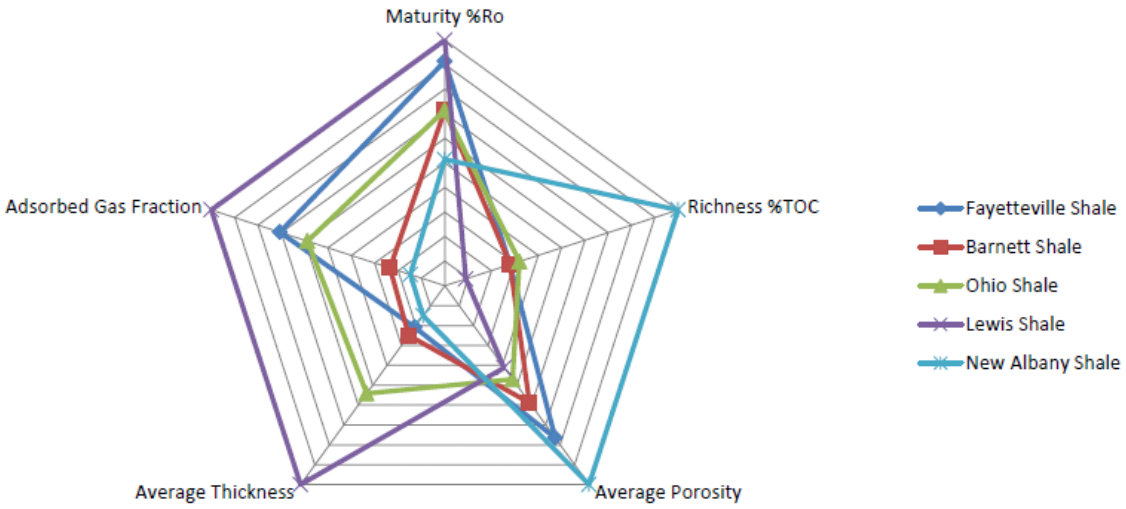

Figure 1.4: Properties of various shale gas reservoirs around the continental United States. Each reservoir is unique in terms of thermal maturity, adsorbed gas fraction, thickness and so on. The reservoir maturity, evaluated by measuring vitrinite reflectance, is a measure of the degree of heating shale has been subjected to. Richness, or percentage total organic carbon is the amount of organic matter in a given sample of rock.

Property	Fayetteville Shale	Barnett Shale	Ohio Shale	Lewis Shale	Antrim Shale	New Albany Shale
Basin	Arkoma	Fort Worth	Appalachian	San Juan	Michigan	Illinois
Age	Mississippian	Mississippian	Devonian	Cretaceous	Devonian	Devonian
Play Type	Black and Gray Shale	Black and Gray Shale	Black Shale and Gray Shale	Siltstone	Black Shale	Black Shale
Sub Play	Thermogenic	Thermogenic	Thermogenic	Thermogenic	Biogenic	Thermogenic and Biogenic
Maturation (Vr %)	1.2 –2.0+	1.1 -1.4	0.6 -1.9	1.6 -1.9	0.6 -0.7	0.6 -1.2
Richness (wt % TOC)	2 -5	2 -5	2 -6	0.5 -1.75	5 -15	5 -20
Porosity (%)	4 -9	3 -7	2 –6	2 -5	5 -12	5 -12
Mineralogy(% Non - Clay)	na	45 -70	45 -60	50 -75	55 -70	50 -70
Thickness (ft)	200-300	200 -400	300 -1,000	500 -1,900	160	180
Depth (ft)	3,000-5,000	7,000 -8,500	2,500 -6,000	4,500 -6,000	500 -2,500	1,000 -2,500
(psi/ft)	0.45 (?)	0.50	≥ 0.3 psi/ft	0.30	0.43	~ 0.43
Avg. Vert. Well EUR (Bcfe)	0.1 –0.5	1.4	0.1-0.5	0.1-0.5	0.75	0.25-0.75
Avg. Hz Well EUR (Bcfe)	1.5	2.5	na	na	na	na
Natural Fractures	Critical to Productivity	Critical to Prod., faults into lower water bad.	Critical to Productivity	Important	Critical to Productivity	Critical to Productivity

Figure 1.5: Properties of various shale gas reservoirs around the continental United States. Most reservoirs are thermogenic and naturally fractured. Higher TOC means more area for gas storage. Similarly, the higher the thermal maturity of the formation, the larger the area for gas storage. Reproduced from EIA.

shale gas to produce methane from biomass for power generation. The Antrim Shale is a biogenic shale, while the New Albany Shale is a mixture of thermogenic and biogenic shale. A standard method to determine nature of a shale gas reservoir is to compare carbon isotope ratios. In thermogenic shale, the C13/C12 ratio is less than that of biogenic shale.

1.3 Production Mechanisms

Shale gas storage can take the form of:

- Sorbed (adsorbed or absorbed) in the organic material: the gas content can be calculated using the TOC
- Free pore space: the gas content depends on porosity and water saturation
- Open Natural Fractures: relatively small amount of gas that can be difficult to quantify

The matrix permeability of shale gas resources in the United States is very low, ranging from 0.2 to 0.00000045 millidarcy. In fact, most shale gas resources depend on natural and hydraulic fractures for higher production. As shown in Figure 1.5, natural fractures are critical to the productivity of Fayetteville, Barnett, Ohio, Antrim and New Albany Shale. These are all black or black and grey shale resources. Lewis Shale is an exception on multiple counts: it is siltstone and is not operated as a stand–alone resource. The Lewis Shale is being completed as a secondary completion zone with new wellbores targeting deeper conventional sandstone reservoirs or as recompletions of existing wells. The gas from the Lewis Shale is commingled with production from deeper zones.

Consider, for example, the Barnett Shale reservoir. The Barnett Shale reservoir has extremely low permeability (100–600 nanodarcys), low porosity (2–6%) and moderate gas adsorption since gas content ranges from 50 to 150 scf/ton (Du et al. 2009). Water saturation was reported to be in the mid 40% range and 75-80% of all natural fractures were healed. To achieve economical production and enhance productivity, a large number of horizontal wells have been drilled and massive multistage hydraulic fracture treatment

jobs have been performed. Due to its complex nature, it was difficult to obtain a clear understanding and accurate description of the Barnett Shale. To quickly acquire knowledge and guide imminent well placement, spacing, pattern and design, various well spacing pilots were drilled and various hydraulic fracturing operation schemes such as "zipper–frac" and "simul–frac" have been developed and tested. It is interesting to note that the salt water used in the hydraulic fracture treatment is produced and recycled (after methane and sand/proppant are separated from the salt water) from the underlying Ellenburger formation. Water is not produced with methane during normal production.

1.4 Well Completions

Since shale gas resources have low permeability, we rely on fractures (natural and hydraulic) for economic production. Today, shale gas production relies on sophisticated horizontal drilling and multi-stage hydraulic fracturing practices. Water mixed with a proppant and an acid treatment additive are injected into the production casing after perforation in a lateral section (typically last 1000 ft). Once the desired fracture pattern is obtained, a fracture plug is installed to isolate the fractured formation. The next section is then perforated, fractured and isolated with another fracture plug. The process repeats until all stages of the hydraulic fracture treatment are complete. The fracture plugs are subsequently drilled out for production.

Computer simulations of the geologic model can be used to evaluate the hydraulic fracturing designs and predict the three-dimensional fracture geometry. Microseismic mapping is used to monitor hydraulic fracturing job responses, help control job processes and evaluate the stimulation results. One key observation made in the case of Barnett Shale was that the fractures were not bi-wing in nature but appeared to have a complex fracture network structure. This is contrary to fracture simulations and other shale gas resources, for example the Marcellus Shale where fractures are bi-wing.

Chapter 2
The Physics of Stimulated Reservoir Volume

2.1 The SRV Region

Unconventional tight-gas or shale-gas reservoirs require stimulation via hydraulic fracturing to create fracture networks for practical exploitation. Within a stimulated reservoir volume (SRV), gas flows from the nano-Darcy scale to the complex fracture network and then to the well for production. The reservoir dynamics are characterized by highly non-linear behavior of many processes, such as gas desorption, Klinkenberg effect, non-Darcy flow and rock deformation in extremely low permeability reservoirs. Therefore it comes as little surprise that a large number of studies have been conducted for unconventional reservoir resources over the past decade: Wang et al. (2009a), King (2010), Wang et al. (2009b), Andrade Perdomo et al. (2010), Leahy-Dios et al. (2011), Andrade Perdomo et al. (2011) and Darishchev et al. (2013).

Blasingame et al. (2008) and Moridis et al. (2010) provide a very comprehensive review of flow mechanisms in unconventional shale gas reservoirs. Many authors use commercial reservoir simulators to study gas production from a shale gas reservoir: Cipolla et al. (2010) Rubin (2010), and Mirzaei et al. (2012). The most popular approach has been to include two or three of the following physical phenomena in a single or multiple interconnected continua (MINC) model (Pruess and Narasimhan 1985; Ding et al. 2014; Java and Univer 2012; Moghanloo and Hosseinipoor 2014; Moinfar et al. 2011; Shabro et al. 2012).

The MINC model developed in this work includes three distinct volumes: a fracture network volume near the well, a stimulated low-permeability matrix volume surrounding the fractures, and an outer unstimulated reservoir volume. The different volumes may exhibit different flow behaviors, therefore different flow models can be applied including Forchheimer flow, Klinkenberg gas-slip flow and gas adsorption/desorption.

The computational approach is to leverage the scalability of the reservoir simulator to take into account all of these physical effects as necessary. With the added advantage of adaptive mesh refinement (and coarsening) we can efficiently and accurately model discrete fractures networks and the non-Darcy flow therein.

2.2 Gas Diffusion And Apparent Permeability

Gas transport mechanisms and apparent permeability in shale reservoirs are significantly different from those in conventional gas reservoirs: gas transport is governed by nanoscale phenomena since the reservoir rock is the source rock.

Accurate determination of the gas permeability in nanopores is required for numerical simulation and is important for gas production forecasting, well placement, and configuration optimization in shale gas reservoirs (Xiong et al. 2012; Tinni et al. 2012; Civan et al. 2013). Nanoscale scanning electron microscope images of shale cores show that organic materials occupy a large volume of the matrix materials. Furthermore, a major portion of the total porosity is contained in pores of the organic matter (Ambrose et al. 2010; Passey et al. 2010). Organic pores are smaller in diameter and adsorb a significant amount of gas on their surfaces (Xiong et al. 2012).

Since organic pore size is nanoscale, which is comparable to the mean free path distance of gas molecules, Knudsen diffusion permeability correction needs to be applied. Wang and Li (2003), Roy et al. (2003) and Holt et al. (2006) reported that Knudsen diffusion is the dominant gas transport mechanism through laboratory experiments. Darabi et al. (2012) also presented the contribution of Knudsen diffusion to cumulative production: for typical shale gas reservoir conditions it can get up to 20%.

2.2.1 Gas Transport Models in Shale Nanopores

Transport mechanisms of bulk gas in shale nanopores include continuum fluid flow, slip flow and transition flow (Rahmanian et al. 2012; Aguilera et al. 2010; Civan et al. 2011; Civan et al. 2012; Civan et al. 2013; Yuan et al. 2014). According to Gad-el Hak (1999), gas transport mechanisms can be divided into two possible categories based on the

inclusion or exclusion of the molecular nature of the gas in transport: molecule models and macro models.

Description of the gas transport mechanism through molecule models, known as molecule modeling, can accurately simulate the various physical mechanisms in nanopores (Gad-el Hak 1999; Malek and Coppens 2002). However, molecule modeling techniques used in shale gas simulations require enormous computing resources and computing time, limiting their application in practice (Koplik and Banavar 1995; Gad-el Hak 1999; Mao and Sinnott 2001; Nie et al. 2004; Coppens and Dammers 2006).

Conventional hydrodynamic continuity models cannot properly describe gas transport mechanisms in organic nanopores (Darabi et al. 2012). There are two possible types of macro models for gas transport mechanisms in shale nanopores:

- hydrodynamic models that modify the no-slip boundary condition in continuum models by accounting for a slip boundary condition (Klinkenberg et al. 1941; Beskok and Karniadakis 1999; Xiong et al. 2012; Civan et al. 2012)

- Hybrid models that combine various transport mechanisms using weighting factors as shown in Table 2.1 (Ertekin et al. 1986; Liu et al. 2002; Jafarpour and McLaughlin 2009; Darabi et al. 2012; Rahmanian et al. 2012).

Klinkenberg et al. (1941) proposed the first empirical model to consider the slip effect. Based on the empirical Klinkenberg model, Luffel et al. (1993) and Wu et al. (1998) described gas transport with slippage effect under low pressure. Beskok and Karniadakis (1999) proposed a model to describe all known gas transport mechanisms in nanopores, including viscous flow, slip flow, transition flow, and free molecule flow conditions.

Civan et al. (2013) modeled gas transport in shale nanopores taking into account the rarefaction effects and slippage effect based on Beskok and Karniadakis' model. Xiong et al. (2012) presented a gas permeability model that considers surface diffusion of adsorbed gas based on Beskok-Karniadaki model.

Table 2.1: Comparison of various permeability models adapted from Wu et al 2014

	Model	Description	Limitation
First Class	Klinkenberg	Empirical model considers only the slippage effect	Does not consider Knudsen diffuion
	Beskok-Karniadakis	Multiple empirical coefficients, consider viscous flow, slip flow, transition flow and free molecule flow conditions	Does not consider Knudsen diffuion
	Civan	Similar to Beskok-Karniadakis	
	Xiong	Simiar to Beskok-Karniadakis but considers adsorbed gas surface diffusion	
Second Class	Ertekin	Based on viscous flow and diffusion flow, summation of two mechanisms using constant weight coefficients	All these models have empirical coefficients which need to be obtained through experiments.
	Liu	Based on viscous flow and Knudsen diffusion, summation of two mechanisms based on the ratio of flow cross-sectional area as the contribution weights not suitable when Knudsen number Kn>=1	
	Javadpour	Empirical coefficients, the linear summation of slip flow and Knudsen diffusion	
	Azom and Javadpour	Same as Javadpour but considers real gas	
	Darabi	Same as Javadpour but considers the effect of wall roughness on Knudsen diffusion	
	Sing and Javadpour	Linear summation between convective flow and Fick diffusion	
	Rahmanian	Summation of viscous flow and Knudsen diffusion using weight coefficients containing empirical coefficients	

Macro model development started with Ertekin who proposed an analytical model with a constant contribution coefficient for viscous flow and diffusion flow (Ertekin et al. 1986). It did not however cover the entire flow-regime spectrum. Liu et al. (2002) applied Adzumi's contribution coefficient as a weight to balance viscous flow, Knudsen diffusion, and modeled gas slippage in nanopores where, the weight coefficient of Knudsen diffusion is the ratio of the slip layer area to nanopore cross-sectional area. However, when the Knudsen number K_n is larger than or equal to 1, the Knudsen diffusion weight coefficient becomes zero and the model goes unphysical.

Javadpour et al. (2009) made a linear superposition of the Knudsen diffusion and slip flow based on the Maxwell theory. AzomPN (2012) proposed gas transmission model for real gas in nanopores based on Javadpour's model. Darabi et al. (2012) considered the effect of wall roughness on Knudsen diffusion in nanopores also based on Javadpour's model. Singh et al. (2013) proposed the nonempirical apparent permeability model based on the analytical model of Veltzke and Thming (Veltzke and Thöming 2012).

Rahmanian et al. (2012) proposed an empirical formula describing the contribution of viscous flow and Knudsen diffusion using Aguilera's formula (Aguilera 2006). The empirical formula contains unknown weighting coefficients which are obtained through experiments, resulting in the limited application.

The key issue in these models is how to properly determine the weight coefficients. To date, there are very few reliable empirical data points available for shale due to high complexity of shale system resulting from different organic materials and mineral types as well as different gas components (Singh et al. 2013).

2.3 Adsorption-Desorption Models

There is a significant amount of adsorbed gas in shale reservoirs. Lu et al. (1995) studied 24 samples of Devonian Shale and showed that the adsorbed gas can contribute up to 61% of total gas volume on average. Desorption of the adsorbed gas plays an important part in transport of gas (Javadpour et al. 2009; Cui and Kelkar 2005). As adsorbed gas

desorbs, it increases the hydraulic diameter of pores, reducing tortuosity and causing extra slippage at the boundary, thereby increasing the matrix permeability many folds (Swami et al. 2013).

Cui et al. (2009) revised the analytical model of Jones et al. (1997) to consider the adsorption/desorption. Adsorbed gas also provides a significant contribution to the final recovery. Yu (2002) simulated thirty years of shale gas development in north America and their results show differences between the gas adsorption capacity and contribution to the ultimate recovery in different reservoirs. New Albany and Marcellus Shale were more than 20%. Haynesville Shale was less than 10%, and Barnett Shale and Eagleford were in the 10% to 20% range.

The adsorption/desorption equation is:

$$\frac{dC}{dt} = \begin{cases} -(C - C_e)/\tau_d & \text{for } C >= C_e \\ -(C - C_e)/\tau_a & \text{for } C < C_e \end{cases} \tag{2.1}$$

Where $C = C(x,t)$ is the adsorbed concentration of a fluid (mass/volume, $kg.m^{-3}$ in SI), τ_d is the time constant for desorption, τ_a the time constant for adsorption and C_e the equilibrium concentration. Note the lack of spatial derivatives as this is a Newton-cooling equation.

Since this is flow through porous media, the adsorption/desorption term appears in the time derivative as fluid is desorbed from the matrix into the pore space (and adsorbed from the pore space back into the matrix). The density time derivative would be:

$$\frac{d\rho}{dt} = \frac{1}{\tau}(C - C_e) \tag{2.2}$$

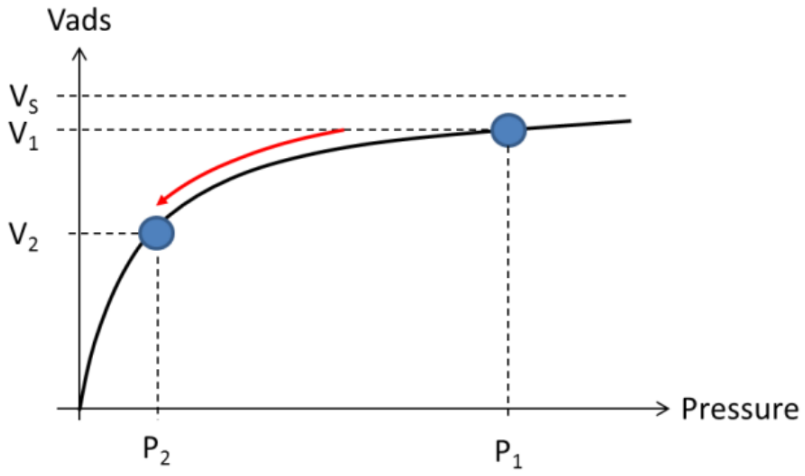

Figure 2.1: The volume of desorbed gas depends on the shape of the isotherm. In general the higher the pressure drop at lower pressure the greater the volume of desorbed gas

The $\frac{C-C_e}{\tau}$ term is the rate of desorption (with $\tau = \tau_d$) or adsorption (with $\tau = \tau_a$) from the matrix to the pore space.

C_e the equilibrium concentration can take many forms but the most common is Langmuir isothermal model defined as:

$$C_e = \frac{\rho_L P}{P + P_L} \tag{2.3}$$

where ρ_L is the Langmuir density and P_L is the Langmuir pressure.

The volume of desorbed gas depends on the shape of the Langmuir isotherm and the general trend for typical shale formations seems to be higher desorbed gas volumes with large pressured drops at low pressure (Figure 2.1).

Chapter 3
Computational Models

3.1 Dual Continuum Models

It is important to note that the dual-continuum concept is a subset of the more general Multiple-Interacting-Continua (MINC) formulation (Pruess and Narasimhan 1985; Moridis et al. 2010). Dual-continuum models are subdivided into dual-permeability and dual-porosity depending on whether matrix-matrix flow is allowed or not respectively. It might seem logical to use the dual-porosity model for shale and tight gas reservoirs because of their very low matrix permeabilities, but the effect of slip-flow and Knudsen diffusion can produce apparent matrix permeabilities that are three orders of magnitude greater than the Darcy matrix permeability (Javadpour et al. 2007; Javadpour et al. 2009; Ozkan et al. 2010). Since gas mobilities are generally high, we immediately see why the dual porosity model might be inadequate. Also, both models have been shown to give quite different results for shale and tight gas reservoirs for a reduced MINC formulation (Moridis et al. 2010).

The most critical aspect of a dual-continuum model is the handling of matrix-fracture interaction and there are three major trends in literature.

The first class of methods is referred to as the boundary condition approach which involves obtaining the matrix-fracture transfer terms explicitly by imposing appropriate boundary conditions between a fracture and its matrix block at each time step of the simulation. This method has been successfully applied to near wellbore studies such as well testing (Kazemi et al. 1976; Ozkan et al. 2010), but is impractical in full field simulations. Zimmerman et al. (1993) also reported numerical instabilities for large time steps when this method was used in a numerical simulator.

The second class of methods is the Warren-Root method. These are very popular with commercial reservoir simulators. These methods assume pseudo-steady state flow between

the matrix block and surrounding fractures with a matrix-fracture transfer term, T_{m-f}. The transfer fracture transfer term T_{m-f} typically includes a pseudo-steady state shape factor and takes the following form:

$$T_{m-f} = \frac{\sigma k_m}{\mu}(P_m - P_f) \tag{3.1}$$

where σ is the pseudo-steady state shape factor that characterizes the surface-volume ratio available for matrix-fracture flows. Its value is a constant for single phase flows and depends on the number of orthogonal fracture sets surrounding the matrix block (Kazemi et al. 1976; Warren and Root 1963). There has been several variants of these Warren-Root type models and they are all derived by considering pseudo-steady state.

A more accurate model would require using more terms in the transient series solution but this would give a form that can not be easily used in numerical simulators (Zimmerman et al. 1993; Lim and Aziz 1995). The third method attempts to overcome this challenge by using an algebraic approximation to the transient series solution which can be used to derive matrix-fracture transfer terms that can easily be implemented in numerical simulators. An example of such a formulation is the Vermeulen model in which, following Zimmerman et al. (1993), can be shown to give a shape factor corresponding to

$$\sigma_{Transient} = \sigma \frac{(P_i - P_f)^2 - (P_i - P_m)^2}{2(P_i - P_m)(P_m - P_f)} \tag{3.2}$$

where P_i is the initial reservoir pressure. Equation 3.2 shows that the transient shape factor is not a constant but a function of the different pressure regimes experienced by the matrix block. Equation 3.2 also approaches the Warren-Root type models as $P_m \Rightarrow P_f$.

For our purposes we use a steady state transfer function with a general shape factor based on the work of Wuthicharn and Zimmerman (2011) and subsequently Shahvali

(2014), Amiry et al. (2014), and Wang (2015). Withicharn and Zimmerman developed a general numerical procedure to calculate shape factors for arbitrary shapes using fine-grid simulation of flow into a single matrix block with constant-pressure boundary conditions. Withicharn's scaling law expresses the shape factor in terms of the block's volume V and the block's outer surface area S. The expression is as follows in two and three dimensions respectively:

$$\sigma_{2D} = \frac{5 \cdot Perimeter}{Area^{1.5}} \tag{3.3}$$

$$\sigma_{3D} = \frac{5 \cdot SurfaceArea}{Volume^{4/3}} \tag{3.4}$$

It is worth mentioning that arbitrary shape factor support is critical for finite elements, especially with adaptive mesh refinement as the shape of resulting elements cannot be predicted a priori.

3.2 Discrete Fracture Models

Flow through naturally fractured media is typically modeled with dual permeability, dual porosity. This approach however suffers from major limitations: the fractures must be small scale, connected, uniformly distributed and the transfer function between matrix and fracture is usually assumed to be a steady-state function when in reality it is transient.

For discrete fractures (large scale, non-uniform fractures) discrete fracture modeling offers some advantages over dual permeability, dual porosity models depending on the type of discrete fracture model used. There are three main categories of discrete fracture models in literature: embedded fracture (source-term) based models, fracture discretization models and multi-scale models.

3.2.1 Embedded Fracture Modeling

To capture the complex geometry of fractured porous media it is necessary to use an unstructured discretization. Embedded fracture modeling techniques remove this restriction and, in general, are the least computationally expensive of all discrete fracture models.

Embedded discrete fracture modeling (EDFM) borrows the concept of dual medium and incorporates the effects of individual fractures. This makes EDFM compatible with finite difference, finite volume and finite element reservoir simulators. There is however the need for moderate mesh refinement around the cells containing fractures. EDFM methods do not require the computational mesh to conform to the complex geometry of the fracture.

The basic premise of EDFM (Li and Lee 2008) is to model fractures as two-dimensional planes, penetrating multiple cells (possibly containing well models). The intersection of cells and fractures is then computed to obtain the list of cells penetrated by each fracture and the number of intersection points between a cell and the fracture. This is the list of (non)neighboring connections (NNCs). These NNCs add source/sink terms to the mass-balance equations:

$$V_b \frac{\partial}{\partial t}(\phi N_i) - V_b \nabla \cdot \sum_{j=1}^{n_p} \frac{k_{rj}}{\mu_j}(\nabla P_j - \gamma_j \nabla z) - q_i + q_i^{NNC} = 0 \tag{3.5}$$

where q_i^{NNC} is the rate of component/phase i exchanged through the NNCs. This term is approximated as a convection term and is given by:

$$q_i^{NNC} = \sum_{m=1}^{n_{NNC}} A_m^{NNC} \sum_{j=1}^{n_p} \frac{k_m^{NNC} k_{rj}}{\mu_j} \left[\frac{(P_j - \gamma_j z) - (P_j - \gamma_j z)_m^{NNC}}{d_m^{NNC}} \right] \tag{3.6}$$

where n_{NNC} is the number of NNCs for a given gridblock and $(P_j - \gamma_j z)$ represents the potential at the non-neighboring cell. The parameters: A^{NNC}, k^{NNC} and d^{NNC} are the area open to flow, permeability (harmonic average of permeability) and characteristic distance respectively used to determine the transmissibility factor between a NNC pair.

For a NNC between matrix and fracture cells, A^{NNC} is the fracture surface area in the cell, k^{NNC} is the harmonic average of the matrix and fracture permeabilities (typically closer to the matrix permeability). The characteristic distance is calculated by making the assumption that pressure varies linearly in the direction normal to each fracture in a gridblock is given as follows:

$$d^{NNC} = \frac{\int_V x_n dv}{V} \tag{3.7}$$

where dv, x_n and V are the volume element, the normal distance of the element from the fracture, and the volume of a gridblock respectively.

For a NNC between intersecting fracture cells, theKarimi-Fard et al. (2003) approach is typically used, where transmissibility is calculated as follows:

$$\frac{k^{NNC}A}{d^{NNC}} = \frac{T_1 T_2}{T_1 + T_2} \tag{3.8}$$

$$T_1 = \frac{k_{f1} w_{f1} L_{int}}{d_{f1}}, \quad T_2 = \frac{k_{f2} w_{f2} L_{int}}{d_{f2}} \tag{3.9}$$

where L_{int} is the length of the intersection line bounded in a grid block, w_f and k_f are the fracture aperture and fracture permeability respectively. d_f is the average of normal distances from the center of the fracture sub-segments (on each side of the intersection line) to the intersecting fractures. Therefore if more than two fractures intersect in a gridblock, a NNC is defined between each pair of intersecting fracture control volumes. Also if two fractures penetrating a gridblock do not intersect with each other in the block, no NNC is needed.

The last (and simplest) case of NNCs arises between two cells of an individual fracture, k^{NNC} is equal to the fracture permeability and d^{NNC} is the distance between the centers of two fracture segments.

The EDFM method offers a lot of advantages: it is computationally efficient, it does not require the mesh to conform to the geologic fracture, making it easier to conform to the stratigraphic geologic model. The flow equation is still the Darcy equation, therefore it assumes a high permeability flow in the fracture as opposed to stokes flow. It is also

more appropriate for use with naturally fractured reservoirs than hydraulically fractured reservoirs due to the linear pressure assumption. Improvements on EDFM include the use of statistical representations of matrix-fracture transfer functions (Lu and Connell 2010), there are however no improvements as of yet that take into account non-linear flow (i.e. Forchheimer flow).

3.2.2 Fracture Discretization Models

These are methods where the geometric discretization conforms to the fracture geometry. Understandably these methods require the use of unstructured meshes for complex fracture geometries. We distinguish two approaches depending on the presence or absence of a matrix-fracture transfer function.

- **Transfer Function Based Models**

This is the original approach of Karimi-Fard et al. (2003) which uses two/three dimensional control volumes defined over a Delaunay triangulation for the matrix and one/two dimensional segments/convex polygons to describe discrete fractures. The discrete fracture segments/faces are not embedded in nor do they intersect the matrix control volumes.

While use of control volumes enables the use of two-point flux approximations to ensure local mass/energy conservation, local refinement is necessary in some cases to ensure control volume circumcenters are always within the convex hull defined over a control volume.

The basic mathematical model for matrix-matrix flow is as follows: consider the flow between two adjacent control volumes. For any control volume shape and problem dimension, the flow rate can be expressed as:

$$Q_{12} = T_{12}(P_2 - P_1) \tag{3.10}$$

where P is the pressure, Q is the flow rate from cell 1 to cell 2 and T_{12} is the transmissibility, defined as:

$$T_{12} = \frac{\alpha_1 \alpha_2}{\alpha_1 + \alpha_2} \quad \text{with} \quad \alpha_i = \frac{A_i k_i}{d_i} \mathbf{n_i} \cdot \mathbf{f_i} \tag{3.11}$$

A_i being the are of the interface, k_i being the permeability of the control volume i, D_i the distance between the centroid of the interface and the centroid of control volume i, $\mathbf{n_i}$ the unit normal to the interface inside the control volume and $\mathbf{f_i}$ is the unit vector along the direction of the line joining the control volume centroid to the centroid of the interface.

For fracture-fracture flow in the computational domain each portion of the fracture is modeled separately as an intermediate control volume. To "connect" two fracture segments/faces, the harmonic average of their transmissibilities is evaluated, similar to that of connected control volumes in a series. This avoids the need to introduce an explicit geometric definition of a control volume at fracture segment/face connections. If however, more than two fractures segments/faces intersect, flow is linearized and a network of resistors model is used. This approximation ignores gravity and assumes linear near-incompressible or incompressible flow.

Matrix-fracture connections can easily be calculated using 3.11 using only one area (the interface area) and the fracture aperture. It is important to note that while a fracture aperture is used, the geometric discretization does not account for fracture thickness. The fracture volume is typically small compared to the overall matrix if the number of fractures is small. A large number of fractures invalidate this simplification and a reduction in the pore volume of the matrix control volumes connected to the fracture is sufficient to account for its volume.

The benefits of discrete fracture modeling with discrete fractures in the discretization are obvious: the complex geometry of natural fractures can be captured accurately. However, this accuracy comes at a price: the mesh has to conform to the fracture, mesh refinement is necessary to obtain good aspect ratio control volumes. This refined mesh volume is also where the computationally expensive non-linear flow models would need to be applied. A scalable, parallel reservoir simulator is therefore necessary for discrete fracture modeling.

The last approach, the cell-average approach (no transfer function) approach, is the approach of Hoteit and later Geiger-Boschung (Hoteit and Firoozabadi 2006; Geiger-Boschung et al. 2009). In this method, the state unknowns (pressure, saturations/compositions) in the fracture and in the adjacent matrix cells are identical. This removes the need to compute the matrix-fracture flux and the matrix-fracture transfer functions. Only the matrix-matrix and fracture/fracture fluxes are required since the control volume includes the fracture segment/face. Therefore a finer grid size is used in fracture cells.

The formulation presented by Hoteit and Firoozabadi (2006) uses first order Raviart-Thomas finite elements for flux terms and discontinuous Galerkin elements for pressure. This formulation overcomes the unstable nature of this discrete saddle-point problem. The use of first order Raviart-Thomas finite elements is necessary for the formulation, and higher order elements cannot be used in this model.

Consider a triangle k with edges/faces ∂k such that $k \subset K$ where K is a triangulation over Ω. With the first order Raviart-Thomas basis function $w_{K,E}$, the fluxes across the element boundaries are:

$$\mathbf{V} = \sum_{E \in \partial k} q_{k,E} \mathbf{w}_{k,E} \quad \text{and} \quad \mathbf{g} = \sum_{E \in \partial k} q^g_{k,E} \mathbf{w}_{k,E} \tag{3.12}$$

where

$$q_{k,E} = \int_E \mathbf{V} \cdot \mathbf{n}_{k,E} \quad \text{and} \quad q^g_{k,E} = \int_E \mathbf{g} \cdot \mathbf{n}_{k,E} \tag{3.13}$$

Manipulating Darcy's law $\mathbf{u} = -K\left(\nabla p - \rho \mathbf{g}\right)$ by inverting the mobility tensor the equation becomes: $K^{-1}\mathbf{u} = -\left(\nabla p - \rho \mathbf{g}\right)$ and substituting the Raviart Thomas approximation from 3.12 and integrating by parts we obtain:

$$\int_k w_{k,E} K^{-1} \mathbf{J} = -\int_k \mathbf{w}_{k,E} K^{-1} \left(\nabla p - \rho \mathbf{g}\right) \tag{3.14}$$

$$= \int_k p \nabla \cdot w_{k,E} - \int_{\partial k} p \mathbf{w}_{k,E} K^{-1} \cdot n_{k,E} \tag{3.15}$$

$$+ \int_k \rho \mathbf{w}_{k,E} g \quad \text{where} \quad E \in \partial k \tag{3.16}$$

Since Raviart Thomas functions satisfy:

$$\nabla \cdot \mathbf{w}_E = \frac{1}{|K|} \tag{3.17}$$

$$\mathbf{w}_E \cdot \mathbf{n}_{E\prime} = 1/|E| \quad if \quad E = E\prime \quad \text{and 0 otherwise} \tag{3.18}$$

The equation becomes:

$$\int_k \mathbf{w}_{k,E} K^{-1} \mathbf{V} = \frac{1}{|K|} \int_k p - \frac{1}{|E|} \int_k p + \int_k \rho \mathbf{w}_{k,E} g \quad E \in \partial k \tag{3.19}$$

since we average pressures in this approach, let p_k and $tp_{k,E}$ denote the cell average pressure on k and the edge average pressure on E respectively. Replacing terms back into equation 3.19 we arrive at the integration equation over a single cell:

$$\sum_{E\prime \in k} q_{k,E\prime} \int_k \mathbf{w}_{k,E} K^{-1} \mathbf{w}_{k,E\prime} = p_k - tp_{k,E\prime}$$
$$+ \sum_{E\prime \in k} \rho_k q^g_{k,E\prime} \int_k \mathbf{w}_{k,E} \mathbf{w}_{k,E\prime} \quad E \in \partial k$$

This equation can be written in matrix form: $B_K Q_K = p_{KE} - tp_K - \rho_K \tilde{B}_K Q^g_K$. The flux $q_{K,E}$ through each edge E is expressed as a function of the cell pressure average p_K and the edge pressure averages $tp_{K,E}$. Similarly we can express the flux at the one dimensional

fracture ends. The system is assembled over all cells and quadrature rules are used to perform the integration.

It is important to mention that there have been alternative approaches to the use of linear Raviart Thomas elements to circumvent explicit calculations of pressures/fluxes in fracture elements. For example (Martin et al. 2005; Jaffré et al. 2011) explicitly add the flux terms in the fractures to the system unknowns. This approach assumes a hyperplane γ where Darcy's law applies equally to flow in fractures and matrices i.e. $\nabla \cdot \mathbf{u}_i = q_i$ and $\mathbf{u}_i = -K_i \nabla p_i$ for $i = matrix, fracture$. This approach suffers from many limitations in Hoteit's implementation: only simple fractures can be modeled, no intersecting fractures, the flow must be incompressible and a large variation between fracture and matrix permeability lead to an ill-conditioned system. It is important to note that using a fine-grain mesh at the fractures will circumvent all of the limitations of this approach, at the cost of significantly increased computational complexity.

3.2.3 Multiscale Approach: Darcy-Stokes-Brinkman Equations

Multiscale approaches to discrete fracture modeling combine a best-of-both-worlds approach to discrete fracture modeling. First discussed by Popov et al. (2009, Popov et al. (2009) and by Efendiev and Hou (2009), Gulbransen et al. (2009) and Gulbransen et al. (2010). This method can be used to discretely model networks of fractures, vugs and caves, making it ideal for fractured carbonate karst reservoirs.

Typically, the flow in fractured, vuggy media is modeled with coupled Stokes-Darcy equations. The porous regions are modeled with Darcy flow while the Stokes equation is used in the free flow region. At the interface between the two, various types of interface conditions are applied. These differ mainly in the treatment of the tangential components of the velocity at the interface, typically referred to as a "jump" condition. The jump condition selection can be based on flow type, interface type and flow regime (Laptev 2003). Furthermore these jump conditions introduce additional parameters that can be determined experimentally or computationally.

Let the superscript ϵ denote the fine scale, let Ω^f and Ω^p and Γ denote the free flow, porous and interface regions. Also the fluid velocity in the fine scale is denoted by $\mathbf{v}^\epsilon$ and the fine scale pressure by p^ϵ. In the free flow region, $\mathbf{v}^\epsilon$ is the actual physical velocity of the fluid and in the porous region it represents the Darcy velocity.

The stokes equations, applicable in the free flow region, has the form:

$$\nabla p^\epsilon - \mu \Delta \mathbf{v}^\epsilon = \mathbf{f} \text{ in } \Omega^f \tag{3.20}$$

$$\nabla \cdot \mathbf{v}^\epsilon = 0 \text{ in } \Omega^f \tag{3.21}$$

Where the first equation is the linear momentum conservation and the second is the conservation of mass. The fluid stress tensor σ is given by:

$$\sigma = -\rho \mathbf{I} + 2\mu \mathbf{D} \tag{3.22}$$

where $\mathbf{D}$ is the strain rate defined by:

$$\mathbf{D} = \frac{1}{2}\left(\nabla \mathbf{v} + \nabla \mathbf{v}^T\right) \tag{3.23}$$

In the porous region, Darcy's law applies:

$$\mathbf{v}^\epsilon = -\frac{\mathbf{K}}{\mu}\left(\nabla p^\epsilon - \mathbf{f}\right) \text{ in } \Omega^p \tag{3.24}$$

$$\nabla \cdot \mathbf{v}^\epsilon = 0 \text{ in } \Omega^p \tag{3.25}$$

These two systems are coupled at the interface Γ. As we mentioned earlier, there are multiple approaches, the classical condition (Beavers and Joseph 1967) for example is as follows:

$$[\mathbf{v}] \cdot \mathbf{n} = 0 \tag{3.26}$$

$$2\mu \mathbf{D} \cdot \mathbf{n} = [p] \tag{3.27}$$

$$\frac{\partial \mathbf{v}_f}{\partial \mathbf{n}} = \frac{\alpha_{BJ}}{\sqrt{K}} [\mathbf{v}] \cdot \mathbf{t}_i \text{ on } \Gamma \tag{3.28}$$

Where $[\cdot]$ denotes the jump in a certain quantity over the interface, i.e. $[\phi] = \phi_f - \phi_p$ for some field ϕ and $\mathbf{n}$ is the unit normal pointing from Ω^f to Ω^p. The dimensionless parameter α_{BJ} is a material property representing the microstructure of the interface which can be computed experimentally or computationally.

Alternatively, the Stokes-Brinkman equations offer a unified approach in the sense that a single equation with variable coefficients is used for both porous and free-flow equations. Stokes-Brinkman equations can be reduced to Stokes or Darcy equations by appropriate choice of parameters. This circumvents the need to formulate special interface terms and allows the formulation of a continuously varied model from a Darcy dominated flow to a Stokes dominated flow which can be used to effectively simulate partially filled fractures.

As the name implies, we use two scales: a fine and a coarse scale. The fine scale media is composed of a porous media and a free flow region. The free flow region represents vugs, caves, and fractures while the porous region represents the matrix of porous media. On the coarse scale, the media is described mostly by Darcy flow. The fine scale features such as vugs caves and fractures along with the surrounding porous matrix are replaced by an effective material with well defined effective permeability and porosity. This would be representative of the flow in the reservoir at large scale. However certain features such as large (relative to the fine scale), long-range caves and fracture networks may still be retained.

The limitations of the multi-scale method include the need to solve over all REV's, instabilities due to poor local conservation properties, the lack of mesh adaptivity (adaptive

REV generation is not straightforward) and the difficulty of incorporating non-linear effects such as pressure dependent apparent permeability. Furthermore implementing the higher order Forchheimer term was not not straightforward.

Chapter 4
The Finite Element Method

4.1 The Finite Element Method

The Finite Element Method (FEM) is a method for numerically approximating the solution to Partial Differential Equations (PDEs). It works by finding a solution function that is made up of "shape functions" multiplied by coefficients and added together. In a sense it is just like polynomial fitting, except the functions aren't typically as simple as x^i (although they can be).

The Galerkin Finite Element method is different from finite difference and finite volume methods because it finds a piecewise continuous function which is an approximate solution to the governing PDE. Just as in polynomial fitting you can evaluate a finite element solution anywhere in the domain by adding up "shape functions" evaluated at the point and multiplied by their coefficient.

FEM is widely applicable for a large range of PDEs and domains. It is supported by a rich mathematical theory with proofs about accuracy, stability, convergence and solution uniqueness.

4.1.1 The Weak Form

Finding the solution to a PDE starts with forming a "weighted residual" or "variational statement" or "weak form". The idea behind generating a weak form is to give some flexibility, both mathematically and numerically. Generating a weak form involves the following steps:

1. Starting from the strong form of PDE (the original form of the PDE)
2. Rearrange terms so that the right hand side is zero
3. Multiply the whole equation with a test function ψ
4. Integrate the whole equation over the domain Ω

5. Integrate by parts using the divergence theorem to get the desired derivative order and generate boundary integrals

4.1.2 The Divergence Theorem

Since we will be using the divergence theorem extensively in the next chapters it is worthwhile to include it here. The divergence theorem is generally expressed as follows:

$$\int_{\Omega} \nabla \cdot \vec{g} \, \mathrm{d}x = \int_{\partial\Omega} \vec{g} \cdot \hat{n} \, \mathrm{d}s \tag{4.1}$$

Let $\vec{g} = -k(x)\nabla u$, then divergence theorem implies:

$$-\int_{\Omega} \psi \left(\nabla \cdot k(x)\nabla u\right) \, \mathrm{d}x = \int_{\Omega} \nabla\psi \cdot k(x)\nabla u \, \mathrm{d}x - \int_{\partial\Omega} \psi \left(k(x)\nabla u \cdot \hat{n}\right) \, \mathrm{d}s \tag{4.2}$$

We often use the inner product notation to represent integrals since it is far more compact:

$$-\left(\psi, \nabla \cdot k(x)\nabla u\right) = \left(\nabla\psi, k(x)\nabla u\right) - \langle \psi, k(x)\nabla u \cdot \hat{n} \rangle \tag{4.3}$$

4.1.3 Computing The Residual

The discretized expansion of u takes the form: $u \approx u_h = \sum_{j=1}^{N} u_j \phi_j$ where ϕ_j are called the "basis functions" which form the basis of the "trial function": u_h. The gradient of u can be expanded similarly: $\nabla u \approx \nabla u_h = \sum_{j=1}^{N} u_j \nabla\phi_j$. The test functions functions can also be expanded: $\psi = \{\psi_i\}_{i=1}^{N}$.

Substituting back into the weak form we get:

$$\left(\nabla\psi_i, k\nabla u_h\right) - \langle \psi_i, k\nabla u_h \cdot \hat{n} \rangle + \left(\psi_i, \vec{\beta} \cdot \nabla u_h\right) - \left(\psi_i, f\right) = 0, \quad i = 1, \ldots, N \tag{4.4}$$

The left-hand side of the equation above is referred to as the i^{th} component of the residual vector $R_i(u_h)$.

The domain integral over Ω can be split into the sum of integrals over individual elements:

$$\int_{\Omega} f(\vec{x})\ \mathrm{d}\vec{x} = \sum_{e} \int_{\Omega_e} f(\vec{x})\ \mathrm{d}\vec{x} \tag{4.5}$$

Through a change of variables, the element integrals are mapped to integrals over the reference elements $\hat{\Omega}_e$.

$$\sum_{e} \int_{\Omega_e} f(\vec{x})\ \mathrm{d}\vec{x} = \sum_{e} \int_{\hat{\Omega}_e} f(\vec{\xi})\,|\mathcal{J}_e|\ \mathrm{d}\vec{\xi} \tag{4.6}$$

where $\mathcal{J}_e$ is the Jacobian of the map from physical element to reference element. To approximate the reference element integrals numerically, we have to use quadrature rules (typically "Gaussian Quadrature"):

$$\sum_{e} \int_{\hat{\Omega}_e} f(\vec{\xi})\,|\mathcal{J}_e|\ \mathrm{d}\vec{\xi} \approx \sum_{e} \sum_{qp} w_{qp} f(\vec{x}_{qp})\,|\mathcal{J}_e(\vec{x}_{qp})| \tag{4.7}$$

where $\vec{x}_{qp}$ is the spatial location of the qp^{th} quadrature point and w_{qp} is its associated weight. Sampling u_h at quadrature points yields:

$$u(\vec{x}_{qp}) \approx u_h(\vec{x}_{qp}) = \sum u_j \phi_j(\vec{x}_{qp}) \tag{4.8}$$

$$\nabla u(\vec{x}_{qp}) \approx \nabla u_h(\vec{x}_{qp}) = \sum u_j \nabla \phi_j(\vec{x}_{qp}) \tag{4.9}$$

and the weak form becomes:

$$R_i(u_h) = \sum_{e} \sum_{qp} w_{qp}\,|\mathcal{J}_e| \left[\nabla \psi_i \cdot k \nabla u_h + \psi_i \left(\vec{\beta} \cdot \nabla u_h\right) - \psi_i f\right](\vec{x}_{qp}) \tag{4.10}$$

$$- \sum_{f} \sum_{qp_{face}} w_{qp_{face}}\,|\mathcal{J}_f|\,[\psi_i k \nabla u_h \cdot \vec{n}]\,(\vec{x}_{qp_{face}}) \tag{4.11}$$

4.2 The FEM Implementations

4.2.1 The Moose Framework

The Multiphysics Object-Oriented Simulation Environment (MOOSE) (Tonks et al. 2012) is a finite- element, multiphysics framework primarily developed at the Idaho National Laboratory. It provides a high-level interface to sophisticated nonlinear solvers including PETSc (Balay et al. 1997), Trilinos among others. Other MOOSE framework features of relevance include:

- Fully-coupled, fully-implicit multiphysics solver
- Dimension independent physics
- Automatically parallel (largest runs $> 100,000$ CPU cores)
- Modular development
- Built-in mesh adaptivity
- Intuitive parallel multiscale solves

Other frameworks that we investigated include FEniCS, Deal.II, libMesh, PETSc, OOFEM and Nektar++. These frameworks were rejected for various reasons including scalability, inaccessible low level controls, unstable interfaces, mesh import issues and so on.

4.2.2 Finite Element Methods with Moose

Consider the convection-diffusion equation:

$$-\nabla \cdot k\nabla u + \vec{\beta} \cdot \nabla u = f \tag{4.12}$$

Re-arranging to a zero right hand side:

$$-\nabla \cdot k\nabla u + \vec{\beta} \cdot \nabla u - f = 0 \tag{4.13}$$

Multiplying by the test function ψ:

$$-\psi\nabla\cdot k\nabla u+\psi\vec{\beta}\cdot\nabla u-\psi f=0 \tag{4.14}$$

Integrating over the domain Ω:

$$-\int_{\Omega}\psi\left(\nabla\cdot k\nabla u\right)+\int_{\Omega}\psi\left(\vec{\beta}\cdot\nabla u\right)-\int_{\Omega}\psi f=0 \tag{4.15}$$

Applying the divergence theorem to the diffusion term (to avoid second order derivatives):

$$\int_{\Omega}\nabla\psi\cdot k\nabla u-\int_{\partial\Omega}\psi\left(k\nabla u\cdot\hat{n}\right)+\int_{\Omega}\psi\left(\vec{\beta}\cdot\nabla u\right)-\int_{\Omega}\psi f=0 \tag{4.16}$$

The C++ code in MOOSE will be based on the inner product notation. Each portion of the equation will inherit from an existing MOOSE type and implement MOOSE functions:

$$\underbrace{\left(\nabla\psi,k\nabla u\right)}_{Kernel}-\underbrace{\left\langle\psi,k\nabla u\cdot\hat{n}\right\rangle}_{BoundaryCondition}+\underbrace{\left(\psi,\vec{\beta}\cdot\nabla u\right)}_{Kernel}-\underbrace{\left(\psi,f\right)}_{Kernel}=0 \tag{4.17}$$

4.2.3 Newton's Method

We have assembled a nonlinear system of equations: $R_i(u_h)=0, \qquad i=1,\ldots,N$ to solve for the coefficients $u_j, j=1,\ldots,N$. Newton's method is a root finding method, it finds zeros of nonlinear equations and has good convergence properties. The typical form of Newton's method is the update form where an intermediate solution is updated to convergence. For example, to find roots of the scalar function $f(x):\mathbb{R}\rightarrow\mathbb{R}$ we calculate its derivative and update x_n:

$$f'(x_n)\delta x_{n+1}=-f(x_n) \tag{4.18}$$

$$x_{n+1}=x_n+\delta x_{n+1} \tag{4.19}$$

Since we have a system of nonlinear equations, Newton's method takes the following form:

$$\mathbf{J}(\vec{u}_n)\delta\vec{u}_{n+1} = -\vec{R}(\vec{u}_n) \tag{4.20}$$

$$\vec{u}_{n+1} = \vec{u}_n + \delta\vec{u}_{n+1} \tag{4.21}$$

where $\mathbf{J}(\vec{u}_n)$ is the Jacobian matrix evaluated at the current iterate:

$$J_{ij}(\vec{u}_n) = \frac{\partial R_i(\vec{u}_n)}{\partial u_j} \tag{4.22}$$

Note that:

$$\frac{\partial u_h}{\partial u_j} = \sum_k \frac{\partial}{\partial u_j}\left(u_k\phi_k\right) = \phi_j \qquad \frac{\partial\left(\nabla u_h\right)}{\partial u_j} = \sum_k \frac{\partial}{\partial u_j}\left(u_k\nabla\phi_k\right) = \nabla\phi_j \tag{4.23}$$

Consider the convection-diffusion equation with nonlinear k, $\vec{\beta}$ and f, where the i^{th} component of the residual vector is:

$$R_i(u_h) = (\nabla\psi_i, k\nabla u_h) - \langle\psi_i, k\nabla u_h\cdot\hat{n}\rangle + \left(\psi_i, \vec{\beta}\cdot\nabla u_h\right) - (\psi_i, f) \tag{4.24}$$

using the rules for $\frac{\partial u_h}{\partial u_j}$ and $\frac{\partial(\nabla u_h)}{\partial u_j}$ the (i,j) entry of the Jacobian is then:

$$J_{ij}(u_h) = \left(\nabla\psi_i, \frac{\partial k}{\partial u_j}\nabla u_h\right) + (\nabla\psi_i, k\nabla\phi_j) - \left\langle\psi_i, \frac{\partial k}{\partial u_j}\nabla u_h\cdot\hat{n}\right\rangle \tag{4.25}$$

$$- \langle\psi_i, k\nabla\phi_j\cdot\hat{n}\rangle + \left(\psi_i, \frac{\partial\vec{\beta}}{\partial u_j}\cdot\nabla u_h\right) + \left(\psi_i, \vec{\beta}\cdot\nabla\phi_j\right) - \left(\psi_i, \frac{\partial f}{\partial u_j}\right) \tag{4.26}$$

and applying the chain rule:

$$\frac{\partial f}{\partial u_j} = \frac{\partial f}{\partial u_h}\frac{\partial u_h}{\partial u_j} \tag{4.27}$$

$$= \frac{\partial f}{\partial u_h}\phi_j \tag{4.28}$$

The Jacobian can be expressed as:

$$J_{ij}(u_h) = \left(\nabla\psi_i, \frac{\partial k}{\partial u_h}\phi_j \nabla u_h\right) + (\nabla\psi_i, k\nabla\phi_j) - \left\langle \psi_i, \frac{\partial k}{\partial u_h}\phi_j \nabla u_h \cdot \hat{n}\right\rangle \tag{4.29}$$

$$- \langle \psi_i, k\nabla\phi_j \cdot \hat{n}\rangle + \left(\psi_i, \frac{\partial \vec{\beta}}{\partial u_h}\phi_j \cdot \nabla u_h\right) + \left(\psi_i, \vec{\beta}\cdot\nabla\phi_j\right) - \left(\psi_i, \frac{\partial f}{\partial u_h}\phi_j\right) \tag{4.30}$$

This is the basic procedure we will follow for all MOOSE kernels. Note that **J** is never explicitly needed to construct the Krylov subspace: only the action of J on a vector is required:

$$\mathbf{J}\vec{v} \approx \frac{\vec{R}(\vec{u}+\epsilon\vec{v}) - \vec{R}(\vec{u})}{\epsilon} \tag{4.31}$$

This has the added advantage of avoiding analytic derivatives to form **J**, no resources required to compute **J** (just residual computations) and no space needed to store **J**.

Chapter 5
Finite Elements Implementation

5.1 FEM Reservoir Implementation

We will apply the FEM approach from 4.2 to the following flow equations:

- Compressible single phase Darcy flow model
- Compressible single phase Darcy flow model with pressure dependent apparent permeability correction
- Compressible single phase Darcy flow model with dual porosity dual permeability and fluid exchange rate
- Compressible single phase Forchheimer flow model
- Adsorption-Desorption model

5.1.1 Compressible Single Phase Flow Model

The mass conservation equation for single phase flow is typically expressed as:

$$\frac{\partial(\phi\rho)}{\partial t} + \nabla \cdot (\rho \mathbf{u}) = q \tag{5.1}$$

where ϕ is the porosity, ρ is the density, t is time, $\mathbf{u}$ is the superficial Darcy velocity and q the external sources and sinks.

The superficial Darcy velocity $\mathbf{u}$ is typically obtained from Darcy's law:

$$\mathbf{u} = -\frac{1}{\mu}\mathbf{k}(\nabla p - \rho \wp \nabla z) \tag{5.2}$$

where $\mathbf{k}$ is the absolute permeability tensor of the porous media, $\wp$ is the magnitude of the gravitational acceleration and z is the depth.

Equations 5.1 and 5.2 are the basic equations in reservoir simulation. For compressible gas flow, where density is a function of pressure (and compressibility is not constant), the mass conservation equation 5.1 can be generalized as:

$$c(p)\frac{\partial p}{\partial t} + \nabla \cdot (\rho \mathbf{u}) = q \tag{5.3}$$

$$c(p) = \phi \frac{\partial \rho}{\partial p} + \rho \frac{d\phi}{dp} \tag{5.4}$$

substituting Darcy's law 5.2 into the compressible mass conservation equation 5.3 we arrive at the general equation:

$$c(p)\frac{\partial p}{\partial t} - \nabla \cdot (\frac{\rho}{\mu}\mathbf{k}(\nabla p - \rho \wp \nabla z)) = q \tag{5.5}$$

Ignoring the time derivative and the source/sink term q for the time being we will focus on the flux term and its contribution to the residual. Multiplying by the test function ψ:

$$-\nabla \cdot \left(\frac{\rho}{\mu}\mathbf{k}\left(\nabla p - \rho \wp \nabla z\right) \right) \psi = 0 \tag{5.6}$$

applying the divergence theorem and integrating by parts over the whole domain Ω:

$$-\int_{\partial\Omega} \psi \frac{\rho}{\mu}\mathbf{k}\left(\nabla p - \rho \wp \nabla z\right) \cdot \hat{n} + \int_{\Omega} \nabla\psi \cdot \frac{\rho}{\mu}\mathbf{k}\left(\nabla p - \rho \wp \nabla z\right) = 0 \tag{5.7}$$

The i^{th} entry in the residual vector for the kernel is therefore:

$$R_i = \int_{\Omega} \nabla\psi_i \cdot \frac{\rho(p_h)}{\mu}\mathbf{k}\left(\nabla p_h - \rho(p_h) \wp \nabla z\right) \tag{5.8}$$

The (i, j) entry in the Jacobian would therefore be:

$$\frac{\partial R_i}{\partial p_j} = \frac{\partial \rho}{\partial p_h}\frac{\phi_j}{\mu}\mathbf{k}\left(\nabla p_h - \rho(p_h)\wp\nabla z\right) + \frac{\rho}{\mu}\mathbf{k}\left(\nabla\phi_j - \frac{\partial\rho}{\partial p_h}\phi_j\wp\nabla z\right) \tag{5.9}$$

5.1.2 Compressible Single Phase With Apparent Permeability

If we use an apparent permeability correction term that is pressure dependent, which applies to most Knudsen diffusion corrections to apparent permeability, the apparent permeability multiplier needs to be taken account in the residual and Jacobian calculations.

The residual equation would therefore take the form:

$$R_i = \int_\Omega \nabla\psi_i \cdot \frac{\rho(p_h)}{\mu}\mathbf{k}\left(1 + \frac{b}{p_h}\right)\left(\nabla p_h - \rho(p_h)\wp\nabla z\right) \tag{5.10}$$

where b is the Klinkenberg correction factor. The (i, j) entry in the Jacobian would therefore be:

$$\frac{\partial R_i}{\partial p_j} = \frac{\partial \rho}{\partial p_h}\frac{\phi_j}{\mu}\mathbf{k}\left(1 + \frac{b}{p_h}\right)\left(\nabla p_h - \rho(p_h)\wp\nabla z\right) \tag{5.11}$$

$$-\frac{\rho}{\mu}\mathbf{k}\frac{b}{p_h^2}\phi_j\left(\nabla p_h - \rho(p_h)\wp\nabla z\right) \tag{5.12}$$

$$+\frac{\rho}{\mu}\mathbf{k}\left(1 + \frac{b}{p_h}\right)\left(\nabla\phi_j - \frac{\partial\rho}{\partial p_h}\phi_j\wp\nabla z\right) \tag{5.13}$$

5.1.3 Dual Porosity Dual Permeability Model

The dual porosity dual permeability model is based on the single phase compressible model. Two sets of equations, one for the fracture the other for the matrix are used along with a matrix-fracture transfer term.

$$c(p)\frac{\partial p_f}{\partial t} - \nabla\cdot\left(\frac{\rho(p_f)}{\mu}\mathbf{k}(\nabla p_f - \rho(p_f)\wp\nabla z)\right) + \sigma\cdot\frac{k_f}{\mu}\cdot\rho(p_f)\left(p_f - p_m\right) = q_f \tag{5.14}$$

$$c(p)\frac{\partial p_m}{\partial t} - \nabla\cdot\left(\frac{\rho(p_m)}{\mu}\mathbf{k}(\nabla p_m - \rho(p_m)\wp\nabla z)\right) + \sigma\cdot\frac{k_m}{\mu}\cdot\rho(p_m)\left(p_m - p_f\right) = q_m \tag{5.15}$$

Where σ is a geometry dependent shape factor and the subscripts f and m denote fracture and matrix respectively. Reduced to a single kernel:

$$c(p)\frac{\partial p_{primary}}{\partial t} - \nabla \cdot (\frac{\rho(p_{primary})}{\mu}\mathbf{k}(\nabla p_{primary} - \rho(p_{primary})\wp\nabla z)) \tag{5.16}$$

$$+ \sigma \cdot \frac{k_{primary}}{\mu} \cdot \rho(p_{primary})\left(p_{primary} - p_{secondary}\right) = q_{primary} \tag{5.17}$$

where $p_{primary}$ denotes the primary medium pressure and $p_{secondary}$ denotes the secondary medium pressure. The only functional difference between this kernel and the single phase flow model kernel is the matrix-fracture transfer term σ. We will therefore inherit the kernel terms from the single phase model and add the transfer term discretization.

Multiplying with the test function, the transfer term residual contribution becomes:

$$R_i = \psi_i\sigma \cdot \frac{k_{primary}}{\mu} \cdot \rho(p_h)\left(p_h - p_{secondary}\right) \tag{5.18}$$

The Jacobian contribution at i, j would therefore be:

$$\frac{\partial R_i}{\partial p_j} = \psi_i\sigma \cdot \frac{k_{primary}}{\mu} \cdot \frac{\partial \rho(p_h)}{\partial p_h}\phi_j\left(p_h - p_{secondary}\right) - \psi_i\sigma \cdot \frac{k_{primary}}{\mu} \cdot \rho(p_h)\phi_j \tag{5.19}$$

Since we are dealing with a system of equations for the fracture and matrix, we would want to use block matrix preconditioners and solvers. To do this we would have to provide the Jacobian (or a means to calculate the entries of the Jacobian) for every row and column, i.e non diagonal entries. The non-diagonal contribution of the transfer term is:

$$\frac{\partial R_i}{\partial p_{jsecondary}} = -\psi_i\sigma \cdot \frac{k_{primary}}{\mu} \cdot \rho(p_{primanry})\phi_j \tag{5.20}$$

Note that the permeability term used in this equation is not the typical permeability tensor but the geometric mean of the diagonal entries to the permeability tensor $k = \sqrt[3]{k_x k_y k_z}$.

5.1.4 Compressible Forchheimer Flow Model

The Forchheimer flow model is used in the discrete fracture model since we use a cell-average discrete fracture treatment (to avoid dealing with transfer functions). It is more complex than the other models as it contains non-linear velocity terms. We will use finite elements for the components of the velocity vector and the pressure. The equations are:

$$\text{Continuity Equation: } \nabla \cdot (\rho(p)\vec{u}) = q \tag{5.21}$$

$$\text{Momentum Equation: } -(\nabla p - \rho(p)\wp\nabla z) = \mu\vec{k}^{-1}\vec{u} + \rho(P)\beta\,|\vec{u}|\,\vec{u} \tag{5.22}$$

We do not have access to Raviart-Thomas finite elements in Moose therefore we use continuous finite elements to discretize the velocity and pressure equations. Specifically, we use mixed finite elements to ensure high order approximation for both vector (e.g. a fluid velocity) and scalar variables (e.g. pressure) simultaneously. For saddle point problems, it is well established that the so-called Babuska-Brezzi or Ladyzhenskaya-Babuska-Brezzi (LBB) conditions (Brezzi and Fortin 1991; Chen et al. 2006) need to be satisfied to ensure stability of the pressure-velocity system. These stability conditions are satisfied in the present work by using elements for velocity that are one order higher than for the pressure.

Multiplying the continuity and Forchheimer equations with test functions, we arrive at the following residual vector contributions:

$$R_i = \nabla \cdot (\rho\vec{u})\psi_i - q\psi_i = \rho\nabla \cdot (\vec{u})\psi_i + \frac{\partial\rho}{\partial p}\nabla p \cdot \vec{u}\psi_i - q\psi_i \tag{5.23}$$

$$R_i = (\nabla p - \rho(p)\wp\nabla z)\,\psi_i + \mu\vec{k}^{-1}\vec{u}\psi_i + \rho(p)\beta\,|\vec{u}|\,\vec{u}\psi_i \tag{5.24}$$

here we employed a change of variable of density to pressure using a simple chain rule: $\nabla\rho = \frac{\partial\rho}{\partial p}\nabla p$.

To make good use of the block Schur complement preconditioner we shall use pressure as the primary variable for the continuity equation and velocity components for the Forchheimer equation. This leaves us with the following diagonal Jacobian contributions:

$$\frac{\partial R_i}{\partial u_j} = \phi_j \frac{\partial \rho}{\partial p} \nabla \cdot \vec{u} \psi_i + \frac{\partial^2 \rho}{\partial p^2} \phi_j \nabla p \cdot \vec{u} + \frac{\partial \rho}{\partial p} \nabla \phi_j \cdot \vec{u} \tag{5.25}$$

$$\frac{\partial R_i}{\partial u_j} = \mu \vec{k^{-1}} \phi_j \psi_i + \rho(p) \beta * \frac{\partial |\vec{u}|}{\partial \vec{u}} \phi_j \vec{u} \psi_i + \rho(p) \beta |\vec{u}| \phi_j \tag{5.26}$$

Since we are working with components of velocity, the magnitude of the velocity vector is: $\vec{u} = u\vec{i} + v\vec{j} + w\vec{k}$ the derivative of velocity magnitude with respect to velocity component in the x-direction is:

$$\frac{\partial |\vec{u}|}{\partial u} = \frac{\partial \sqrt[2]{u^2 + v^2 + w^2}}{\partial u} = \frac{u}{\sqrt[2]{u^2 + v^2 + w^2}} = \frac{u}{|\vec{u}|} \tag{5.27}$$

similarly for y and z directions:

$$\frac{\partial |\vec{u}|}{\partial v} = \frac{v}{|\vec{u}|} \tag{5.28}$$

$$\frac{\partial |\vec{u}|}{\partial w} = \frac{w}{|\vec{u}|} \tag{5.29}$$

Since we intend to use a block Schur complement, we would also want to compute the off-diagonal terms of the Jacobian, i.e. the derivative of the continuity residual 5.25 with respect to velocity components and the derivative of the Forchheimer equation with respect to pressure. Keeping in mind that the divergence of velocity in terms of its components is: $\nabla \cdot \vec{u} = \frac{\partial u}{\partial x} + \frac{\partial v}{\partial y} + \frac{\partial w}{\partial z}$, these contributions for the continuity equation with respect to the velocity components are as follows:

$$\frac{\partial R_i}{\partial u_j} = \rho \frac{\partial \phi_j}{\partial x} \psi_i + \frac{\partial \rho}{\partial p} \nabla p[0] \phi_j \psi_i \tag{5.30}$$

$$\frac{\partial R_i}{\partial v_j} = \rho \frac{\partial \phi_j}{\partial y} \psi_i + \frac{\partial \rho}{\partial p} \nabla p[1] \phi_j \psi_i \tag{5.31}$$

$$\frac{\partial R_i}{\partial w_j} = \rho \frac{\partial \phi_j}{\partial z} \psi_i + \frac{\partial \rho}{\partial p} \nabla p[2] \phi_j \psi_i \tag{5.32}$$

$$\tag{5.33}$$

For the Forchheimer equation the off-diagonal term is the derivative of the Forchheimer equation with one component against another, which is the derivative of the Forchheimer term. For example the derivative of the Forchheimer equation for the x-component velocity with respect to the y-component velocity is:

$$\frac{\partial R_i}{\partial u_j} = \rho \beta \phi_j \frac{v}{\sqrt[2]{u^2 + v^2 + w^2}} \psi_i \tag{5.34}$$

For the Forchheimer equation of component c, the off-diagonal pressure Jacobian contribution is:

$$\frac{\partial R_i}{\partial u_j} = (\nabla \phi_j[c] - \frac{\partial \rho}{\partial p} \phi_j \wp \nabla z) \psi_i + \frac{\partial \rho}{\partial p} \phi_j \beta \left| \vec{u} \right| \vec{u}[c] \psi_i \tag{5.35}$$

Chapter 6
Verification, Validation and Features

6.1 Verification and Validation Studies

6.1.1 Basic Incompressible Darcy Flow

We first start by verifying the compressible Klinkenberg kernel against a simple analytical case: incompressible cylindrical flow without gravity. The basic parameters are as follows:

- Permeability $k = 1.5$ MD
- Viscosity $\mu = 0.8$ cp
- Well pressure (inner wall pressure) $P_w = 10$ psi
- Reservoir pressure (outer wall pressure) $P_e = 100$ psi
- Well (inner) radius $R_w = 1$ ft
- Reservoir (outer) radius $R_e = 10$ ft

The analytical solution is given by:

$$Q = \frac{2\pi kh(P_e - P_w)}{\mu Ln(R_e/R_w)} \tag{6.1}$$

$$P(r) = P_w + \frac{Q\mu}{2\pi kh} Ln(\frac{r}{R_w}) \tag{6.2}$$

We create a mesh with Cubit/Trelis, import into MOOSE and run. Figures 6.1 and 6.2 show the results for this basic mesh. The numerical solution agrees with the analytic solution.

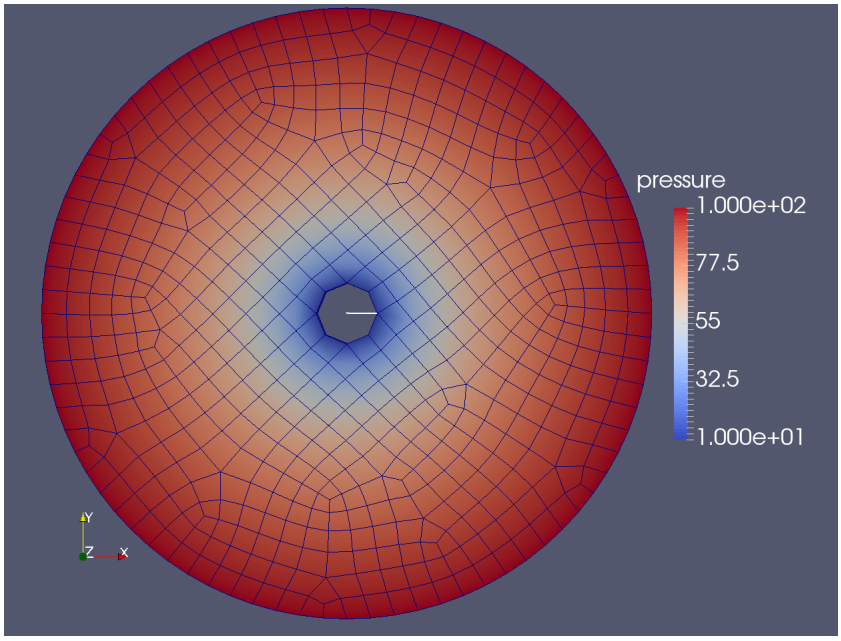

Figure 6.1: The numerical solution plotted in paraview with the mesh. Note the inner and outer boundary conditions for pressure, 10 and 100 respectively

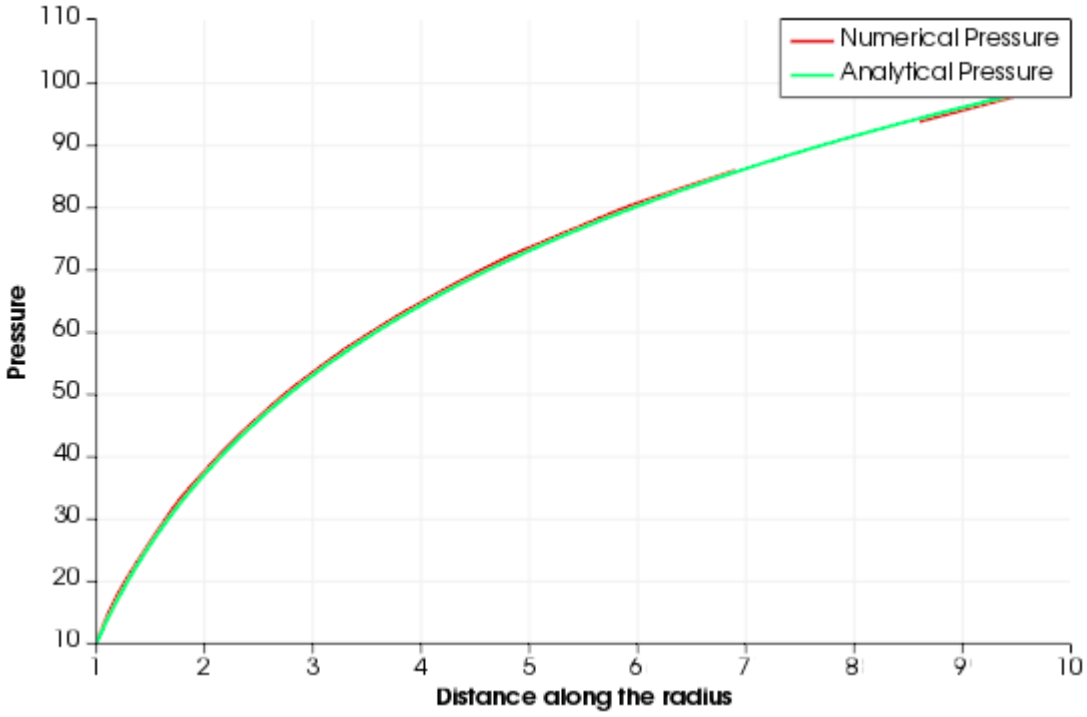

Figure 6.2: The numerical solution plotted along a line, along with the analytical solution. Results were identical to the 8th significant digit

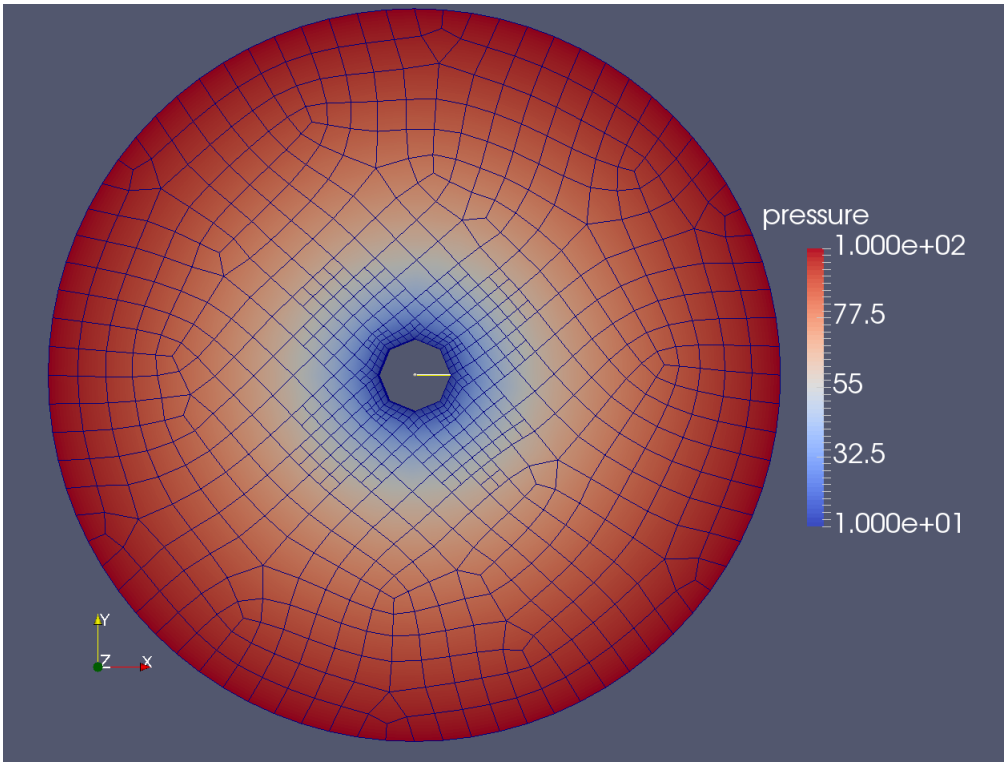

Figure 6.3: The same numerical solution but with AMR enabled, 0.5 refinement fraction

Figures 6.3 and 6.4 show the same problem but with adaptive mesh refinement enabled. The gradient of the variable (i.e. the pressure) is used as an indicator and a maximum fraction of 0.5 of the mesh can be refined. In this particular case only two levels of refinement are allowed.

With a coarse mesh, the AMR capability is easier to highlight. The same radial flow problem is solved with a 0.5 refinement fraction and a 2-step refinement process. Figures 6.5 and 6.6 show coarse and fine meshes respectively. The error fraction marker, computed based on the error gradient indicator, is shown in Figure 6.7. Note that due to the limit imposed on the number of refined and coarsened cells, the error fraction marker is not zero everywhere.

6.1.2 Compressible Klinkenberg Flow

Method of Manufactured Solutions (MMS) is a useful tool for code verification. The method works by assuming a solution, substituting it into the PDE, and obtaining a forcing

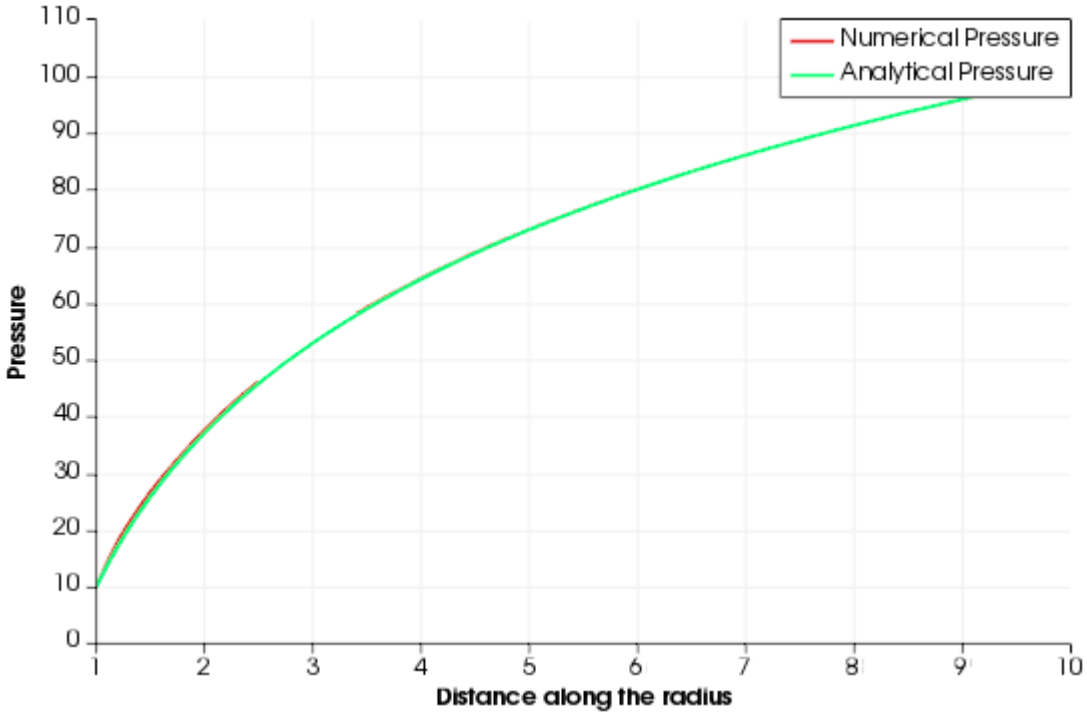

Figure 6.4: The numerical solution plotted along a line, along with the analytical solution but with AMR enabled, 0.5 refinement fraction

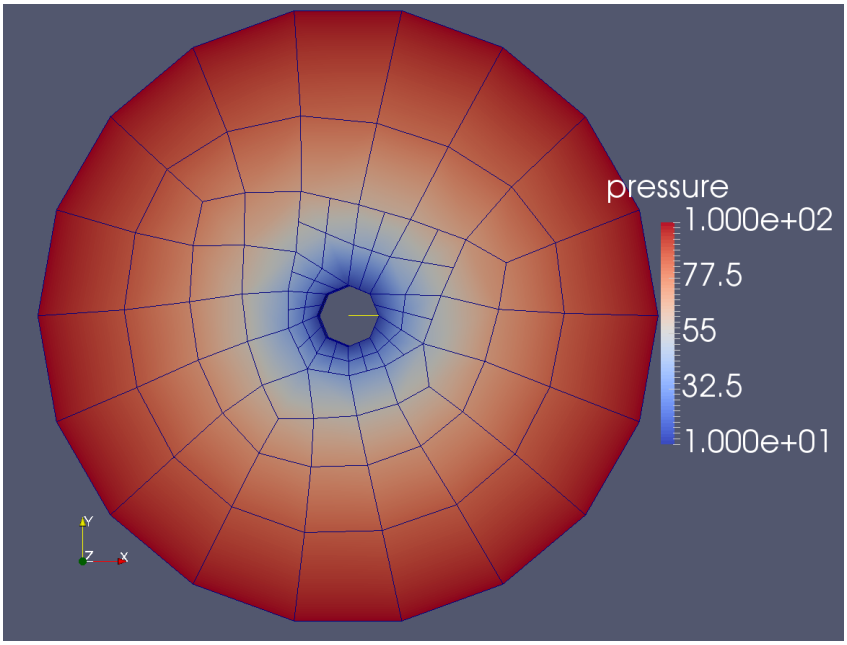

Figure 6.5: Coarse mesh radial flow

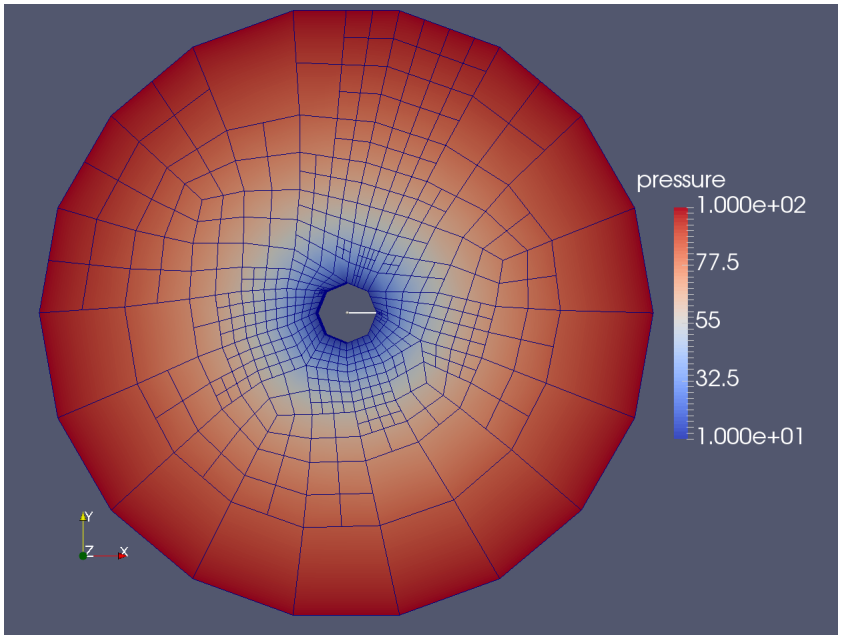

Figure 6.6: Refined mesh (second step)

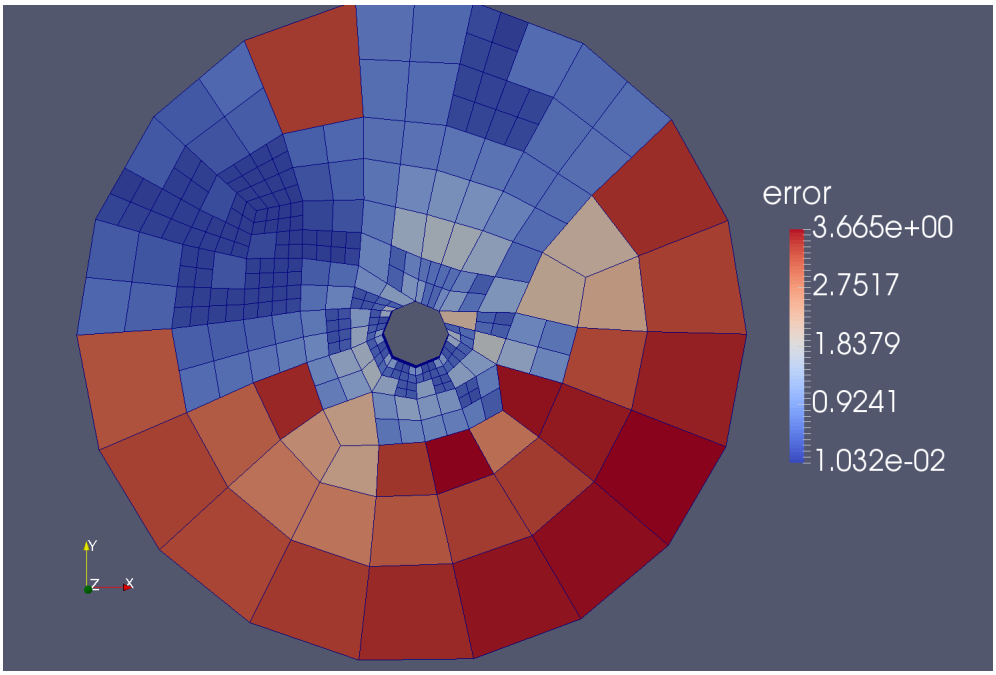

Figure 6.7: The error fraction marker used to refine the mesh

term. The modified PDE (with forcing term added) is then solved numerically; the result can be compared to the assumed solution along multiple refinements.

For this problem (firugre 6.8) we setup a simple compressible Darcy flow with pressure dependent apparent permeability correction (i.e. Klinkenberg permeability). The mesh is a simple 2D mesh with a range (0,1). The model parameters are as follows:

- Left boundary condition pressure = 1.0
- Right boundary condition pressure = $e^{-1} = 0.368...$
- Gas density Model: bulk density model, initial density 0.7 and bulk modulus 1.4
- Fluid viscosity 1
- Klinkenberg Factor 0.25

The analytical solution for pressure in this problem setup is $p = e^{-x^2}$, hence the left boundary condition of 1 and the right boundary condition of $e^{-1} = 0.368....$ The Klinkenberg permeability factor is 0.25, hence the apparent permeability $\mathbf{K}_a = \mathbf{K}(1 + \frac{0.25}{pressure})$. We use a simple density model $\rho(pressure) = \rho_0 e^{\left(\frac{pressure}{bulkmodulus}\right)}$ and with our parameters the density equation is: $\rho(pressure) = 0.7e^{\left(\frac{pressure}{1.4}\right)}$.

Figures 6.8 and 6.9 show the numerical manufactured solution and the numerical solution plotted against a line and compared to the analytic solution. Note that even with simple density models, the forcing function can be elaborate. For example the following is the forcing function as specified in the Moose input file:

```
function ='-2.8*(0.714285714285714*x
*exp(-x*x)+x)*x*(0.25*exp(x*x)+1)*
exp(-x*x+0.714285714285714*exp(-x*x))
+0.70*x*x*exp(0.714285714285714*exp(-x*x))
+1.4*(0.25*exp(x*x)+1)
*exp(-x*x+0.714285714285714*exp(-x*x))'
```

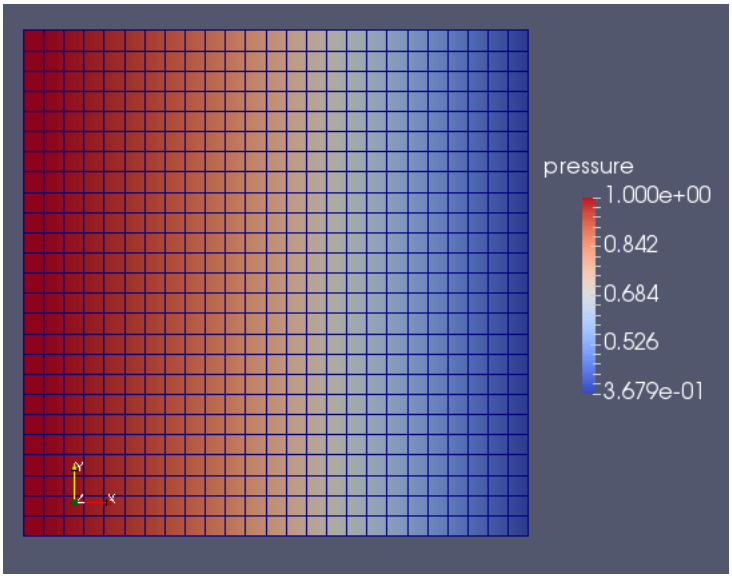

Figure 6.8: Simple 2D automatically generated mesh with simple left-right boundary conditions for the analytic solution $p = e^{-x^2}$

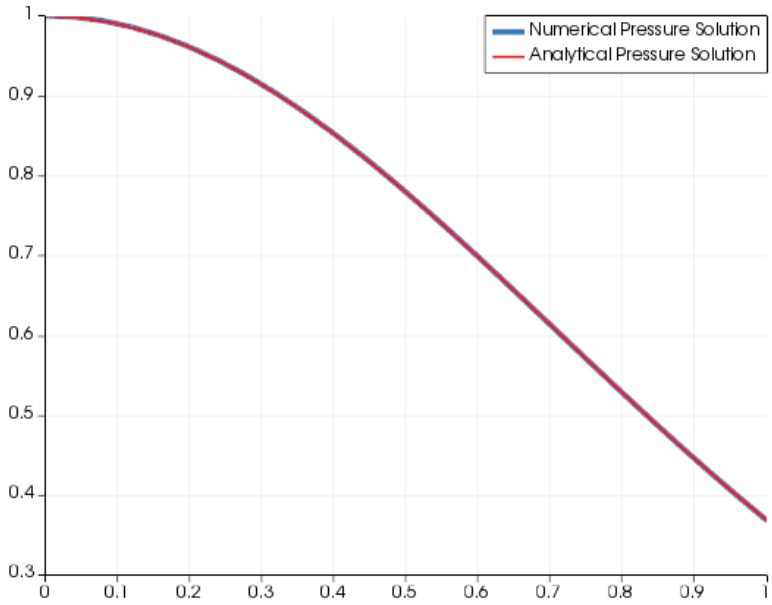

Figure 6.9: Numerical versus analytic solutions along the x-axis. The values are identical up to the 8th decimal point

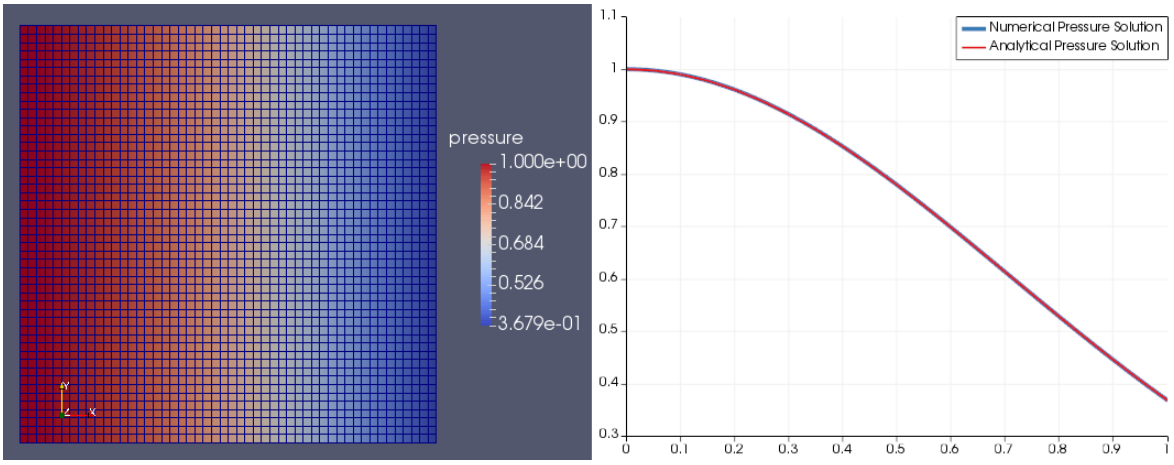

Figure 6.10: The problem solved on a 50x50 mesh

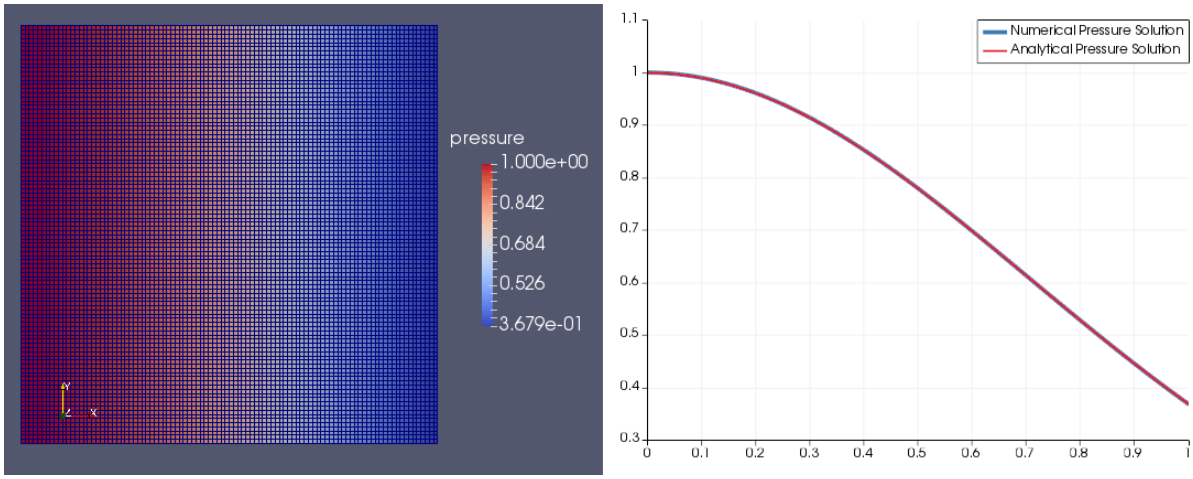

Figure 6.11: The same problem solved on a finer, 100x100 mesh

Available density models include ideal gas law and Van Der Waals. The first and second derivatives of density are also available for use with Jacobian and off-diagonal Jacobian blocks. The only reason a more complex density model was not chosen was the difficulty in generating a forcing function within the 256 character buffer limit.

Successive mesh refinement displays expected results: Figures 6.10 and 6.11 show the solution on a 50x50 and 100x100 mesh.

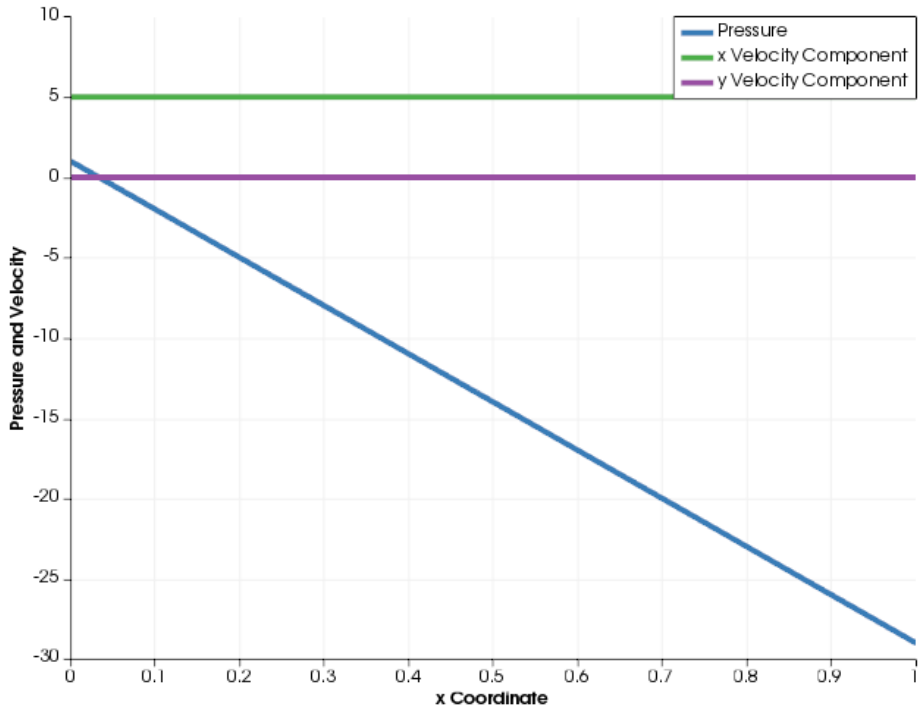

Figure 6.12: Linear pressure profile, constant velocity for incompressible Forchheimer flow

6.1.3 Forchheimer equation

The first test on the Forchheimer equation is a simple linear test to verify the higher order velocity term. We impose simple Dirichlet boundary conditions on pressure and incompressible flow. A left pressure boundary condition of 1 and right boundary condition of -29 are imposed on a 2D uniform grid.

In an incompressible flow, the divergence of velocity is zero, therefore the velocity components are uniform in their respective directions (u,v,w=constants). This coupled with the now 1-dimensional Forchheiemer equation makes the analytic solution rather simple: a linear pressure: $pressure = -30x + 1$ and a uniform x-velocity of 5 for a density and Forchheimer factor of 1. Figure 6.12 shows the numerical solution plotted over the x-axis (extracted from figure 6.13).

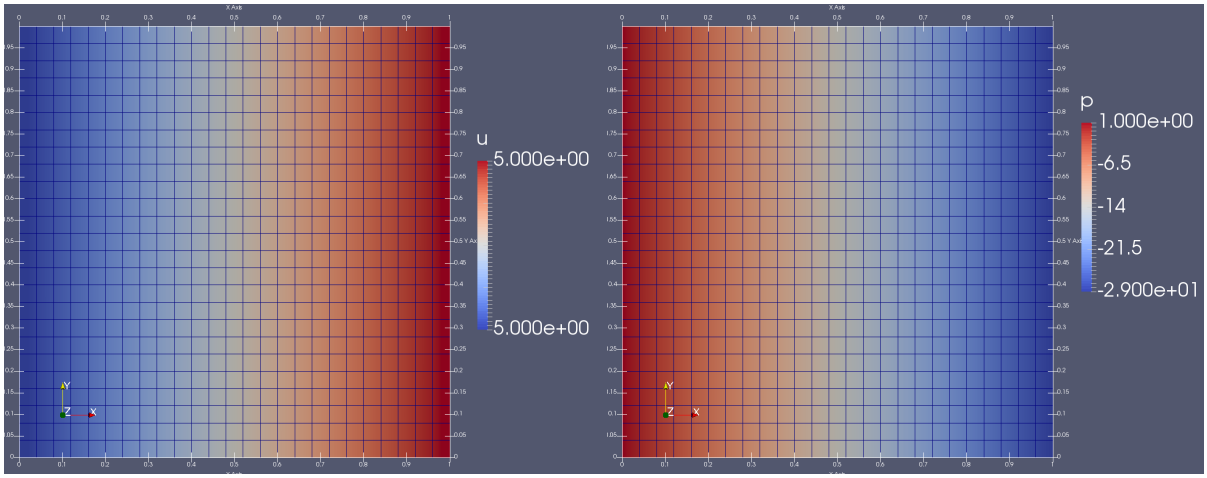

Figure 6.13: The 2D numerical solution for a linear Forchheimer velocity flow

6.1.4 Adsorption-Desorption

A simple test with initial concentration of 1, pressure=1, $\tau = 1.1$, Langmuir density of 0.88, Langmuir pressure of 1.23 is run from from $t = 0$ to $t = 2$ and the results are compared against analytic solution. Figure 6.14 shows the results comparing the analytic and numerical solutions.

6.1.5 Buckley-Leverett Problem

The FEM code can run in multiphase mode but with some restrictions due to instability and convergence problems. For example high flow rates (high β factors) cause problems with the upwinding terms that we add to reduce numerical diffusion.

These upwinding terms can easily cause large residuals leading to divergence in the solver unless an appropriate combination of initial condition, preconditioner and timestep are selected. In a sense the "mechanics" of the fully implicit multiphase flow work, but only in very specific cases.

Figures 6.15 and 6.16 show a typical one-dimensional oil-water Buckley-Leverett problem with a classic streamline upwinded Petrov-Galerkin stabilization. Note that at early time and halfway before water breakthrough the saturation front is smeared even with adaptive mesh refinement turned on.

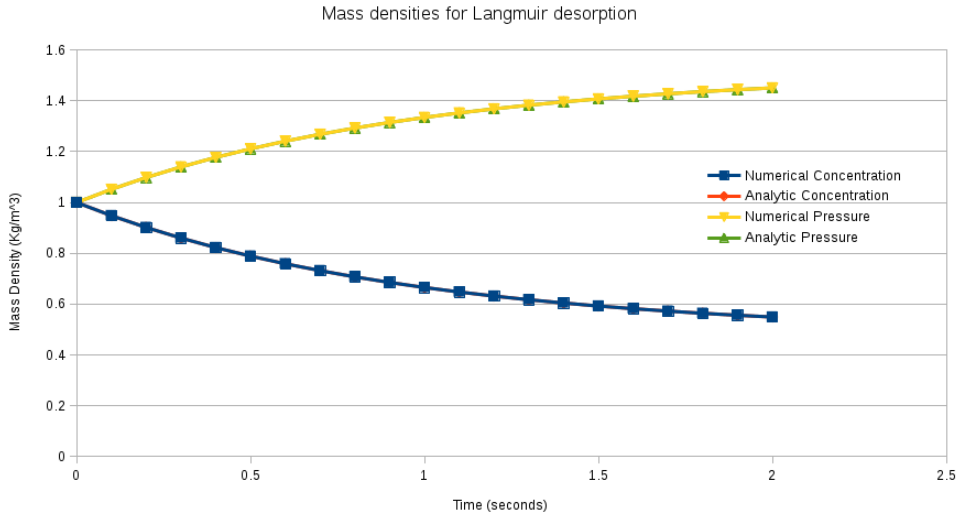

Figure 6.14: Comparison of pressure and concentration (density) obtained from numerical and analytic solutions of Langmuir model

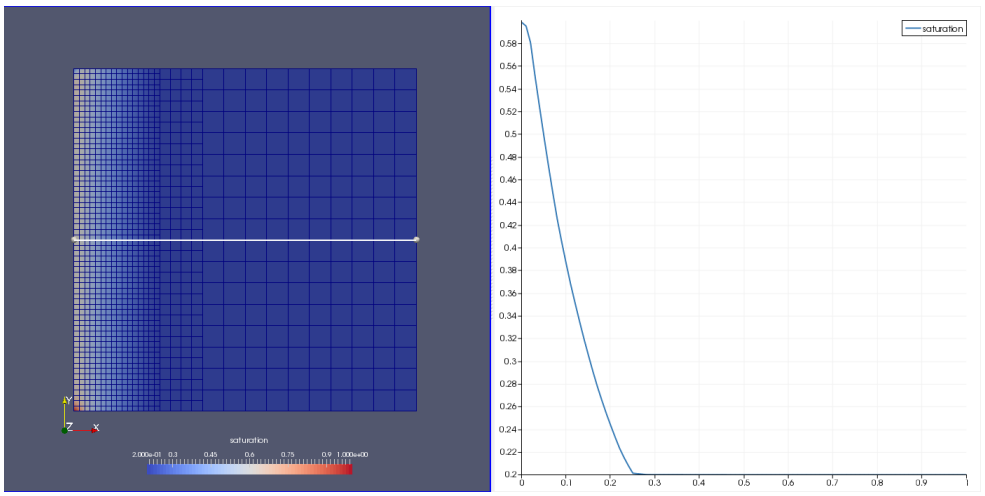

Figure 6.15: Water saturation at early time

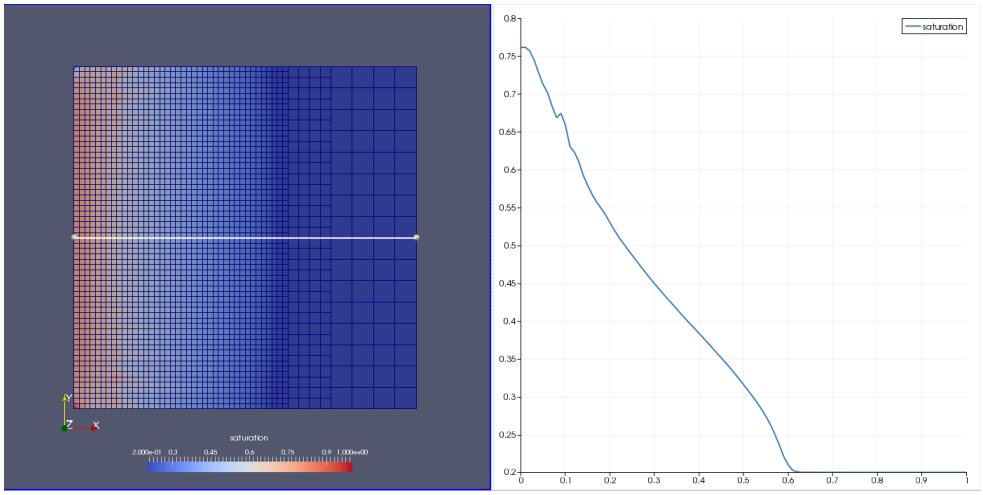

Figure 6.16: Water saturation at halfway before water breakthrough

To improve the stability and shock capturing we use an advanced artificial diffusion term that is based on the fully upwinded numerical flux on the boundary of each cell as suggested by Guermond and Pasquetti (2008).

The time-dependent saturation equation is as follows:

$$\epsilon\left(\frac{S^{(n-1)}-S^{(n)}}{\Delta t_c^{(n)}}\right)+\mathbf{u}_t^{(n)}\cdot\nabla F\left(S^{(n-1)}\right)+F\left(S^{(n-1)}\right)\nabla\cdot\mathbf{u}_t^{(n)}=0 \tag{6.3}$$

where $S^{(n)}$ is the saturation at the current n time step and $\mathbf{u_t}$ is the total phase velocity: $\mathbf{u_t}=\mathbf{u_o}+\mathbf{u_w}$. $F(S)$ is the saturation dependent advected quantity:

$$F(S)=\frac{k_{rw}(S)/\mu_w}{k_{rw}(S)/\mu_w+k_{ro}(S)/\mu_o},$$

To obtain the weak formulation from equation 6.3 we multiply with the test function σ and add the artificial diffusion term $\nu(S)$:

$$\left(\epsilon\frac{\partial S}{\partial t},\sigma\right)-\left(\mathbf{u}_tF\left(S\right),\nabla\sigma\right)+\left(\mathbf{n}\cdot\mathbf{u}_t\hat{F}\left(S\right),\sigma\right)_{\partial\Omega}+\left(\nu(S)\nabla S,\nabla\sigma\right)=0$$

where ν is the artificial diffusion term and $\hat{F}$ is the fully upwinded advection term. Following Guermond and Pasquetti (2008) we apply the parameter ν as a piecewise constant (C^0) function on each cell K with diameter h_K as follows:

$$\nu(S_h)|_K = \beta \|\mathbf{u}_t \max\{F'(S_h), 1\}\|_{L^\infty(K)} \min\left\{h_K, h_K^\alpha \frac{\|\mathrm{Res}(S_h)\|_{L^\infty(K)}}{c(\mathbf{u}_t, S)}\right\}$$

where α is a stabilization exponent and β is a dimensionless user-defined stabilization constant. The velocity and saturation global normalization constant $c(\mathbf{u_t}, S)$ and the residual term $\mathrm{Res}(S)$ are given by:

$$c(\mathbf{u}_t, S) = c_R \|\mathbf{u}_t \max\{F'(S), 1\}\|_{L^\infty(\Omega)} \mathrm{var}(S)^\alpha |\mathrm{diam}(\Omega)|^{\alpha-2}$$

and:

$$\mathrm{Res}(S) = \left(\epsilon \frac{\partial S}{\partial t} + \mathbf{u}_t \cdot \nabla F(S) + F(S) q\right) \cdot S^{\alpha-1}$$

c_R is another dimensionless user-defined constant. $\mathrm{diam}(\Omega)$ is the diameter of the cell and $\mathrm{var}(S) = max_\Omega S - min_\Omega S = 1 - S_{wirr}$ is the range of the saturation over the entire domain. The residual term is simply the last known residual multiplied by a scaling factor.

This stabilization scheme has a number of advantages over simpler schemes such as finite volume methods or streamline upwind Petrov Galerkin (SUPG) discretizations. In particular, the artificial diffusion term acts primarily in the vicinity of discontinuities since the residual is small in areas where the saturation is smooth. It therefore provides for a higher degree of accuracy.

The problem in Figures 6.15 and 6.16 is repeated in Figures 6.17 and 6.18. Note how the front is tracked more accurately without adaptive mesh refinement and is in much better agreement with the analytical solution 6.19.

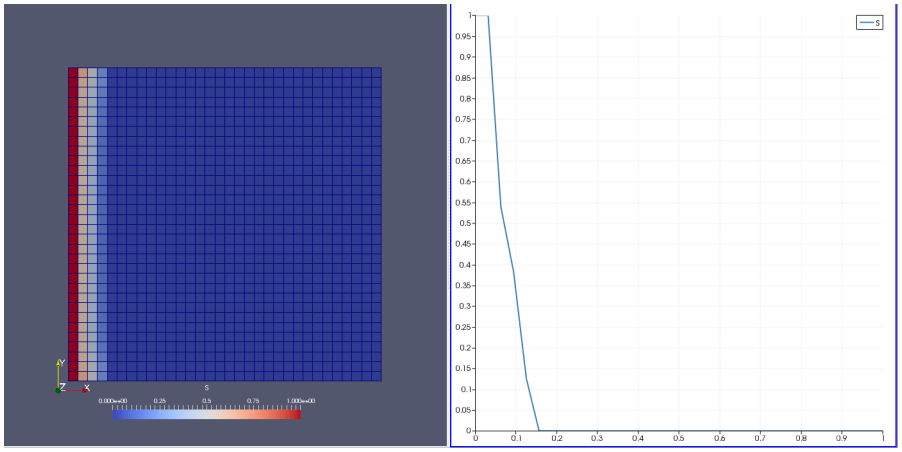

Figure 6.17: Water saturation at early time with advanced artificial diffusion

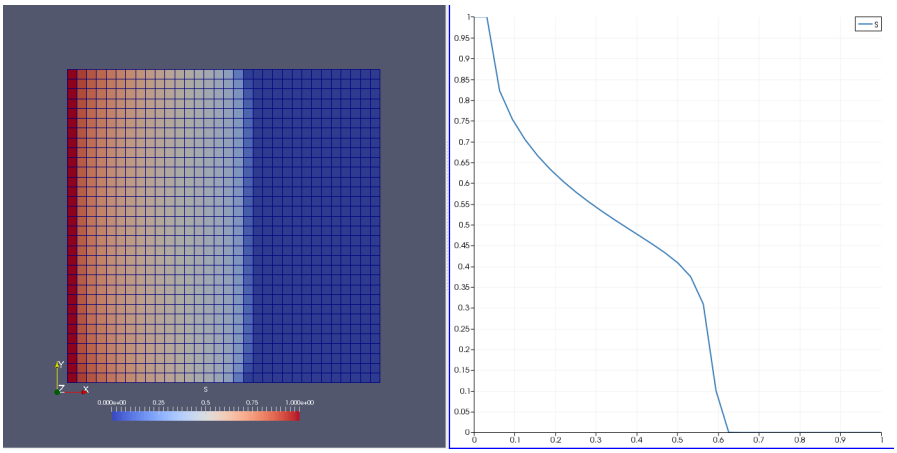

Figure 6.18: Water saturation at halfway before water breakthrough with advanced artificial diffusion

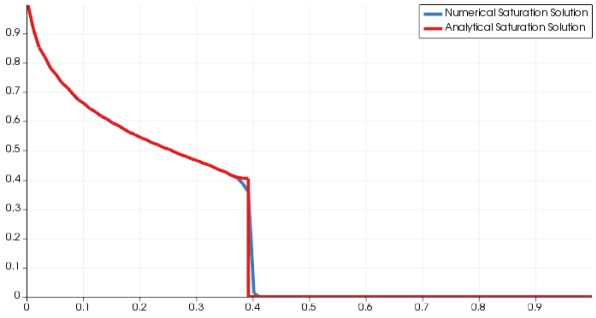

Figure 6.19: The new advanced artificial diffusion solution compared against the analytical solution

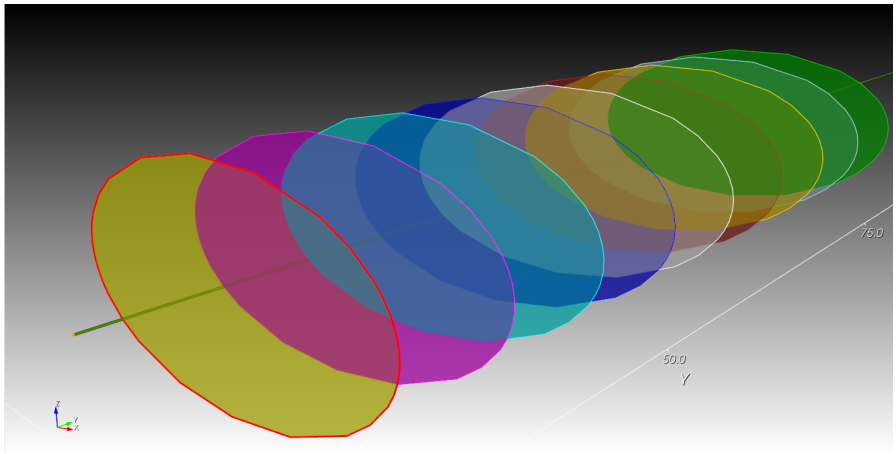

Figure 6.20: Basic Fracture geometry with $0.1m$ well diameter and ellipsoidal fractures with $10m$ major radius and $5m$ minor radius

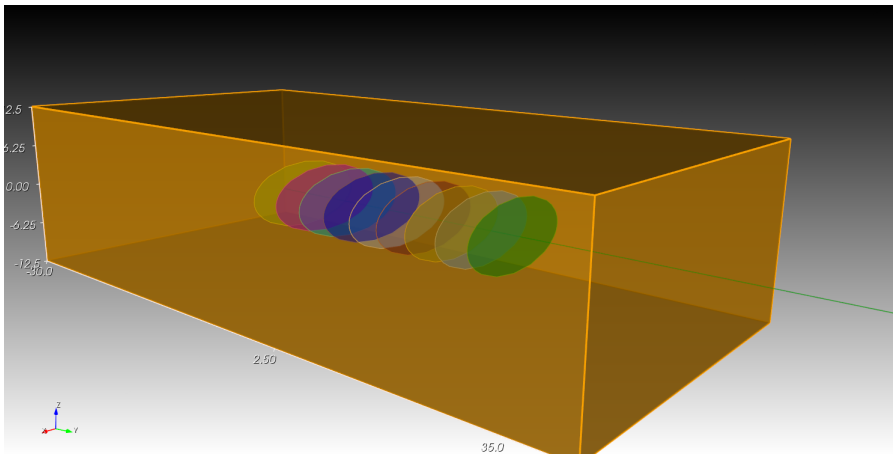

Figure 6.21: Adding the SRV and imprinting the fractures in the SRV

6.2 Mesh Generation

Good Mesh generation is a required to create accurate models, especially with hydraulically fractured reservoirs. The exodus.ii format is a logical choice as it portable across mesh readers and generators. For mesh generation we use Trelis, the commercial successor to Cubit. With a simple script it is possible to create a realistic SRV mesh. Figure 6.20 shows a fracture geometry based on ellipsoidal hydraulic fractures. Adding a simple SRV region as shown in figure 6.21 allows us to create a mesh that is suitable for suitable for adaptive mesh refinement 6.22.

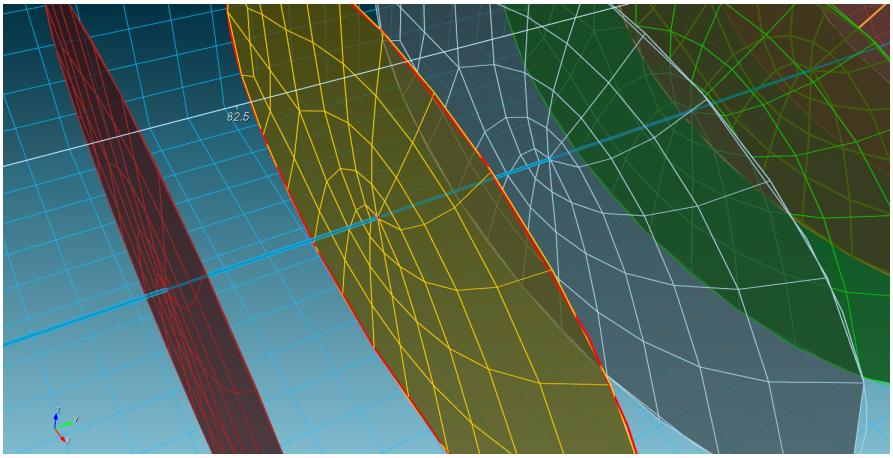

Figure 6.22: Creating a high quality coarse mesh leaves plenty of possibilities for adaptive mesh refinement at runtime

6.2.1 Simple Two-Block Verification

A major design aspect of the research reservoir simulator is the ability to handle mesh blocks. Consider the simplified case of two connected blocks with gravity set to zero, viscosity set to 1, the Klinkenberg factor set to 0 and with left and right pressure boundary conditions of 10 and 1. With a left block permeability of 1, a right block permeability of 10, we can compute the pressure at the interface as follows: flux across the interface is constant (conservation of mass) therefore:

$$K_1 \frac{P_{middle} - P_{left}}{\delta x} = K_2 \frac{P_{right} - P_{middle}}{\delta x} \tag{6.4}$$

$$(K_1 + K_2) P_{middle} = K_2 P_{right} + K_1 P_{left} \tag{6.5}$$

$$P_{middle} = \frac{K_2 P_{right} + K_1 P_{left}}{K_1 + K_2} = \frac{10 + 10}{11} = 1.8181... \tag{6.6}$$

Figure 6.23 shows the block structure of the mesh and Figure 6.24 shows the solution along with the a line plot over the x-axis. The pressure profile is linear and interface pressure is 1.818181 as expected.

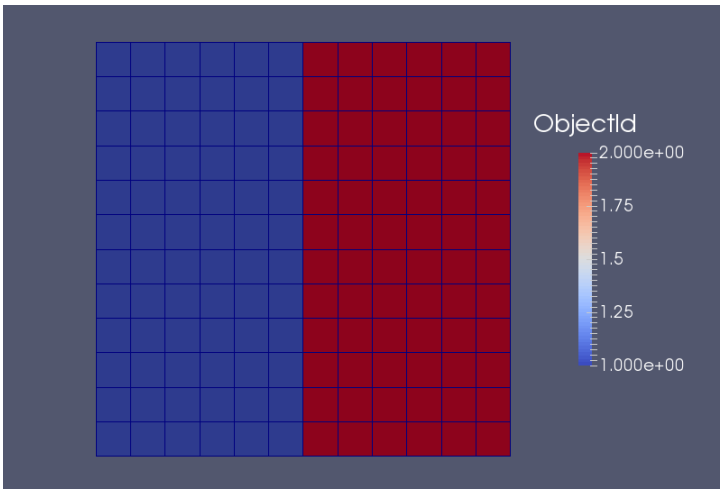

Figure 6.23: The left and right block object Id's used to label the cells

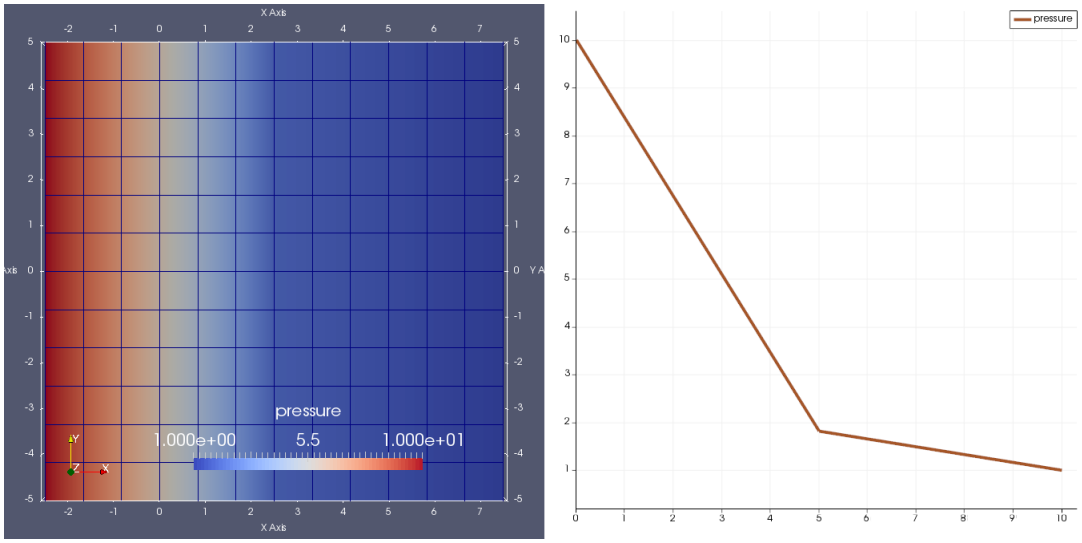

Figure 6.24: Results from the two block problem, note the correct interface pressure of 1.8181

6.2.2 Fracture Blocks

Using the mesh generation script described in section 6.2 we can create multistage fractures and explicitly simulate flow through the fractures using cell averaging. Figure 6.25 shows the results of the Klinkenberg kernel applied to both matrix and fracture. The matrix permeability in this case is 1 milli-Darcy and the fracture permeability is 10 Darcy. Note the use of tetrahedral finite elements as opposed to hexahedral elements as the research reservoir simulator supports both element types.

Figures 6.26 and 6.27 show a slice of the 85,000 degree of freedom problem. Figure 6.28 is an isosurface plot of the same slice. The boundary conditions for pressure are 100 psi on the SRV and 10 psi at the well. This model was run on a single workstation in under 5 minutes on eight cores with the an AMG preconditioner.

The same mesh generation script can be extended to generate fractal fractures. Figure 6.29 depicts a three stage fractal fracture generator with seven fracture stages. Figures 6.30 and 6.31 show the pressure solution for a 10 Darcy fracture permeability, 10 nano-Darcy matrix permeability, 1000 psi reservoir and 500 psi well flowing pressure problem. Note the size of the SRV: the bulk of the reservoir is unaffected by the pressure drop near the well or fractures.

6.3 Performance and Scalability

One of the major nonfunctional requirements of this research simulator was the use of advanced parallel computing paradigms to assure high performance and scalability. With PETSc as the solver core, this task was somewhat easy to accomplish. PETSc allows us the use of advanced features including:

- Algebraic Multigrid Preconditioner through the BoomerAMG preconditioner which is a part of HYPRe (Falgout and Yang 2002)
- GPU enabled solver (Minden et al. 2010) that uses NVIDIA's CUSP library
- Intel Xeon Phi support with the ViennaCL library (Tillet et al. 2013)

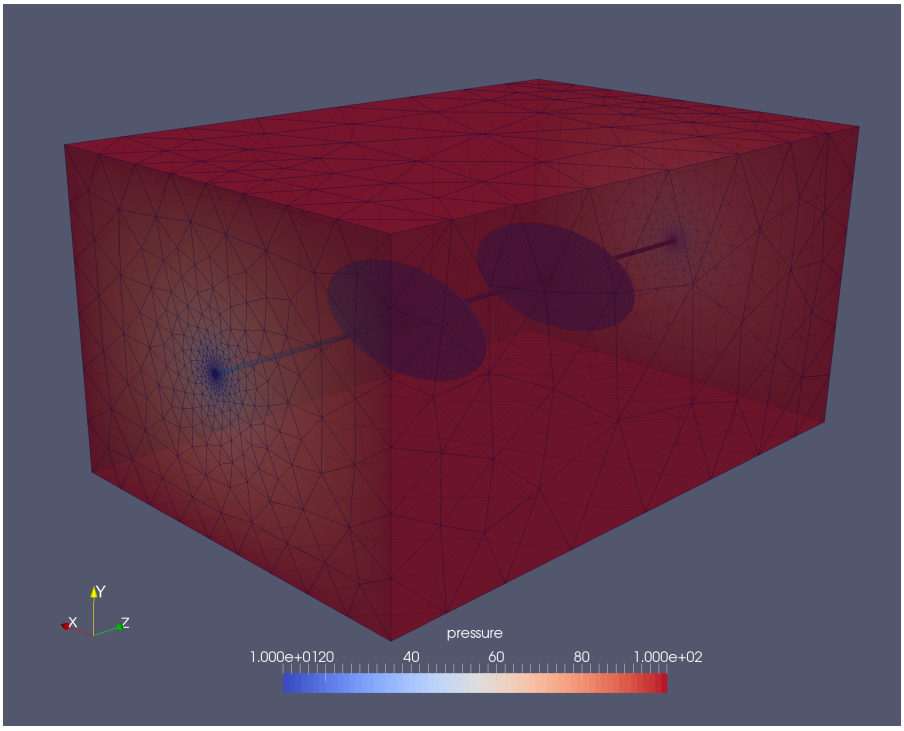

Figure 6.25: Simple two fracture problem with boundary conditions on well and reservoir extent. The Fracture is modeled explicitly

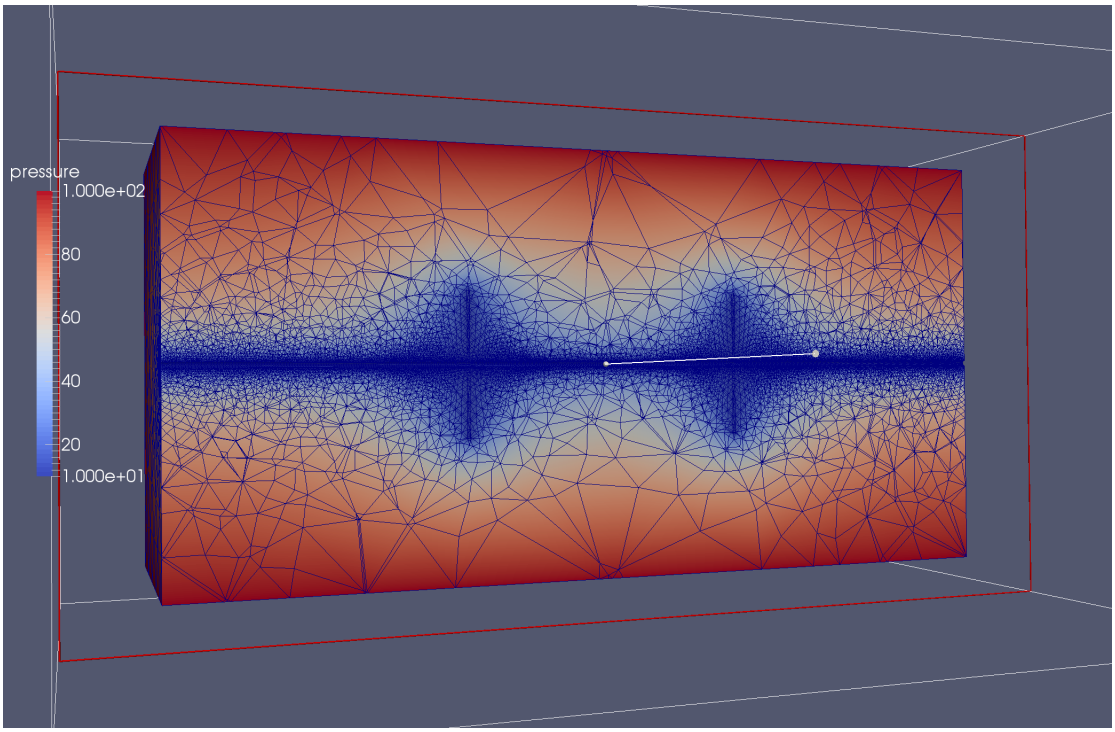

Figure 6.26: A slice view of the SRV. Note the gradual outward coarsening of the mesh.

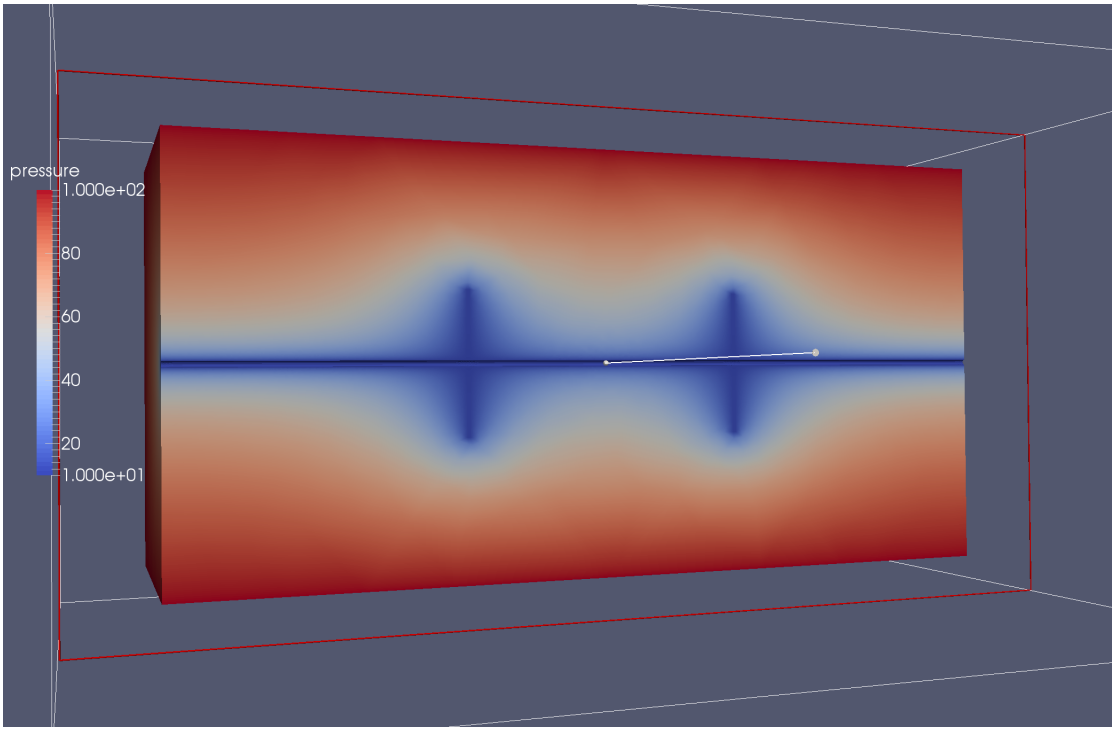

Figure 6.27: A slightly different view with the mesh edges removed.

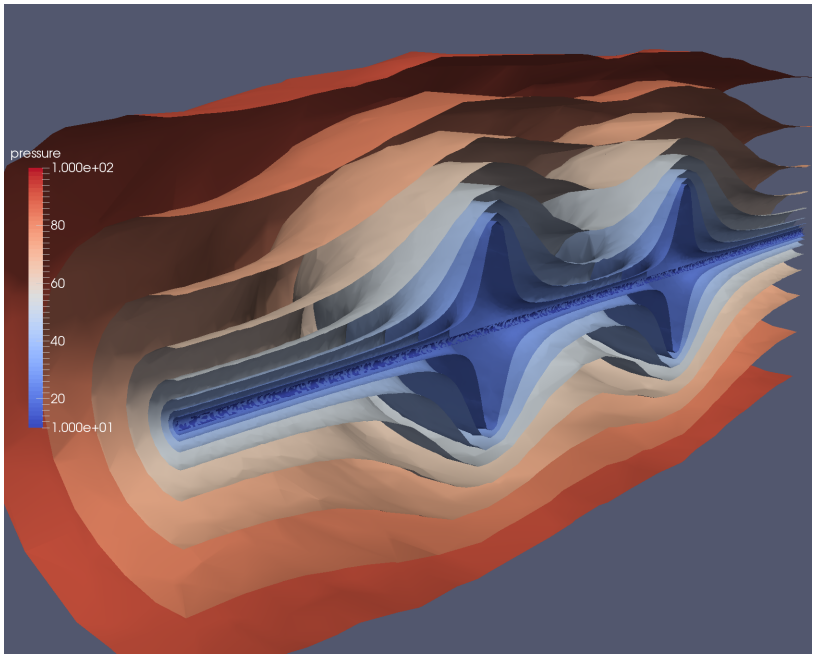

Figure 6.28: An iso-surface plot for various pressure values

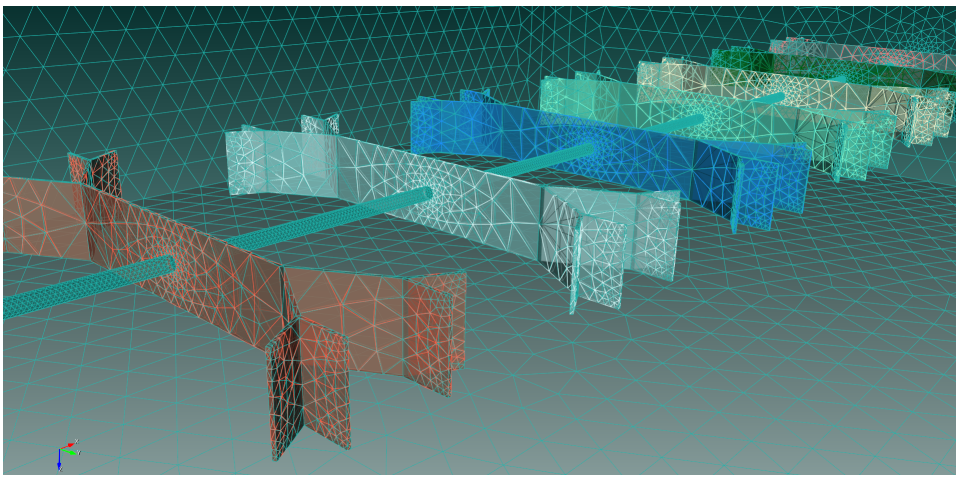

Figure 6.29: Python scripted fractally generated fracture mesh

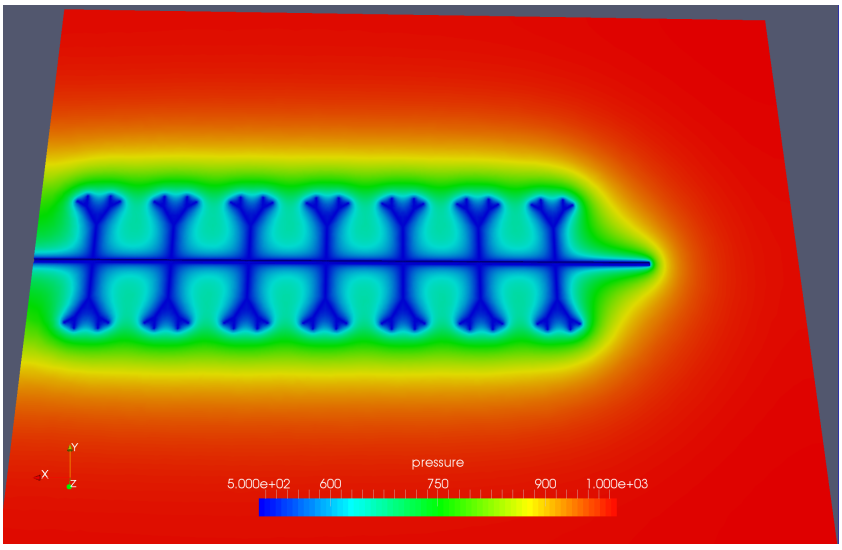

Figure 6.30: Pressure solution for a 10 Darcy fracture, 10 Nano Darcy matrix, 1000psi reservoir 500psi well flow problem

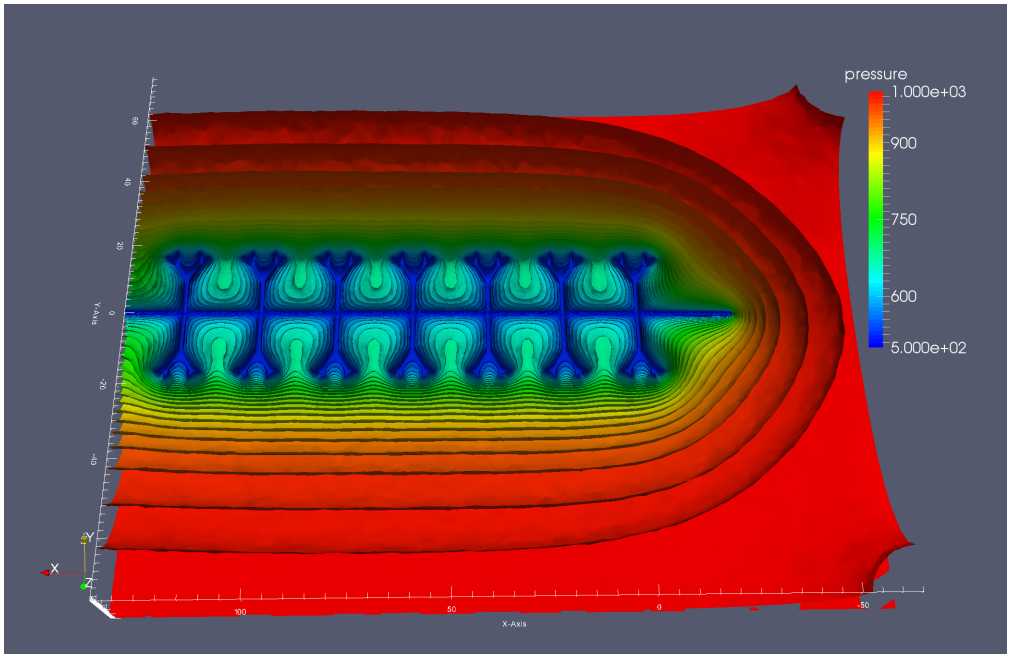

Figure 6.31: Isosurface plot of the same problem as figure 6.31. Note how near well flow is captured accurately especially at the well toe.

- Hybrid CPU parallelism with MPI and OpenMP that is ideally suited for large shared memory systems such as Intel Xeon Phi or Power9

For medium sized single core jobs the performance of the CUSP GPU based solver is 28% to 40% faster than algebraic multigrid preconditioned Jacobian-free Newton Kyrlov. However as the problem size increases array transfer costs erode the performance gains. The recommended solver settings would, therefore, be the algebraic multigrid preconditioned Jacobian-free Newton Krylov solver (JFNK). This solver/preconditioner combination outperforms JFNK preconditioned with split operator "physics based" by 30% and JFNK preconditioned with block diagonal preconditioner.

In terms of scalability, figure 6.32 depicts the results of a weak and strong scaling study. Note the log 10 scale on both axis. Since Moose is based on libmesh, which is in turn based on PETSc, scalability to tens of thousands of cores is not an issue. However, as is the case with most memory bound applications that are scaled too high, mpi communication costs increase and the application becomes network bound.

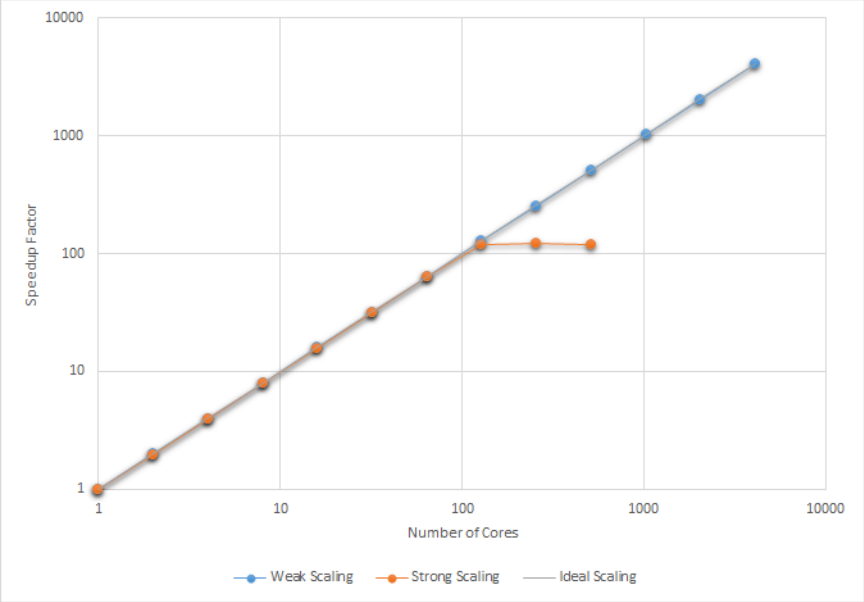

Figure 6.32: Strong and Weak scaling plots. Note that the strong scaling factor plateaus after 128 cores. The

Chapter 7
Effects of Various Physical Models

7.1 Analytical Discussion

As a precursor to the detailed numerical investigation, we will perform a dimensional analysis for the various models we have used thus far. The dimensionless variables are denoted with a hat, characteristic parameters are denoted with the c subscript, that is:

$$
\begin{aligned}
length\, \hat{l} &= \frac{l}{l_c} \\
time\, \hat{t} &= \frac{t}{t_c} \\
pressure\, \hat{p} &= \frac{p}{p_c} \\
velocity\, \hat{\mathbf{v}} &= \frac{\mathbf{v}}{\mathbf{v}_c} \\
density\, \hat{\rho} &= \frac{\rho}{\rho_c} \\
gradient, divergence operator\, \hat{\nabla} &= l_c \nabla
\end{aligned}
$$

It is not possible to fix all the characteristic quantities independently of each other, there are some characteristic quantities which are given as a function of others, density and pressure for example. The choice of the characteristic quantities introduced above can vary the output of the model significantly since they scale the dimensionless variables.

The dimensionless form of Darcy's law can be derived as follows:

$$\mathbf{v} = -\frac{K}{\mu}\left(\nabla P - \rho g\right) \tag{7.1}$$

$$\hat{\mathbf{v}}\mathbf{v_c} = -\frac{K}{\mu}\left(\frac{\hat{\nabla}}{l_c}\hat{P}P_c - \hat{\rho}\rho_c g\right) \tag{7.2}$$

Using the following definitions for capillary and gravity numbers:

$$C_a = \frac{KP_c}{l_c v_c \mu} = \frac{capillary\ force}{viscous\ force} \tag{7.3}$$

$$G_r = \frac{K\rho g}{v_c \mu} = \frac{gravity\ force}{viscous\ force} \tag{7.4}$$

and substituting back into 7.2 we obtain the following dimensionless form of Darcy's law:

$$\hat{\mathbf{v}} = -\left(C_a \hat{\nabla}\hat{P} - G_r\right) \tag{7.5}$$

Similarly, the dimensionless mass transport equation for component k in phase α with saturation S_α can be derived:

$$\sum_{\alpha \in o,g} \left(\frac{\partial\left(\phi \hat{\rho_\alpha} X_\alpha^k S_\alpha\right)}{\partial \hat{t}} + \hat{\nabla} \cdot \hat{\rho_\alpha} \left(\hat{\mathbf{v}_\alpha} X_\alpha^k - \frac{1}{Pe} \hat{\nabla} X_\alpha^k \right) \right) - \sum_{\alpha \in o,g} \frac{q_\alpha^k t_c}{\rho_{c\alpha}} = 0 \tag{7.6}$$

where P_e is the Pectlet number:

$$P_e = \frac{l_c v_c}{D_{\alpha,pm}^k} = \frac{advection}{diffusion} \tag{7.7}$$

The Peclet number determines the ratio of advection to diffusion. A low diffusion coefficient would give high Peclet numbers which makes the effect of the gradient of the mole fraction X_α^k insignificant compared to the advective transport of the mole fraction in the system. Larger diffusion would make the gradient of the mole fraction a significant term in the equation and it will have to be considered. For simplicity, in the following analysis we will assume:

- Gravity effects are not of interest
- Single component, single phase flow

Darcy's law is therefore reduced to the following dimensionless form:

$$\hat{\mathbf{v}} = -C_a \hat{\nabla} \hat{P} \tag{7.8}$$

The mass transport equation is then reduced to the mass balance equation:

$$\frac{\partial (\phi \hat{\rho})}{\partial \hat{t}} + \hat{\nabla} \cdot (\hat{\rho} \hat{\mathbf{v}}) - \frac{q t_c}{\rho_c} = 0 \tag{7.9}$$

7.1.1 Dimensionless Klinkenberg

Starting from the Klinkenberg permeability correction:

$$\mathbf{v} = -\frac{K}{\mu} \left(1 + \frac{b}{P}\right) \nabla P$$

We can derive the following dimensionless Klinkenberg equation:

$$\hat{\mathbf{v}} \mathbf{v}_c = -\frac{K P_c}{\mu l_c} \hat{\nabla} \hat{P} - \frac{K}{\mu} \frac{b}{\hat{P} P_c} \frac{\hat{\nabla}}{l_c} \hat{P} P_c \tag{7.10}$$

$$\hat{\mathbf{v}} = -\frac{K P_c}{\mu l_c v_c} \hat{\nabla} \hat{P} - \frac{K b}{\mu l_c v_c} \frac{1}{\hat{P}} \hat{\nabla} \hat{P} \tag{7.11}$$

$$\hat{\mathbf{v}} = -Ca \hat{\nabla} \hat{P} - \frac{Ka}{\hat{P}} \hat{\nabla} \hat{P} \tag{7.12}$$

Where Ca is the capillary number from 7.3 and Ka, the dimensionless Klinkenberg effect number we define as:

$$Ka = \frac{Kb}{\mu v_c l_c} = \frac{Klinkenberg\ force}{viscous\ force}$$

This is inline with our understanding of the capillary number since the Klinkenberg correction factor b has the same units as pressure.

The deviation from the dimensionless form of Darcy's law is the second term on the right hand side of equation 7.12, i.e. the term: $Ka/\hat{P}$. Note that this term will be important if:

- The Klinkenberg effect number is large
- The dimensionless pressure is low

We can therefore expect Klinkenberg permeability correction to be significant in:

- reservoirs with large Klinkenberg permeability correction factors (i.e. b) and therefore a significant Klinkenberg dimensionless number
- reservoirs (or parts thereof) where the pressure is low (which increases the contribution of Klinkenberg correction).

7.1.2 Dimensionless Forchheimer

Starting from Forchheimer's equation:

$$-\nabla P = \frac{\mu}{K}\mathbf{v} + \beta\rho\mathbf{v}\left|\mathbf{v}\right|$$

Assume one dimensional flow for simplicity:

$$-\nabla P = \frac{\mu}{K}\mathbf{v} + \beta\rho\mathbf{v}^2$$

We can derive the dimensionless form as follows:

$$-\nabla P = \frac{\mu}{K}\mathbf{v} + \beta\rho\mathbf{v}^2 \tag{7.13}$$

$$-\frac{\hat{\nabla}}{l_c}\hat{P}P_c = \frac{\mu}{K}\mathbf{v}_c\hat{\mathbf{v}} + \beta\rho\hat{\mathbf{v}^2}\mathbf{v}_c^2 \tag{7.14}$$

$$-\hat{\nabla}\hat{P} = \frac{\mu l_c\mathbf{v}_c}{KP_c}\hat{\mathbf{v}} + \beta\frac{\rho l_c\mathbf{v}_c^2}{P_c}\hat{\mathbf{v}^2} \tag{7.15}$$

Using the definition of Ca the capillary number and Euler's number:

$$Eu = \frac{P_c}{\rho\mathbf{v}_c^2} = \frac{pressure\,force}{inertia\,force}$$

and substituting in equation 7.15 we arrive at:

$$-\hat{\nabla}\hat{P} = \frac{1}{Ca}\hat{\mathbf{v}} + \frac{\beta l_c}{Eu}\hat{\mathbf{v}^2} \tag{7.16}$$

In this equation 7.16, the first term on the right hand side can be thought of as the pressure gradient required to overcome the viscous resistance. Similarly, the second term is the pressure gradient needed to overcome the inertial resistance. Rearranging:

$$\hat{\mathbf{v}} = -Ca\hat{\nabla}\hat{P} - \beta l_c \frac{Ca}{Eu}\hat{\mathbf{v}^2} \tag{7.17}$$

Note that we can use Reynolds number $Re = \rho \mathbf{v}_c l_c/\mu$ to obtain:

$$\hat{\mathbf{v}} = -Ca\hat{\nabla}\hat{P} - \frac{\beta K}{l_c} Re\hat{\mathbf{v}^2} \tag{7.18}$$

The dimensions are consistent since β is L^{-1} and K is L^2. Note that Zeng and Grigg (2006) cautioned that Reynolds number in this formulation 7.18 cannot be used as the only criteria to determining non- Darcy flow and proposed their Forchheimer number alternative, the ratio of non-Darcy to Darcy flow. For our purposes however, it is clear that the larger the Reynolds number, the larger the deviation from Darcy flow. Furthermore, the $\beta K/lc$ term, Forchheimer factor multiplied by permeability, plays an important role in determining how pronounced the deviation is.

7.2 Numerical Effects of Physical Models

7.2.1 Effect of Klinkenberg Diffusion

To numerically investigate the effect of Klinkenberg diffusion we run parameter sweep simulations over two cases: flow in a rectangular domain and flow in a radial domain. We impose a set of Dirichlet boundary conditions and a flow rate (Neumann) boundary condition. The parameters for the studies were:

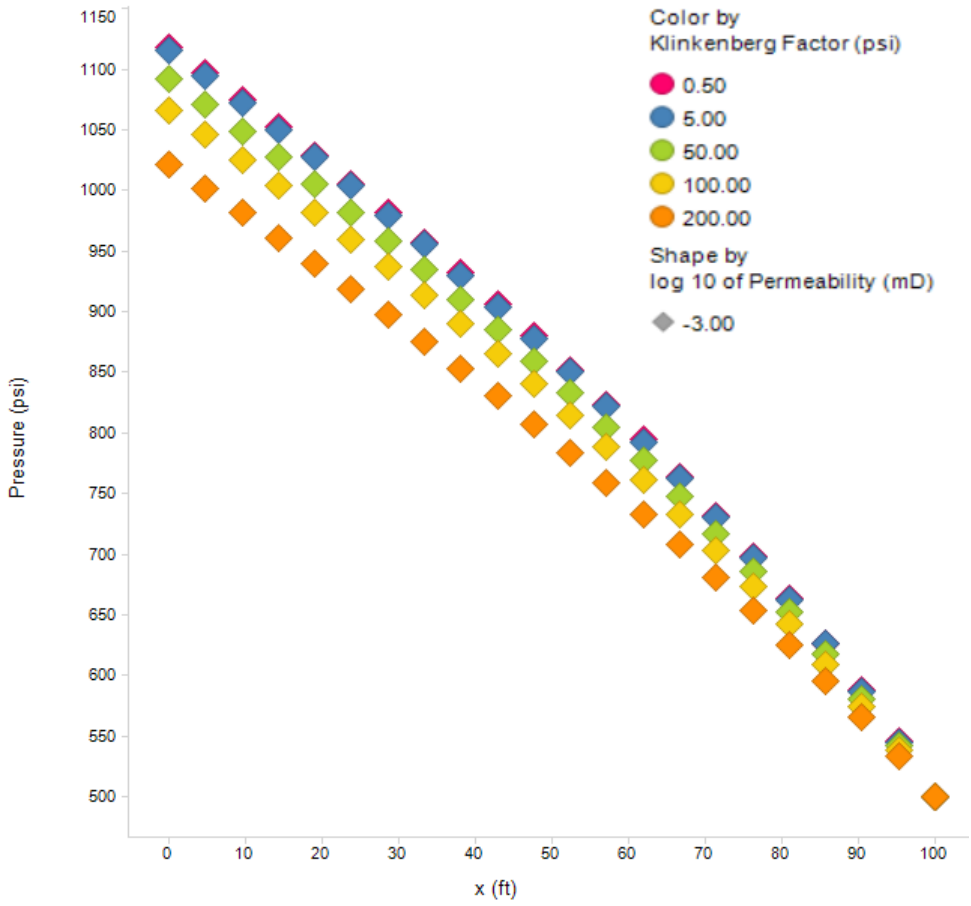

Figure 7.1: Pressure (psi) along the x-axis (ft) in with linear compressible flow

- Permeability (in milli Darcy): 1000, 1, 0.001, 0.000001
- Klinkenberg factor (in psi): 0.5, 5, 50, 100, 200
- Flow Rate (in MMscf/day): 1.0e-6, 1.0e-3, 1, 10
- Reservoir pressure (in psi): 500, 5000, 1000

For simplicity, the length (100 ft), area (10 squared ft), radius (100ft), well radius (0.1 ft), height (10 ft), compressibility and viscosity (0.0184 cp) were kept constant.

Figures 7.1 and 7.2 depict the pressure along the x-axis and radius of the linear and radial cases. Note the variation of the endpoint pressure based on the value of the Klinkenberg b-factor. We can therefore plot the relative change in pressure based on variations of

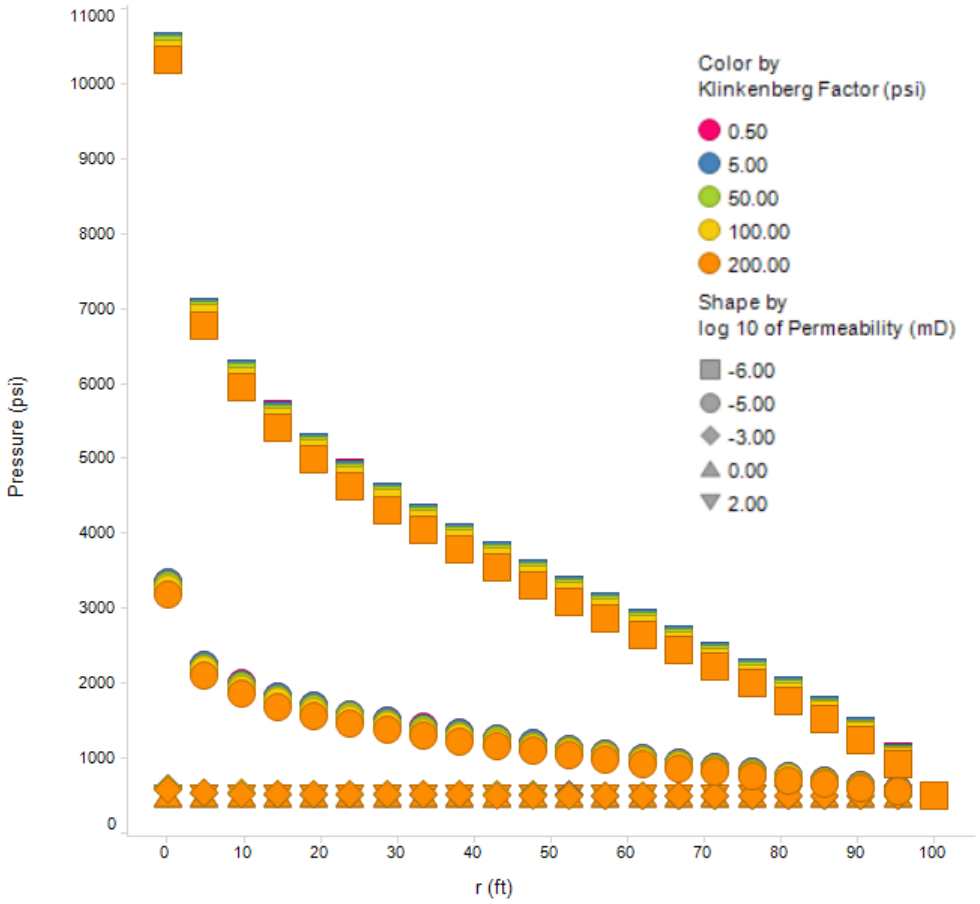

Figure 7.2: Pressure (psi) along the radius (ft) in the radial compressible flow

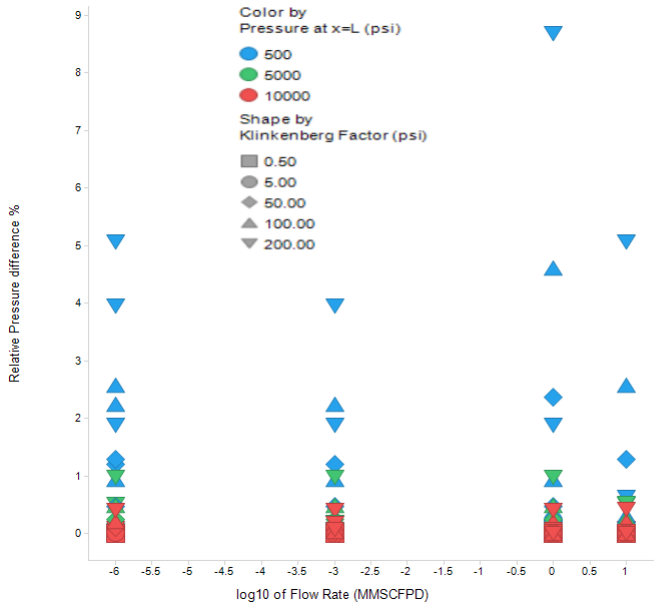

Figure 7.3: Relative pressure change % is independent of the flowrate in the linear case

the parameters in the studies. For example, the relative change in pressure is independent of the flow rate in both linear and radial cases as shown by Figures 7.3 and 7.4.

The relative change in pressure depends heavily on the Klinkenberg factor divided by pressure, after all this is the permeability correction factor. Case in point, Figures 7.5 and 7.6 show the relative change in pressure as it varies with the ratio of Klinkenberg factor to reservoir pressure. Note that as the pressure of the reservoir decreases this effect is more pronounced.

To be thorough we can also examine the effect of reservoir pressure. Figures 7.7 and 7.8 show these effects. Note that Klinkenberg slip effects are most pronounced at low pressure or extraordinarily high Klinkenberg correction factors.

Lastly we examine the effect of varying permeability and it should come as no surprise that permeability does not hold a strong influence on the relative pressure change. Figures 7.9 and 7.10 depict that fact. However, Klinkenberg slip phenomena exclusively apply in matrices where the mean free path of the gas molecules is comparable to the pore throat which is common in low permeability shales.

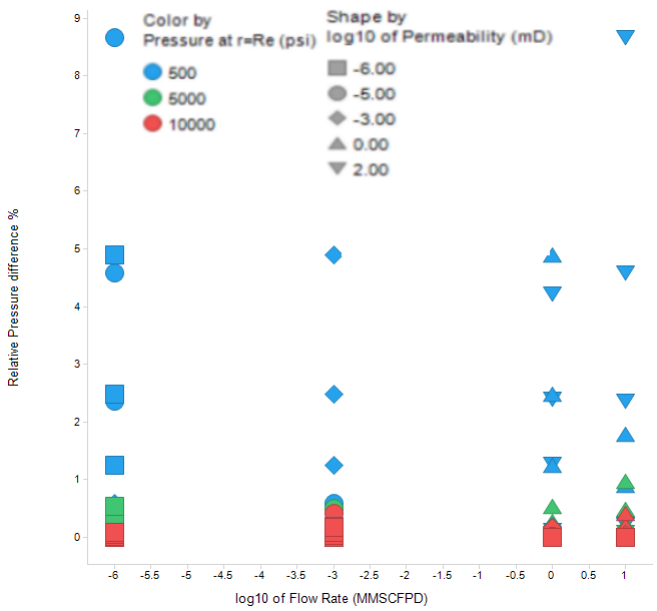

Figure 7.4: Relative pressure change % is independent of the flowrate in the radial case

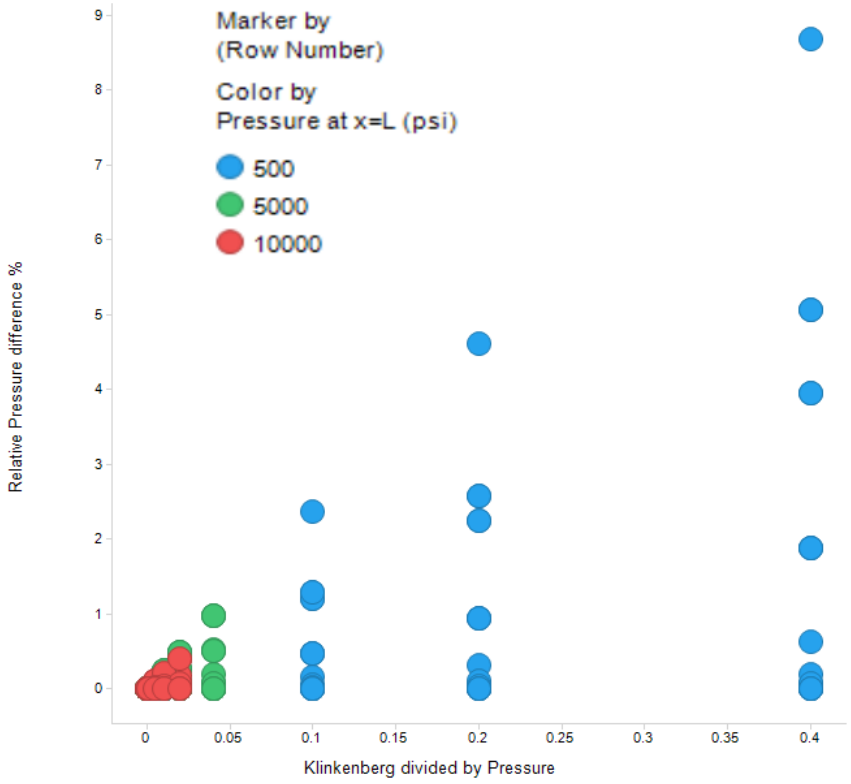

Figure 7.5: Relative pressure change % is a function of Klinkenberg factor divided by pressure in the linear case

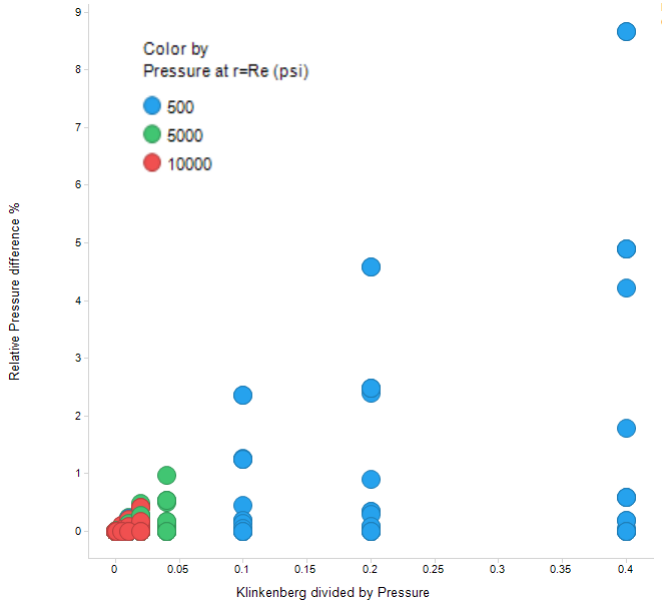

Figure 7.6: Relative pressure change % is a function of Klinkenberg factor divided by pressure in the radial case

Figure 7.7: Relative pressure change % depends heavily on pressure, the lower the pressure the more pronounced the effect, linear case

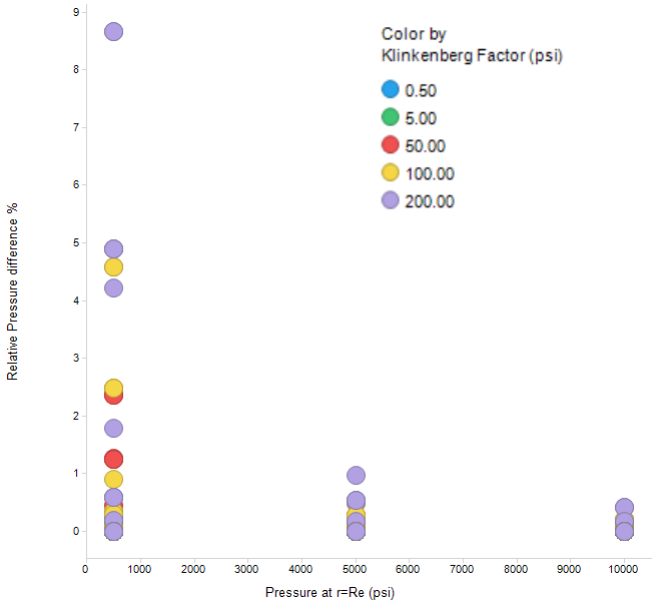

Figure 7.8: Relative pressure change % depends heavily on pressure, the lower the pressure the more pronounced the effect, radial case

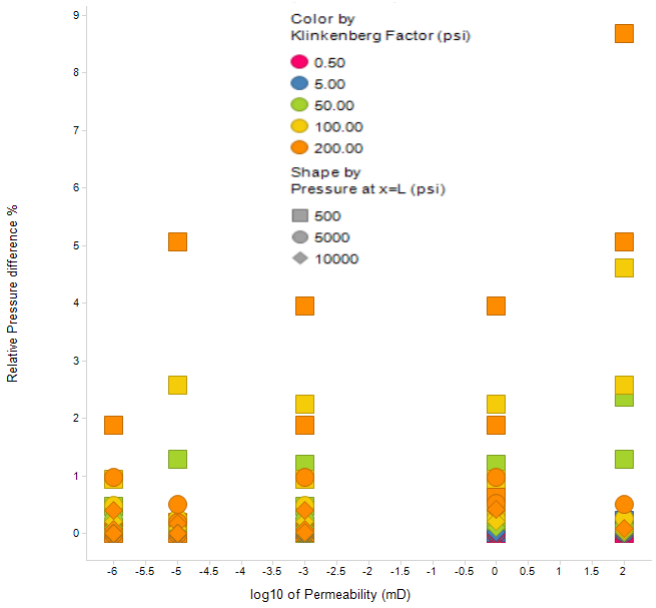

Figure 7.9: Relative pressure change % does not depend on permeability, linear

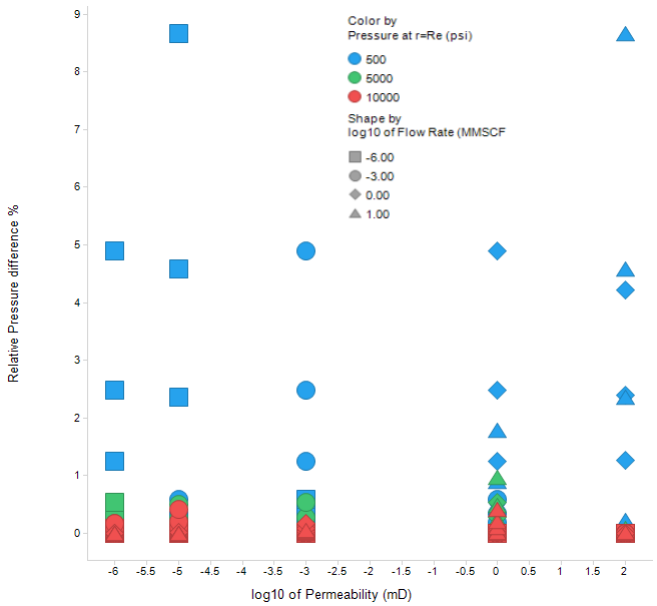

Figure 7.10: Relative pressure change % does not depend on permeability, radial case

The conclusions that can be drawn from these studies are as follows:

- Klinkenberg correction should be investigated (and appropriately applied) in shale matrices
- Klinkenberg correction depends heavily on pressure: the lower the pressure, the more pronounced the effect
- Klinkenberg correction depends heavily on the Klinkenberg factor: the higher the Klinkenberg factor the higher the effect
- A quick set of coarse simulations can be used to determine the need for including Klinkenberg effects, specifically outside the SRV where pressure is high
- Ignoring Klinkenberg correction when its effect is undetectable can moderately improve performance since the presence of pressure in the denominator leads to highly nonlinear terms in the Jacobian
- Klinkenberg correction should be thoroughly investigated in matrix flow near producing wells and connecting fractures (low pressure) and low pressure shale reservoirs

7.2.2 Effect of Forchheimer Flow

The Forchheimer factor β (non-Darcy Beta factor) used in the Forchheimer correction is determined using a correlation proposed by R.d and F. (1994) as given below:

$$\beta = 1.485e9/K^{1.021} \tag{7.19}$$

where the unit of K is milli Darcy (md) and unit of β is ft^{-1} . This β correlation was obtained using over 180 data points including those for propped fractures and was found to match the data very well with a correlation coefficient of 0.974 (Rubin et al. 2010). This equation is implemented in the reservoir simulator and used to evaluate the effect of Forchheimer flow with a parameter sweep study.

We use the same problem setup as before, flow in rectilinear and radial domains (i.e. away from well and near the well) and we vary the following parameters:

- Permeability (in md): 1.0e5 (i.e. 100 Darcy), 1.0e4, 1.0e3, 1.0e2, 1.0, 1.0e-2, 1.0e-5, 1.0e-6
- Beta correlates with permeability now so its values are (in ft^{-1}): 1.166e4, 1.223e5, 1.284e6, 1.348e7, 1.485e9, 1.635e11, 1.891e14, 1.98484434e+15
- Pressure varies (in psi) in the range: 500, 5000 to 10000 psi
- Flowrate varies (in MMscf per day) in the range: 1.0e-6, 1.0e-3, 1.0, 10.0

And again, for simplicity, the length (100 ft), area (10 squared ft), radius (100ft), well radius (0.1 ft), height (10 ft), compressibility and viscosity (0.0184 cp) were kept constant.

Figures 7.11 and 7.12 show the small effect Forchheimer flow has at a moderate flow rate in the linear case at both ends of the permeability scale, low and high. Figures 7.13 and 7.14 depict the similar small effect for the radial case.

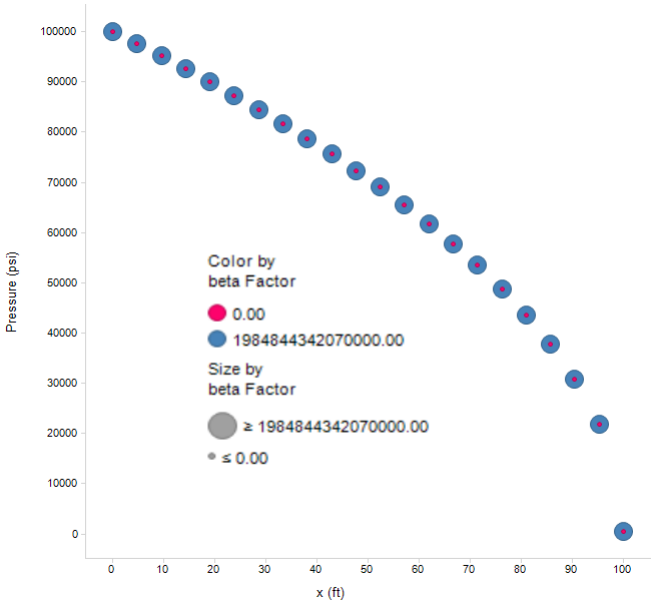

Figure 7.11: Forchheimer flow vs Darcy flow with medium flow rate, linear case and low permeability

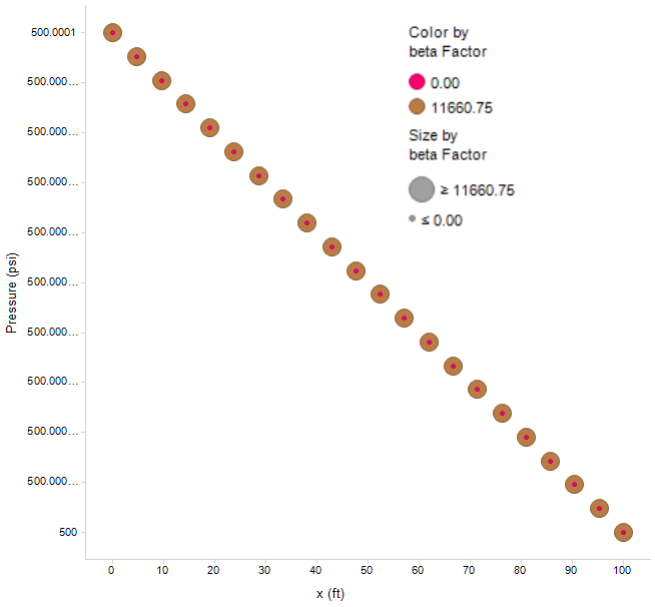

Figure 7.12: Forchheimer flow vs Darcy flow with medium flow rate, linear case and high permeability

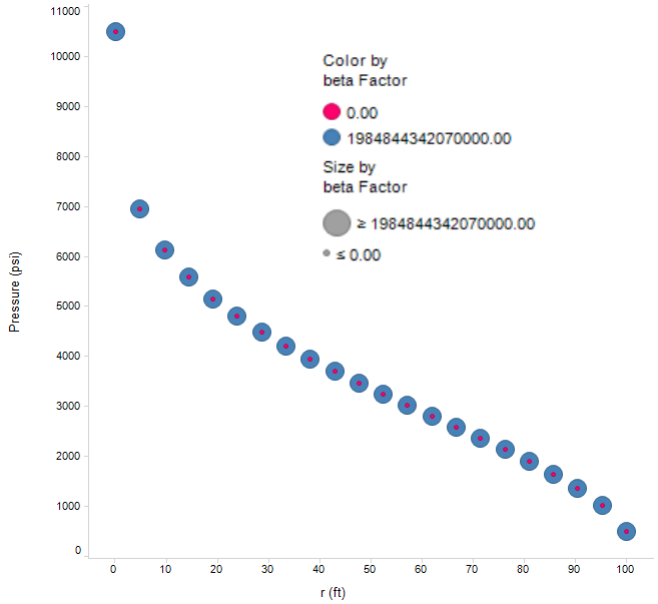

Figure 7.13: Forchheimer flow vs Darcy flow with medium flow rate, radial case and low permeability

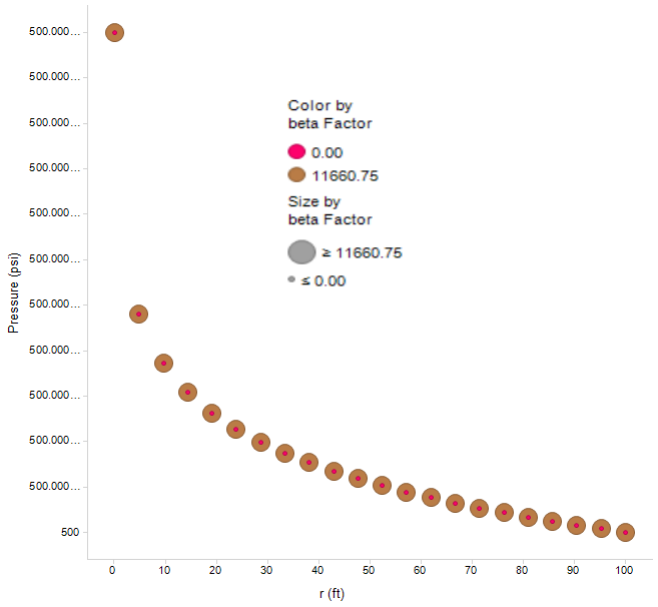

Figure 7.14: Forchheimer flow vs Darcy flow with medium flow rate, radial case and high permeability

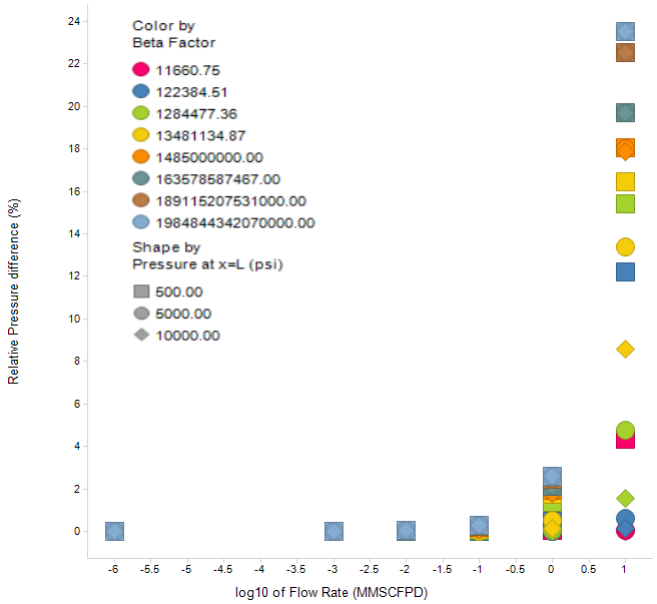

Figure 7.15: Relative pressure change versus log10 of MMscf/day in the linear case. Note the higher the β factor and the lower the pressure, the higher the effect

Since Forchheimer flow is inertial flow, flow velocity and subsequently the flow rate is a primary controlling factor. It is no surprise therefore that sufficiently high flow rates will cause greater deviation between Darcy and Forchheimer flows.

Figures 7.15 and 7.16 depict the effect of flow rate on the relative change in pressure for linear and radial cases. Note that the higher the flow rate, the more pronounced the deviation from Darcy flow.

Also note that since we are using the Evans and Civan β-permeability correlation, the higher the β factor the lower the permeability. This is inline with the Forchheimer flow equation: for a given pressure gradient, as the Darcy component decreases (low permeability) the non-Darcy component (β multiplied twice by velocity) increases. Also note that as pressure decreases, so does the effect of Forchheimer flow.

Therefore Forchheimer flow should be taken into account when the flow rate is high, specifically when the flow rate is in the order of 100 Mscf/day in a 100ft by 10 squared ft volume or a 100ft outer radius, 0.1 ft inner radius, 10ft height cylinder. For comparison, the production rate reported from Marcellus Shale wells averages about 950 Mscf per day,

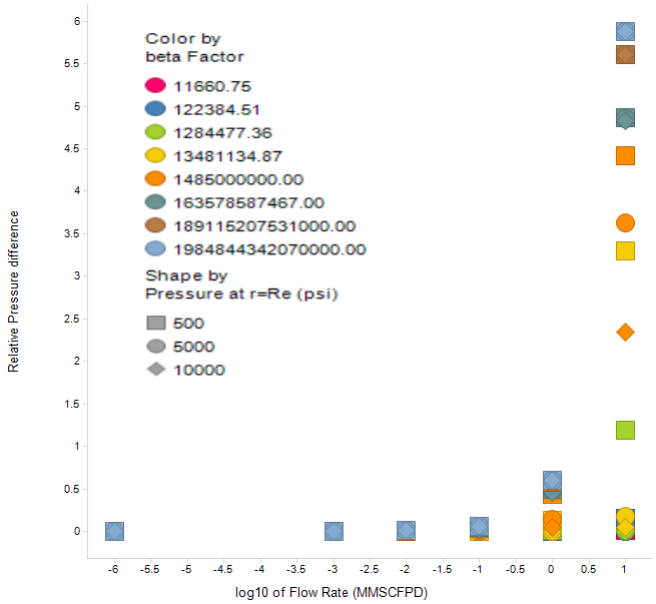

Figure 7.16: Relative pressure change versus log10 of MMscf/day in the radial case. Note the higher the β factor and the lower the pressure, the higher the effect

for Barnett shale 261 Mscf per day. Scaling flow rate by area, it is clear it is easy to arrive at conservative rule of thumb: if the production rate is lower than 10 Mscf/day taking stock of Forchheimer flow might be superfluous.

The following conclusions can be drawn:

- Forchheimer effects are most significant at very high flow rates
- Forchheimer effects are therefore most significant in the matrix (low permeability, high β factor) near the wells and fractures (low pressure), i.e. the SRV zone
- Forchheimer effects in fractures (high permeability, low β) can be ignored unless the pressure is low. High production pressures reduce the impact of Forchheimer effects in the fractures.
- Forchheimer flow outside the SRV zone in a reservoir with no natural fractures can be safely ignored if the flow rate is sufficiently low
- Forchheimer adds a highly non-linear term to the flow equation as well as another

higher order variable to the finite element formulation. It is very costly and should be avoided if at all possible.

7.2.3 Effect of Adsorption-Desorption

Gas in shale reservoirs can be present in some or all of the following forms:

- Free matrix pore structure gas
- Free gas in natural fractures
- Adsorbed gas on the surface of the shale matrix
- Adsorbed gas in the organic materials

The adsorption capacity of shales depends on several factors including the hydrocarbon composition, presence of CO2, specific surface area, pressure, temperature, pore size and adsorption affinity (Das et al. 2012; Leahy-Dios et al. 2011).

Unlike conventional gas reservoirs, shale gas reservoirs can potentially produce non-insignificant amounts of desorbed gas (Mengal et al. 2011). Gas desorption may be a major gas production mechanism and can be an important factor for ultimate gas recovery. Ignoring gas adsorption and desorption effects would therefore lead to underestimating gas potential. This is more pronounced in shale formations with higher total organic content. For example in the organic rich Woodford shale, the total organic carbon within the reservoir can occupy up to 40% of the reservoir rock by volume (Passey et al. 2010). Cipolla et al. (2010) reported that gas desorption may constitute 5-15% of the total gas production in 30-year period for both Barnett Shale and Marcellus Shale, but the impact of gas desorption is primarily observable during the later time of well production, depending on: initial reservoir pressure, reservoir permeability, flowing bottom hole pressure, hydraulic fracture geometry and the presence of natural fractures.

Therefore desorbed gas production needs to be taken into account in estimated ultimate recovery (EUR) studies. Thompson et al. (2011) states that gas desorption contributes to

Table 7.1: Langmuir adsorption data for different shale formations

Parameter	Barnett	Marcellus	EagleFord	Haynesville	New Albany	Unit
Langmuir Volume	96	200	175	60	104.2	scf/ton
Langmuir Pressure	650	500	1500	1500	412.5	psi
Bulk Density	2.58	2.46	2.6	2.6	2.4	g/cm3

17% increase in the EUR with respect to a 30-year forecasting result in a Marcellus shale well. Mengal et al. (2011) reported that gas desorption can result in approximately 30% increase in original gas in place estimates and 17% decrease in recovery factor estimates for Barnett Shale and concluded that it is impossible to obtain accurate estimations and forecasting if the gas desorption is ignored.

Despite several shortcomings, the most widely used adsorption/desorption model is the Langmuir isotherm model (Das et al. 2012; Yu and Sepehrnoori 2014). A quick survey of the available Langmuir model parameters for well known shale gas reservoirs are listed in Table 7.1

Using the information in Table 7.1 we can plot the volume of adsorbed gas versus pressure as shown in Figure 7.17. Assuming instantaneous equilibrium between adsorbed gas and free gas, i.e. $\tau = \tau_d = \tau_a$ we can compute the mass flow rate of desorbed gas versus pressure and add it as a pressure dependent source term to the flow equations.

A thorough analysis of the effects of desorption on gas production models was conducted byLewis et al. (2008). In their work with analytical and numerical models, gas desorption effects were documented on four common reservoir systems: single porosity, dual porosity, finite conductivity vertical fracture and dual porosity with a finite conductivity vertical pressure. From their analysis is it evident that the effects of desorption should be included in simulation for shale gas reservoirs, specifically reservoirs with high organic content and low pressure.

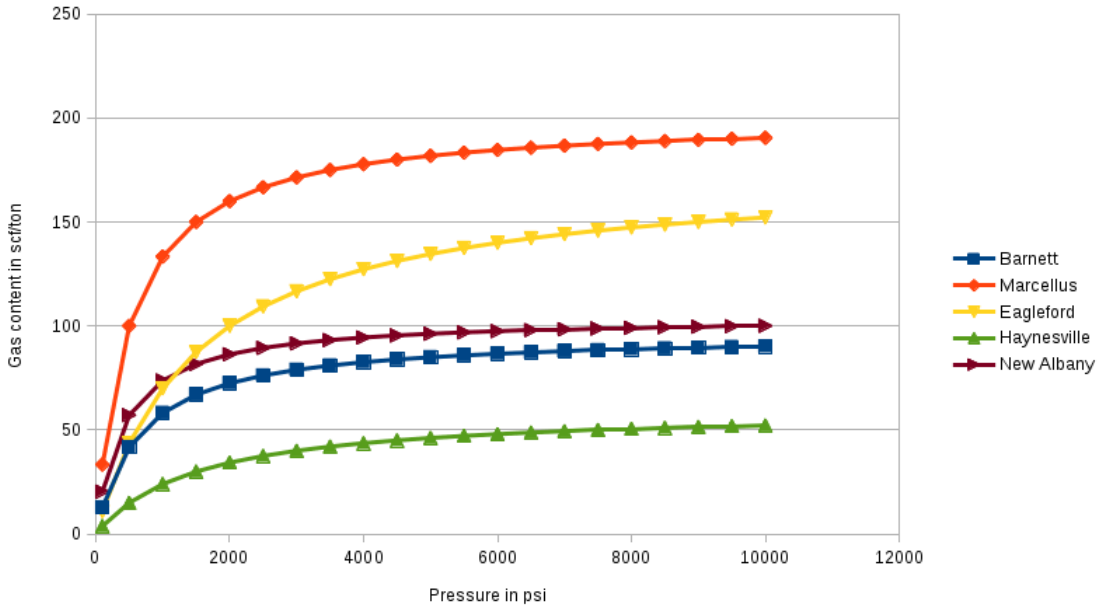

Figure 7.17: Langmuir Isotherm Curves for typical shale formations

Chapter 8
Conclusions and Future Work

8.1 Conclusions

Starting with the objective of accurately modeling fractured shale gas reservoirs, we survey available literature for the important physical phenomena that need to be taken into consideration and the various computational models associated with them. This includes Knudsen diffusion, natural and hydraulic fractures and adsorption/desorption.

We then develop and verify a parallel, scalable, finite element based reservoir simulator with advanced numerical, computational and physics capabilities. Some of these capabilities exist in commercial reservoir simulators to varying degrees however there is no single commercial reservoir simulator that combines support for AMR, AMG, scales to tens of thousands of cores and implements the various physical models we implemented.

After running sensitivity analysis studies with the reservoir simulator a few conclusions can be drawn, specifically regarding the relative importance of physical phenomena near hydraulic fractures and near wells.

Adsorption and desorption effects should always be taken into consideration in shale gas reservoirs since most are characterized by high organic content. Similarly since a good portion of shale gas reservoirs have low pressure (Antrim and New Albany are 2500 ft deep), Klinkenberg correction (or some form of Knudsen diffusion permeability correction) should be used in the whole reservoir. Quick, small scale simulations can be used to justify the use of Klinkenberg correction, especially with high pressure reservoirs since they incur additional computational complexity and cost to simulations.

Forchheimer flow effects are significant at high flow rates in the immediate vicinity of the wells and connecting fractures. Unless flow rates are extraordinarily high, the contribution of non-Darcy flow is otherwise minimal. Furthermore, if we are to use the widely accepted Evans and Civan β-permeability correlation, Forchheimer flow effects are most significant

in the matrix surrounding the well and hydraulic fractures where the flow rates are high. Inside the fracture, permeability is high which leads to a diminished β factor and a reduced Forchheimer effect.

A set of quick, low fidelity simulations with model parameters can and should be used to determine the need for Forchheimer flow simulation. The added cost of simulating Forchheimer versus Darcy flows is roughly 260% in terms of memory and roughly 210% in terms of CPU time. Judicial application of Forchheimer flow is therefore highly recommended.

It might be of some use, as a gedankenexperiment, to re-define the SRV as the region of the shale reservoir where Forchheimer flow effects are important. This would be the region surrounding the wells, hydraulic fractures and any natural fractures that network with the hydraulic fractures. Given this new definition, a multi-block capable reservoir simulator that can judiciously apply Forchheimer flow models, such as the reservoir simulator presented here, would be an economical alternative to whole grid Forchheimer simulations.

This proposed, redefined SRV would therefore be the region of the reservoir where non-Darcy flow, Knudsen diffusion and adsorption/desorption models apply. The outer zone of the reservoir would correspond to the region where only adsorption/desorption, possibly Knudsen diffusion (if supported by quick simulations) models apply.

8.2 Future Work

There are several pending features to this research reservoir simulator. They fall in three categories: new analysis, new physical models, improved features and improved usability.

8.2.1 New Analysis

One of the main advantages of using finite elements is the flexible geometry. The next step would be to study the effect of fidelity to fracture geometry. Fractures are rarely evenly spaced parallel rectangles, nor are they evenly spaced elliptical discs for that matter. Investigating the effect of fracture geometry be it generated or fitted to micro-seismic data might yield more insight into the necessary level of fidelity to the fracture geometry.

Another investigation that can be begin immediately would be analyzing combined effects of Forchheimer flow, slip flow and adsorption/desorption in the matrix surrounding the wells and hydraulic fractures. This analysis would not require new Jacobian terms to be generated, the complexity would be restricted to input file generation and post-processing.

8.2.2 New Physical Models

Per our conclusions, more care and effort should be placed, in general, in understanding the effects of Knudsen diffusion than Forchheimer flow since Forchheimer flow effects are arguably less prevalent. A large number of Knudsen diffusion models have been discussed in section 2.2 and some of them will be implemented for further study.

Currently support for multiphase flow is only reliably for two phases. This was mostly due to instability and front tracking issues. Investigations into the latest research in this area are underway along with a complete rewrite of the transport equations to move from a saturation to an accumulation formulation.

Finally a distinct advantage of having a finite element based reservoir simulator is the relative ease of coupling to a finite element based geomechanical model.

8.2.3 Improved Features

As the number of physical models increases, the need for automatic differentiation will only increase. This is not a difficult feature to implement, but it is difficult to implement in a performance friendly fashion. The added cost of computing derivatives can be detrimental to performance and by-hand derivative calculations will always be faster. A priori automatic differentiation using tools such as GiNAC and SymPy might be the answer.

One of the main concerns when using the Moose framework over libmesh directly is that it hides some of the low-level functionality that advanced users would need. Specifically support for Raviart Thomas finite elements. This would have reduced the cost of using higher order finite elements for Forchheimer flow problems. Another low level feature that would have been useful is better support for discontinuous Galerkin transfer terms.

8.2.4 Improved Usability

Currently all input has to be specified in the Moose input file language. A better solution would be to develop an input deck language in Python that generates the Moose input script for the most common scenarios: read geometry, specify well etc..

RESCUE file support is needed for integration with geologic modeling. Field history file (FHF) support should also be added to simplify comparison with existing reservoir simulators.

Well handling currently is rather basic: internal Dirichlet boundary condition, pressure on a node (or set of nodes identified by a node-set from Trelis) and of course Peaceman as uniform pressure over a block are supported. Flow rate constrained wells have been difficult to implement in a stable and usable fashion. Furthermore the focus of Moose and libmesh has been to simplify the process of assembling the matrix and right hand side rather than allow direct manipulation of the assembled, distributed matrix. There are some advanced features from the Moose framework, including multi-apps that can be used to this end.

Bibliography

Aguilera, R. et al. (2010). Flow units: from conventional to tight gas to shale gas reservoirs. In *Trinidad and Tobago Energy Resources Conference*. Society of Petroleum Engineers.

Aguilera, R. F. (2006). *Assessing the long run availability of global fossil energy resources*. Ph. D. thesis, Colorado School of Mines.

Ambrose, R. J., R. C. Hartman, M. Diaz Campos, I. Y. Akkutlu, C. Sondergeld, et al. (2010). New pore-scale considerations for shale gas in place calculations. In *SPE Unconventional Gas Conference*. Society of Petroleum Engineers.

Amiry, M. T., Z. E. Heinemann, and C. Brand (2014). The Heinemann-Mittermeir Generalized Shape Factor and Its Practical Relevance. *48*(1), 1–13.

Andrade Perdomo, J., F. Civan, D. Devegowda, and R. Sigal (2011). Design and examination of requirements for a rigorous shale-gas reservoir simulator compared to current shale-gas simulator. In *North American Unconventional Gas Conference and Exhibition*.

Andrade Perdomo, J. F., F. Civan, D. Devegowda, R. F. Sigal, et al. (2010). Accurate simulation of shale-gas reservoirs. In *SPE Annual Technical Conference and Exhibition*. Society of Petroleum Engineers.

AzomPN, J. (2012). Dual continuummodelingofshaleandtightgasreservoirs. In *SPE Annual Technical Conference and Exhibition. San Antonio, Texas, USA: Society of Petrole um Engineers*.

Balay, S., W. D. Gropp, L. C. McInnes, and B. F. Smith (1997). Efficient management of parallelism in object oriented numerical software libraries. In E. Arge, A. M. Bruaset, and H. P. Langtangen (Eds.), *Modern Software Tools in Scientific Computing*, pp. 163–202. Birkhäuser Press.

Beavers, G. and D. Joseph (1967). Boundary conditions at a naturally permeable wall. *Journal of fluid mechanics*.

Beskok, A. and G. E. Karniadakis (1999). Report: a model for flows in channels, pipes, and ducts at micro and nano scales. *Microscale Thermophysical Engineering 3*(1), 43–77.

Blasingame, T. A. et al. (2008). The characteristic flow behavior of low-permeability reservoir systems. In *SPE Unconventional Reservoirs Conference*. Society of Petroleum Engineers.

Brezzi, F. and M. Fortin (1991). Mixed and hybrid finite element methods, no. 15 in springer series in computational mathematics.

Chen, Z., G. Huan, and Y. Ma (2006). *Computational methods for multiphase flows in porous media*, Volume 2. Siam.

Cipolla, C., E. Lolon, J. Erdle, and B. Rubin (2010). Reservoir modeling in shale-gas reservoirs. *SPE Reservoir Evaluation & Engineering 13*(4), 638653.

Cipolla, C. L., E. P. Lolon, J. C. Erdle, B. Rubin, et al. (2010). Reservoir modeling in shale-gas reservoirs. *SPE reservoir evaluation & engineering 13*(04), 638–653.

Civan, F., D. Devegowda, R. F. Sigal, et al. (2013). Critical evaluation and improvement of methods for determination of matrix permeability of shale. In *SPE Annual Technical Conference and Exhibition*. Society of Petroleum Engineers.

Civan, F., C. S. Rai, and C. H. Sondergeld (2011). Shale-gas permeability and diffusivity inferred by improved formulation of relevant retention and transport mechanisms. *Transport in Porous Media 86*(3), 925–944.

Civan, F., C. S. Rai, C. H. Sondergeld, et al. (2012). Determining shale permeability to gas by simultaneous analysis of various pressure tests. *SPE Journal 17*(03), 717–726.

Coppens, M.-O. and A. J. Dammers (2006). Effects of heterogeneity on diffusion in nanoporesfrom inorganic materials to protein crystals and ion channels. *Fluid phase equilibria 241*(1), 308–316.

Cui, H. and M. Kelkar (2005, 3). Automatic history matching of naturally fractured reservoirs and a case study. *Proceedings of SPE Western Regional Meeting*.

Cui, X., A. Bustin, and R. M. Bustin (2009). Measurements of gas permeability and diffusivity of tight reservoir rocks: different approaches and their applications. *Geofluids 9*(3), 208–223.

Darabi, H., A. Ettehad, F. Javadpour, and K. Sepehrnoori (2012). Gas flow in ultra-tight shale strata. *Journal of Fluid Mechanics 710*, 641–658.

Darishchev, A., P. Rouvroy, P. Lemouzy, et al. (2013). On simulation of flow in tight and shale gas reservoirs. In *SPE Unconventional Gas Conference and Exhibition*. Society of Petroleum Engineers.

Das, M., R. Jonk, and R. Schelble (2012). Effect of multicomponent adsorption/desorption behavior on gas-in-place (gip) calculations and estimation of free and adsorbed ch4 and co2 in shale gas systems.

Ding, Y. D., Y.-s. Wu, N. Farah, C. Wang, and B. Bourbiaux (2014). Numerical Simulation of Low Permeability Unconventional Gas Reservoirs. *SPE/EAGE European Unconventional Resources Conference and Exhibition* (2008), 1–30.

Du, C., X. Zhang, B. Melton, D. Fullilove, E. Suliman, S. Gowelly, D. Grant, and J. Calvez (2009). A workflow for integrated barnett shale gas reservoir modeling and simulation. In *Latin American and Caribbean Petroleum Engineering Conference*, Number 2007, pp. 1–12.

Efendiev, Y. and T. Hou (2009). *Multiscale finite element methods: theory and applications*.

Ertekin, T., G. A. King, F. C. Schwerer, et al. (1986). Dynamic gas slippage: a unique dual-mechanism approach to the flow of gas in tight formations. *SPE formation evaluation 1*(01), 43–52.

Falgout, R. D. and U. M. Yang (2002). hypre: a library of high performance preconditioners. In *Preconditioners, Lecture Notes in Computer Science*, pp. 632–641.

Gad-el Hak, M. (1999). The fluid mechanics of microdevices-the freeman scholar lecture. *Transactions-American Society of Mechanical Engineers Journal of FLUIDS Engineering 121*, 5–33.

Geiger-Boschung, S., Q. Huangfu, F. Reid, S. Matthai, D. Coumou, M. Belayneh, C. Fricke, and K. Schmid (2009, February). Massively Parallel Sector Scale Discrete Fracture and Matrix Simulations. *Proceedings of SPE Reservoir Simulation Symposium*.

Guermond, J.-L. and R. Pasquetti (2008). Entropy-based nonlinear viscosity for fourier approximations of conservation laws. *Comptes Rendus Mathematique 346*(13), 801–806.

Gulbransen, A., V. Hauge, and K. Lie (2009). A multiscale mixed finite element method for vuggy and naturally fractured reservoirs. *SPE Reservoir Simulation ...* (November 2008), 2–4.

Gulbransen, A. F., V. L. Hauge, K.-a. Lie, and S. Ict (2010). A multiscale mixed finite-element method for vuggy and naturally fractured reservoirs. (November 2008), 2–4.

Holt, J. K., H. G. Park, Y. Wang, M. Stadermann, A. B. Artyukhin, C. P. Grigoropoulos, A. Noy, and O. Bakajin (2006). Fast mass transport through sub-2-nanometer carbon nanotubes. *Science 312*(5776), 1034–1037.

Hoteit, H. and A. Firoozabadi (2006, September). Compositional Modeling of Discrete-Fractured Media Without Transfer Functions by the Discontinuous Galerkin and Mixed Methods. *SPE Journal 11*(3), 26–29.

Jafarpour, B. and D. McLaughlin (2009, 3). Reservoir characterization with the discrete cosine transform. *SPE Journal 14*(1).

Jaffré, J., M. Mnejja, and J. Roberts (2011). A discrete fracture model for two-phase flow with matrix-fracture interaction. *Procedia Computer Science 4*, 967–973.

Java, F. and T. Univer (2012). Dual-Continuum Modeling of shale and tight gas reservoirs.

Javadpour, F. et al. (2009). Nanopores and apparent permeability of gas flow in mudrocks (shales and siltstone). *Journal of Canadian Petroleum Technology 48*(08), 16–21.

Javadpour, F., D. Fisher, M. Unsworth, et al. (2007). Nanoscale gas flow in shale gas sediments. *Journal of Canadian Petroleum Technology 46*(10).

Jones, S. et al. (1997). A technique for faster pulse-decay permeability measurements in tight rocks. *SPE Formation Evaluation 12*(01), 19–26.

Karimi-Fard, M., L. Durlofsky, and K. Aziz (2003, February). An Efficient Discrete Fracture Model Applicable for General Purpose Reservoir Simulators. *Proceedings of SPE Reservoir Simulation Symposium*, 1–11.

Kazemi, H., K. Porterfield, and P. Zeman (1976). Numerical simulation of water-oil flow in naturally fractured reservoirs. *Old SPE Journal 16*(6), 317326.

King, G. (2010). Thirty years of gas shale fracturing: What have we learned? In *SPE Annual Technical Conference and Exhibition*, Number September, pp. 19–22.

Klinkenberg, L. et al. (1941). The permeability of porous media to liquids and gases. In *Drilling and production practice*. American Petroleum Institute.

Koplik, J. and J. R. Banavar (1995). Continuum deductions from molecular hydrodynamics. *Annual Review of Fluid Mechanics 27*(1), 257–292.

Laptev, V. (2003). Numerical solution of coupled 2ow in plain and porous media. *2*.

Leahy-Dios, A., M. Das, A. Agarwal, R. D. Kaminsky, et al. (2011). Modeling of transport phenomena and multicomponent sorption for shale gas and coalbed methane in an unstructured grid simulator. In *SPE Annual Technical Conference and Exhibition*. Society of Petroleum Engineers.

Lewis, A. M., R. G. Hughes, et al. (2008). Production data analysis of shale gas reservoirs. In *SPE Annual Technical Conference and Exhibition*. Society of Petroleum Engineers.

Li, L. and S. Lee (2008, August). Efficient Field-Scale Simulation of Black Oil in a Naturally Fractured Reservoir Through Discrete Fracture Networks and Homogenized Media. *SPE Reservoir Evaluation & Engineering 11*(4), 5–7.

Lim, K. and K. Aziz (1995). Matrix-fracture transfer shape factors for dual-porosity simulators. *Journal of Petroleum Science and Engineering 13*(3), 169–178.

Liu, Q., P. Shen, and P. Yang (2002). Pore scale network modelling of gas slippage in tight porous media. *Contemporary Mathematics 295*, 367–376.

Lu, M. and L. D. Connell (2010, September). A Statistical Representation of the MatrixFracture Transfer Function for Porous Media. *Transport in Porous Media 86*(3), 777–803.

Lu, X.-C., F.-C. Li, and A. T. Watson (1995). Adsorption measurements in devonian shales. *Fuel 74*(4), 599–603.

Luffel, D., C. Hopkins, P. Schettler Jr, et al. (1993). Matrix permeability measurement of gas productive shales. In *SPE Annual Technical Conference and Exhibition*. Society of Petroleum Engineers.

Malek, K. and M.-O. Coppens (2002). Pore roughness effects on self-and transport diffusion in nanoporous materials. *Colloids and Surfaces A: Physicochemical and Engineering Aspects 206*(1), 335–348.

Mao, Z. and S. B. Sinnott (2001). Separation of organic molecular mixtures in carbon nanotubes and bundles: molecular dynamics simulations. *The Journal of Physical Chemistry B 105*(29), 6916–6924.

Martin, V., J. Jaffré, and J. Roberts (2005). Modeling fractures and barriers as interfaces for flow in porous media. *SIAM Journal on Scientific Computing 26*(5), 1667–1691.

Mengal, S. A., R. A. Wattenbarger, et al. (2011). Accounting for adsorbed gas in shale gas reservoirs. In *SPE Middle East Oil and Gas Show and Conference*. Society of Petroleum Engineers.

Minden, V., B. Smith, and M. Knepley (2010). Preliminary implementation of petsc using gpus. *Proceedings of the 2010 International Workshop of GPU Solutions to Multiscale Problems in Science and Engineering*.

Mirzaei, M., C. L. Cipolla, et al. (2012). A workflow for modeling and simulation of hydraulic fractures in unconventional gas reservoirs. In *SPE Middle East Unconventional Gas Conference and Exhibition*. Society of Petroleum Engineers.

Moghanloo, R. G. and S. Hosseinipoor (2014). The Mechanistic Modeling of Fluid Flow in Shale. *Proceedings of the 2nd Unconventional Resources Technology Conference* (2005).

Moinfar, A., W. Narr, M. Hui, B. Mallison, and S. Lee (2011). Comparison of discrete-fracture and dual-permeability models for multiphase flow in naturally fractured reservoirs. In *SPE Reservoir Simulation Symposium*, pp. 1–17.

Moridis, G. J., T. A. Blasingame, C. M. Freeman, et al. (2010). Analysis of mechanisms of flow in fractured tight-gas and shale-gas reservoirs. In *SPE Latin American and Caribbean Petroleum Engineering Conference*. Society of Petroleum Engineers.

Nie, X., S. Chen, M. Robbins, et al. (2004). A continuum and molecular dynamics hybrid method for micro-and nano-fluid flow. *Journal of Fluid Mechanics 500*, 55–64.

Ozkan, E., R. Raghavan, and O. Apaydin (2010). Modeling of fluid transfer from shale matrix to fracture network. In *SPE Annual Technical Conference and Exhibition*.

Passey, Q. R., K. Bohacs, W. L. Esch, R. Klimentidis, S. Sinha, et al. (2010). From oil-prone source rock to gas-producing shale reservoir-geologic and petrophysical characterization of unconventional shale gas reservoirs. In *International oil and gas conference and exhibition in China*. Society of Petroleum Engineers.

Popov, P., Y. Efendiev, and G. Qin (2009). Multiscale modeling and simulations of flows in naturally fractured karst reservoirs. *Communications in computational ... 6*(1), 162–184.

Popov, P., G. Qin, L. Bi, and Y. Efendiev (2009). Multiphysics and multiscale methods for modeling fluid flow through naturally fractured carbonate karst reservoirs. *SPE Reservoir ....*

Pruess, K. and T. N. Narasimhan (1985). A Practical Method for Modeling Fluid and Heat Flow in Fractured Porous Media. *Society of Petroleum Engineers Journal 25*(1), 14 – 26.

Rahmanian, M., R. Aguilera, A. Kantzas, et al. (2012). A new unified diffusion–viscous-flow model based on pore-level studies of tight gas formations. *SPE Journal 18*(01), 38–49.

R.d, E. and C. F. (1994). Characterization of non-darcy multiphase flow in petroleum bearing formation. In *Final Report For US Department Of Energy*. United States Department of Energy.

Roy, S., R. Raju, H. F. Chuang, B. A. Cruden, and M. Meyyappan (2003). Modeling gas flow through microchannels and nanopores. *Journal of applied physics 93*(8), 4870–4879.

Rubin, B. (2010). Accurate simulation of non darcy flow in stimulated fractured shale reservoirs. In *SPE Western Regional Meeting*.

Rubin, B. et al. (2010). Accurate simulation of non darcy flow in stimulated fractured shale reservoirs. In *SPE Western Regional Meeting*. Society of Petroleum Engineers.

Shabro, V., C. Torres-Verdin, and K. Sepehrnoori (2012). Forecasting Gas Production in Organic Shale with the Combined Numerical Simulation of Gas Diffusion in Kerogen, Langmuir Desorption from Kerogen Surfaces, and Advection in Nanopores. *Proceedings of SPE Annual Technical Conference and Exhibition*, SPE 159250.

Shahvali, M. (2014). Discrete Fracture Modeling of Shale Plays with Multi-stage Hydraulic Fracturing Using Centroidal Voronoi Mesh. *Ecmor Xiv* (September 2014), 8–11.

Singh, H., P. N. Azom, et al. (2013). Integration of nonempirical shale permeability model in a dual-continuum reservoir simulator. In *SPE Unconventional Resources Conference Canada*. Society of Petroleum Engineers.

Swami, V., A. T. Settari, F. Javadpour, et al. (2013). A numerical model for multi-mechanism flow in shale gas reservoirs with application to laboratory scale testing. In *EAGE Annual Conference & Exhibition incorporating SPE Europec*. Society of Petroleum Engineers.

Thompson, J., D. A. Fekete, and V. O. M'Angha (2011). Advancements in shale gas production forecasting - a marcellus case study. In *SPE North American Unconventional Gas Conference and Exhibition*. Society of Petroleum Engineers.

Tillet, P., K. Rupp, S. Selberherr, and C.-T. Lin (2013). Towards performance-portable, scalable, and convenient linear algebra. In *Presented as part of the 5th USENIX Workshop on Hot Topics in Parallelism*, Berkeley, CA. USENIX.

Tinni, A., E. Fathi, R. Agarwal, C. H. Sondergeld, I. Y. Akkutlu, C. S. Rai, et al. (2012). Shale permeability measurements on plugs and crushed samples. In *SPE Canadian Unconventional Resources Conference*. Society of Petroleum Engineers.

Tonks, M. R., D. Gaston, P. C. Millett, D. Andrs, and P. Talbot (2012). An object-oriented finite element framework for multiphysics phase field simulations. *Computational Materials Science 51*(1), 20 – 29.

Veltzke, T. and J. Thöming (2012). An analytically predictive model for moderately rarefied gas flow. *Journal of Fluid Mechanics 698*, 406–422.

Wang, C., G. Li, and A. Reynolds (2009a, 9). Production optimization in closed-loop reservoir management. *SPE Journal 14*(3).

Wang, M. and Z. Li (2003). Nonideal gas flow and heat transfer in micro-and nanochannels using the direct simulation monte carlo method. *Physical Review E 68*(4), 046704.

Wang, Y. (2015). A Hybrid Dual-Continuum Discrete Fracture Modeling Approach for Numerical Simulation of production from unconventional plays.

Wang, Y., G. Li, and A. Reynolds (2009b, 2). Estimation of depths of fluid contacts by history matching using iterative ensemble kalman smoothers. *Proceedings of SPE Reservoir Simulation Symposium* (2007).

Warren, J. and P. Root (1963). The behavior of naturally fractured reservoirs. *Old SPE Journal 3*(3), 245255.

Wu, Y.-S., K. Pruess, et al. (1998). Gas flow in porous media with klinkenberg effects. *Transport in Porous Media 32*(1), 117–137.

Wuthicharn, K. and R. W. Zimmerman (2011). SPE 148060 Shape Factors for Irregularly Shaped Matrix Blocks. (October), 9–11.

Xiong, X., D. Devegowda, M. Villazon, G. German, R. F. Sigal, F. Civan, et al. (2012). A fully-coupled free and adsorptive phase transport model for shale gas reservoirs including non-darcy flow effects. In *SPE Annual Technical Conference and Exhibition*. Society of Petroleum Engineers.

Yu, H. (2002). Scalar mixing and chemical reaction simulations using lattice boltzmann method 2 . lattice boltzmann equations. *3*(1).

Yu, W. and K. Sepehrnoori (2014). Simulation of gas desorption and geomechanics effects for unconventional gas reservoirs. *Fuel 116*, 455–464.

Yuan, W., Z. Pan, X. Li, Y. Yang, C. Zhao, L. D. Connell, S. Li, and J. He (2014). Experimental study and modelling of methane adsorption and diffusion in shale. *Fuel 117*, 509–519.

Zeng, Z. and R. Grigg (2006). A criterion for non-darcy flow in porous media. *Transport in Porous Media 63*(1), 57–69.

Zimmerman, R. W., G. Chen, T. Hadgu, and G. S. Bodvarsson (1993). A numerical dual-porosity model with semianalytical treatment of fracture/matrix flow. *Water resources research 29*(7), 2127–2137.

Appendix
Quarter Five Spot comparison with CMG

Adding more verification and validation cases is now easier with an automated well specification tool for mesh generation. On CMG's side we use local grid refinement to model fractures and explicit fractures in MOOSE. Initial pressure is 100 kPa, producer and injector pressures were 50 and 150 kPa respectively.

Figure A.1 shows the configuration and location of the fractures. Figures A.2 and A.3 show the pressure solution. Results are consistent with CMG, especially near the wells and throughout the simple fracture networks.

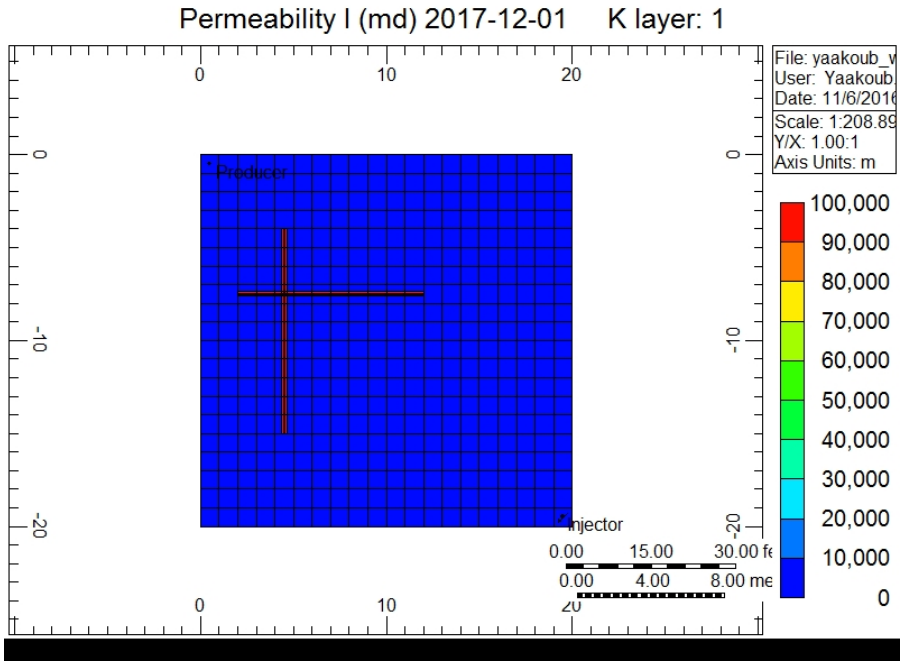

Figure A.1: Permeability of a simple quarter five spot problem with local grid refinement for fractures.

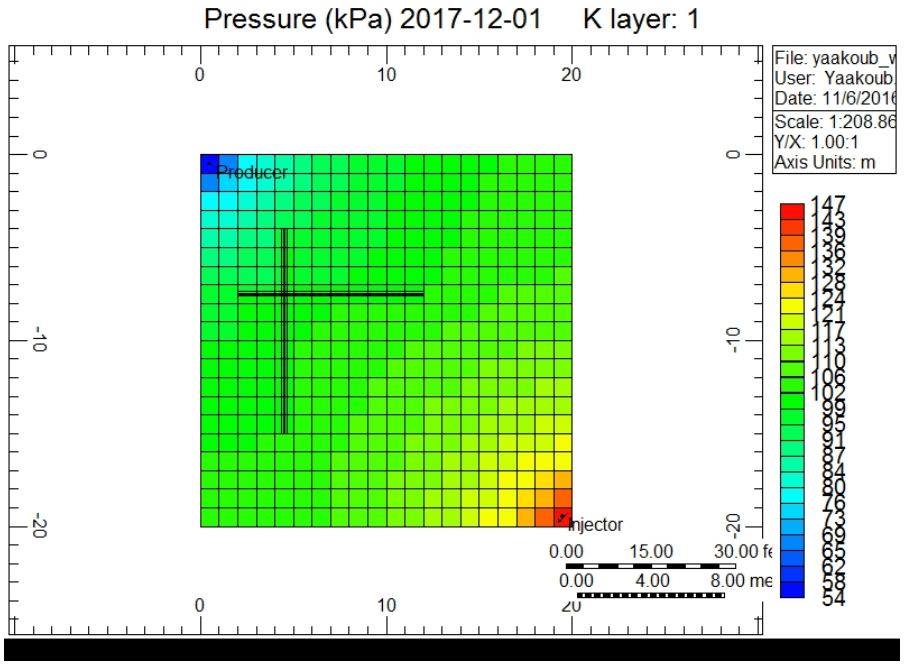

Figure A.2: CMG IMEX Pressure solution after one year of simulation

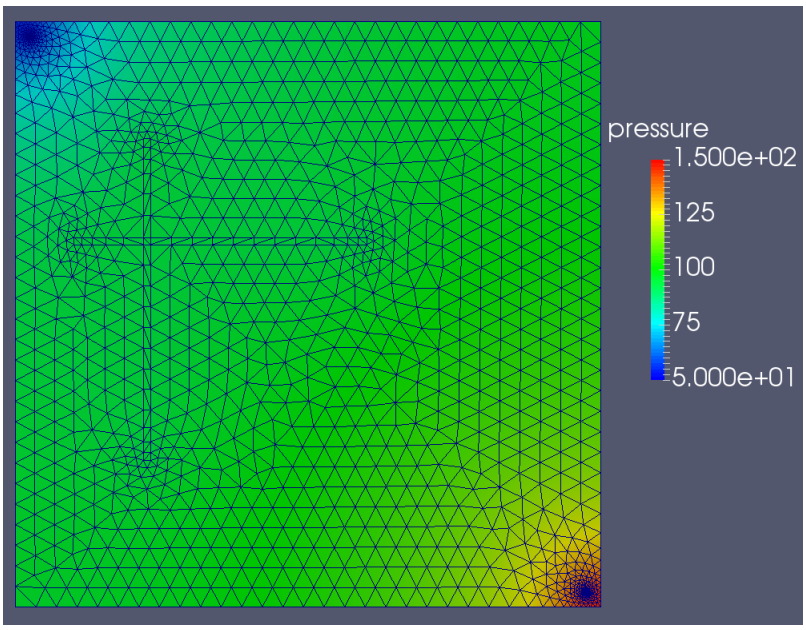

Figure A.3: Solution using MOOSE. Note the close agreement of the results with CMG

Vita

Yaakoub El Khamra received his Bachelor's degree in mechanical engineering from the American University of Beirut in 2002 and his Petroleum Engineering Masters degree from Louisiana State University in 2009.